Dissertation

submitted to the

Combined Faculties of the Natural Sciences and Mathematics

of the Ruperto-Carola-University of Heidelberg, Germany

for the degree of

Doctor of Natural Sciences

Put forward by

Julia Isabell Djuvsland

born in Heidelberg

Oral examination on July 28th, 2016

Analysis of $WW\gamma$ production with the ATLAS experiment

Referees: Prof. Dr. Hans-Christian Schultz-Coulon
Prof. Dr. Stephanie Hansmann-Menzemer

Abstract

In this thesis, triboson final states containing two W bosons and a photon are studied using proton-proton collisions. The data set was recorded with the ATLAS detector at a centre-of-mass energy of $\sqrt{s} = 8\,\text{TeV}$ and corresponds to an integrated luminosity of $20.3\,\text{fb}^{-1}$. The fiducial cross-section of the process $WW\gamma \to e\nu\mu\nu\gamma$ is measured for the first time in hadron collisions and corresponds to $\sigma_{\text{fid.}}^{e\mu\gamma} = (1.89 \pm 0.93(\text{stat.}) \pm 0.41(\text{syst.}) \pm 0.05(\text{lumi.}))\,\text{fb}$. It is in good agreement with the Standard Model prediction at next-to-leading order in the strong coupling constant. As no deviation from the Standard Model expectation is observed, frequentist limits at 95 % confidence level are computed to exclude contributions from anomalous quartic gauge couplings. This analysis is sensitive to fourteen coupling parameters of mass dimension eight and the limits are derived for all parameters with and without unitarisation.

Zusammenfassung

In der vorliegenden Arbeit wird die simultane Produktion eines Photons und zweier W-Bosonen analysiert. Die studierten Protonkollisionen wurden mit dem ATLAS-Detektor bei einer Schwerpunktsenergie von $\sqrt{s} = 8\,\text{TeV}$ aufgezeichnet und entsprechen einer integrierten Luminosität von $20.3\,\text{fb}^{-1}$. Dieser Datensatz ermöglicht es erstmalig, den Prozess $WW\gamma \to e\nu\mu\nu\gamma$ in Hadronkollisionen zu untersuchen. Der ermittelte Wirkungsquerschnitt beträgt $\sigma_{\text{fid.}}^{e\mu\gamma} = (1.89 \pm 0.93(\text{stat.}) \pm 0.41(\text{syst.}) \pm 0.05(\text{lumi.}))\,\text{fb}$ und ist mit den Erwartungen des Standardmodells in nächstführender Ordnung der starken Wechselwirkung gut vereinbar. Da keine Abweichung von der Standardmodell-Erwartung beobachtet wird, werden frequentistische Ausschlussgrenzen auf anomale quartischen Eichkopplungen mit einem Konfidenzintervall von 95 % gesetzt. Dieser Endzustand ist auf vierzehn Kopplungsparameter der Massendimension acht sensitiv und die Ausschlussgrenzen werden für alle Parameter mit und ohne Unitarisierung berechnet.

Contents

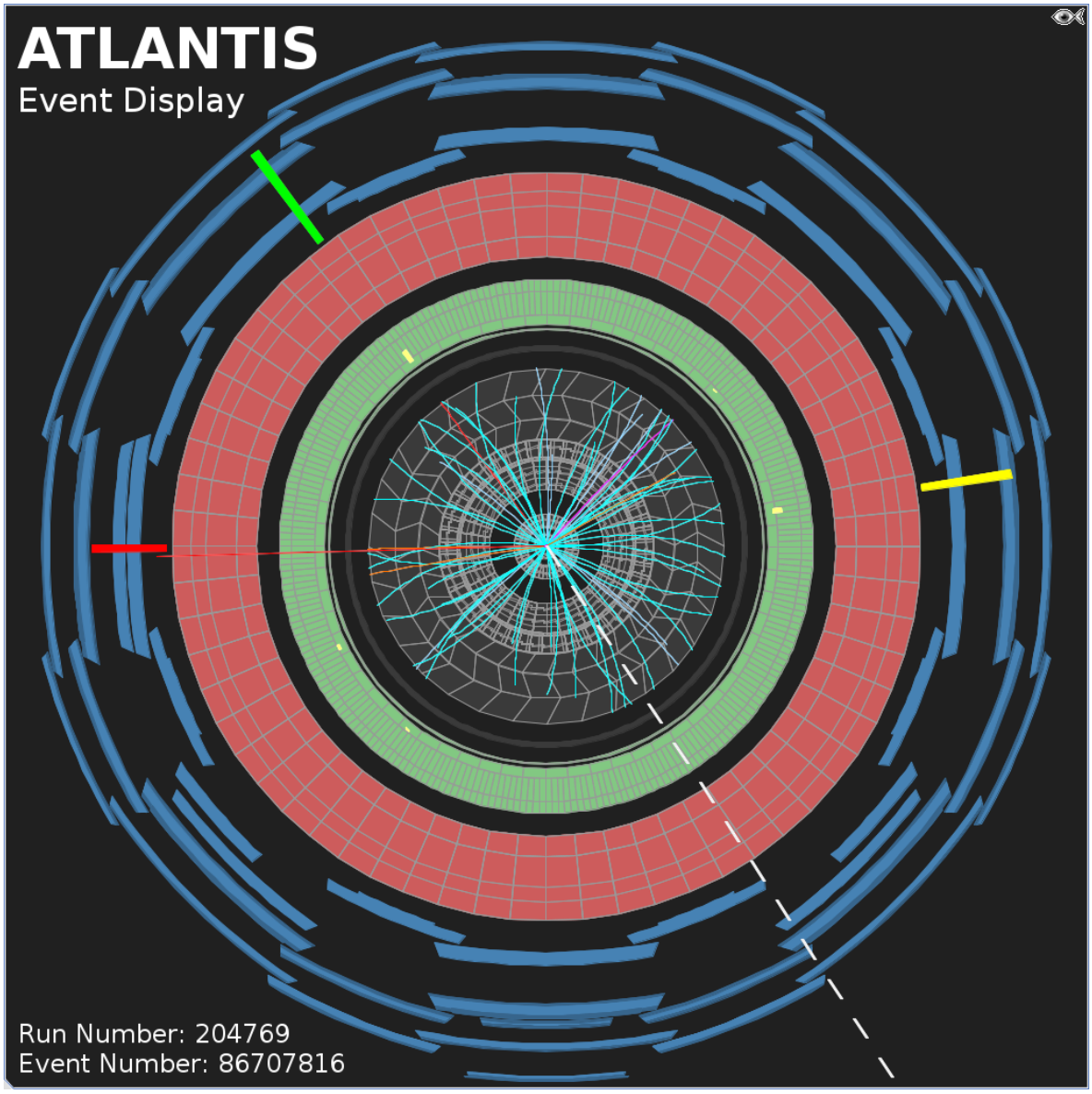

Figure 1: Visualisation of the outcome of a proton-proton collision recorded with the ATLAS detector using the Atlantis event display [1]. For better visibility, the proportions are distorted using the fish-eye effect. The event shown is a candidate signal event for the analysis presented here and was recorded on June 10^{th}, 2012 at 14:32:08 CEST.

Introduction

Understanding the basic principles of nature is at the heart of the research performed at the European Organization for Nuclear Research, CERN. Since its foundation in 1954, the laboratory has been studying the structure of the universe by examining particles, the building blocks of all matter. They are studied by analysing the outcome of particle collisions, which are induced in large accelerator complexes. The collision products are the fundamental particles that do not have any substructure according to the most widely accepted theory, the Standard Model of particle physics. These particles are assumed to be pointlike and their dimensions are so small that large machines are built in order to measure them.

One such machine is the ATLAS detector, which is located at the largest particle accelerator of CERN, the Large Hadron Collider, LHC. A sketch of a lateral cut of the ATLAS detector can be seen in Figure 1 along with the visualisation of the products of a proton-proton collision. The collision point is in the centre of the image and the different subcomponents of the detector are shown, as each employs a different technology for the measurement. The energetic particles that leave the collision are indicated by the three large coloured bars in the figure. These particles are of different nature and correspond to three types of fundamental particles that are indicated by their colour in the image: an electron in green, a photon in yellow and a muon in red.

The collisions are described by the Standard Model which is an established theory but still has some shortcomings that hint to the fact that it might need further expansion to describe the interactions at very high energies. Therefore, it is tested with scrutiny by the experiments located at the LHC. The electroweak sector of the model can be tested by the analysis of final states containing gauge bosons, as for example the production of a photon in association with two W bosons, $WW\gamma$. The fully-leptonic decay mode of this process has not been studied in hadron collisions before and is presented in this thesis. The challenge of this analysis is the low production probability of the process, which is why a data set with high statistics is needed. Thus, the proton-proton collisions recorded with the ATLAS detector at a centre-of-mass energy of $\sqrt{s} = 8\,\text{TeV}$ corresponding to an integrated luminosity of $20.3\,\text{fb}^{-1}$ are employed in this study. The low production probability has the additional disadvantage of high background rates, as many processes exist that are more likely to be produced in the collision. Therefore, effective background rejection criteria have to be defined in order to suppress the contributions from these processes.

Semi-leptonic $WW\gamma$ final states [2] have been studied in proton-proton collisions before, but their production probability could not be measured, as the signal was not sufficiently isolated from the background processes. The presence of two leptons in the final state considered here helps to reduce the background contribution from hadronic processes significantly. The production of the $WW\gamma$ process has also been studied in electron-positron collisions, where fully-leptonic, semi-leptonic and fully-hadronic final states were analysed [3]. These analyses tested lower energy regimes than are accessible with this analysis due to the lower collision energies. Therefore, the work presented here extends the measurements that were carried out

previously.

In the first chapter of this thesis, the theoretical description of the process and a possible extension of the Standard Model to which this process is sensitive, are introduced. The LHC and the ATLAS experiment are described in Chapter 2 as they provide the experimental infrastructure to this work. Methods and programs to simulate proton-proton collisions are outlined in Chapter 3 and the reconstruction of the particles using the information of the ATLAS detector components is described in Chapter 4.

Chapter 5 introduces the event selection, that requires the final state to contain an energetic electron, muon and photon. Only low energetic contributions from hadrons are allowed in the selected events to reduce hadronic background processes. Additionally, a certain momentum imbalance is required in the final state for further background suppression. The estimation of the remaining background components is detailed in Chapter 6 and used to extract the number of signal events in the selected data set. This number can be used to quantify the production probability of the $WW\gamma \to e\nu\mu\nu\gamma$ process by computing its cross-section as described in Chapter 7.

This analysis can also be used to constrain possible extensions of the Standard Model. To this end, frequentist exclusion limits are set at 95 % confidence level on so-called anomalous quartic gauge couplings described in the framework of effective field theory. The results are detailed in Chapter 8, where the limit computation is described for the couplings with and without unitarisation. More information about the event displayed in Figure 1 and other details of the analysis can be found in the appendix.

Author's Statement This work is performed in the framework of the ATLAS collaboration, an international community that together conceived, constructed and operates the ATLAS detector. The recording of the data analysed here is a common effort, as it requires full time supervision of the detector. The author contributed to this data taking efforts by taking on-site responsibilities for parts of the data acquisition and trigger system. In addition a tool for the monitoring of the fine timing of the Level-1 Calorimeter Trigger was developed and is constantly running during data taking to supervise the proper functioning of the system.

The analysis presented here is fully conceived and performed by the author and is reported to the ATLAS collaboration on several discussion platforms to assure its integrity. It is currently in the ATLAS-internal review and fully documented for the collaborators in Reference [4] with the goal of prompt publication. All analysis specific figures in this thesis are produced by the author using the ATLAS software framework. For all other figures the corresponding references are given.

Many methods and skills were obtained through the author's contribution to another measurement containing electroweak bosons; the analysis of final states with one leptonically decaying W boson and two photons, published in Reference [5]. It is not reported in this work, as the analysis was a common effort distributed among several analysers and the analysis strategy is similar to the one explained here. The author also contributed to the luminosity calibration efforts of the ATLAS experiment by studying non-linear effects observed in the Van der Meer scans of March 2011 taken with a centre-of-mass energy of $\sqrt{s} = 2.76\,\text{TeV}$. This study is described in detail in an ATLAS-internal document [6].

1 Theoretical Foundations

The basic building blocks of matter and their interactions, that are subject of study in this thesis, are described by the Standard Model of particle physics. The Standard Model was developed about 50 years ago and still yields a successful description of almost all experimental results. It is outlined in Section 1.1. A complete overview is given in various works of literature and this discussion follows References [7] and [8]. Section 1.2 concentrates on the electroweak aspect of the model and Section 1.3 describes the process of interest in this work: the production of two W bosons in association with a photon. In Section 1.4 an extension of the Standard Model in terms of anomalous quartic gauge couplings is introduced.

1.1 The Standard Model of Particle Physics

The Standard Model of particle physics is a relativistic quantum field theory that is based on the principle of local gauge invariance. It describes all elementary particles observed to date along with their interactions: the strong, the weak and the electromagnetic. Gravity is not included, and only plays a role on macroscopic scales, not in particle physics.

The particle content of the model can be grouped according to the intrinsic angular momentum of the particles, the spin. So far particles with spin 0, spin $1/2$ and spin 1 have been observed. They are referred to as Higgs bosons, fermions and gauge bosons respectively.

The Standard Model describes 12 fermions that can be grouped into two categories, called quarks and leptons, according to the interactions they are subject to. Leptons carry weak charge and can be arranged into three generations, each containing a massive lepton and an electrically neutral counterpart, the neutrino. The massive leptons carry one negative elementary electrical charge, and only differ in their mass which increases with the generation. They are called electron (e), muon (μ) and tau (τ) and the neutrinos are called electron neutrino (ν_e), muon neutrino (ν_μ) and tau neutrino (ν_τ) accordingly. This is depicted in the lower part of Table 1.1. Each fermion in the Standard Model has a corresponding antiparticle that has the exact same properties, but carries opposite charges.

The quarks are called up (u), down (d), charm (c), strange (s), top (t) and bottom (b) and are also summarized in Table 1.1. They all differ in mass and within one generation by one unit of the electric charge. Quarks are also subject to the strong force and thus carry the corresponding charge, called colour. The possible colour charges are named red, green and blue. Only colour neutral states, i.e. compound systems with colour and anticolour or with three different colours, have been observed to exist freely. This implies, that quarks only have been detected as bound states, called hadrons, so far. Hadrons can be divided into mesons, composed of a quark and an antiquark, and baryons, formed by three quarks that each carry a different colour charge.

Each force in the Standard Model is mediated by the exchange of a fundamental particle, a gauge boson, and is described by a quantum field theory. The theory of the strong interaction is called quantum chromodynamics and is based on the SU(3) gauge group. The gauge bosons

Particle	generation 1	2	3	electric charge [e]	colour charge	weak charge
Quarks	u	c	t	$+2/3$	✓	✓
	d	s	b	$-1/3$	✓	✓
Leptons	ν_e	ν_μ	ν_τ	0	-	✓
	e	μ	τ	-1	-	✓

Table 1.1: The twelve fermions of the Standard Model of particle physics. The electrical charge is given in units of the elementary electric charge $1\,\mathrm{e} = 1.6021766208(98) \times 10^{-19}\,\mathrm{C}$ [9].

are an octet of massless gluons each carrying colour and anticolour charge. Therefore, the gluons not only interact with quarks, but also with each other, leading to a limited range of the interaction. The strong coupling has the largest coupling constant, which means that it is the strongest of all forces at short distance.

Electromagnetism is described by quantum electrodynamics which has the U(1) gauge group as underlying symmetry. Its mediating particle is the photon, which is massless and uncharged. Therefore the interaction has an unlimited range, but it is still about two orders of magnitude weaker than the strong interaction.

The weak interaction is mediated by the W and the Z bosons and based on the SU(2) gauge group. These exchange bosons carry weak charge, but differ in their electrical charge. The W^+ boson carries one elementary charge, the W^- boson carries one negative elementary charge and the Z boson is electrically neutral. Since these bosons are massive, the range of the weak interaction is limited and the coupling is weaker than the electromagnetic or the strong interaction.

The Higgs boson is responsible for the generation of mass in the Standard Model. It was discovered in 2012 [11, 12] and is the only elementary particle with spin 0 that has been observed so far. Its coupling strength is proportional to the mass of the particles it interacts with. The existence of the Higgs boson explains the difference in mass between the heavy gauge bosons and the photon as it spontaneously breaks the electroweak symmetry.

The aforementioned particles and interactions compose the Standard Model of particle physics. It is depicted in Figure 1.1 which shows the particle content (black ovals) along with their respective couplings (blue lines).

There are many interesting aspects of the Standard Model, but for this thesis the most relevant one is the electroweak sector of the model. It describes the unification of the electromagnetic and weak interaction and is discussed in the following section.

1.2 Electroweak Interactions

The electromagnetic and the weak interaction can be understood as the low energy manifestations of one common force, the electroweak interaction. This unification was derived by Glashow, Salam and Weinberg in the 1960s. The underlying gauge symmetry is $\mathrm{U}(1)_Y \times \mathrm{SU}(2)_L$, where Y refers to the so-called weak hypercharge. The subscript L indicates, that only left handed particles interact weakly. These are particles whose spin projection along their direction of motion is negative, i.e. pointing backwards.

Analogous to classical mechanics, where the equation of motion of a particle can be obtained

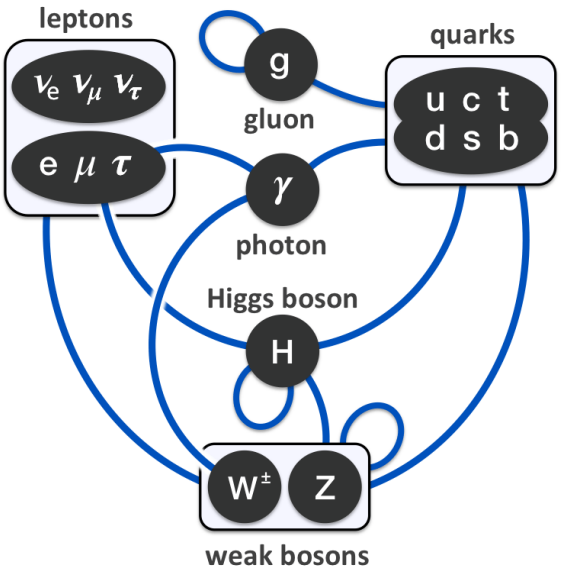

Figure 1.1: Particle content and interactions of the Standard Model. The particles are represented by black ovals and grouped into categories by the boxes. The possible interactions are indicated by blue lines. Interactions between single particles are indicated by lines connecting the black ovals. Lines connecting two boxes indicate, that interaction is possible between all particles in the given categories [10].

from the Euler-Lagrange equations, the dynamics of a quantum field theory are determined by the Lagrangian density $\mathcal{L}$, referred to as Lagrangian in the following discussion. In this picture, the fundamental particles are the excitations of a quantum field F_μ, where $\mu \in \{0, 1, 2, 3\}$ indicates the space time-coordinate and the zeroth component represents the time component.

The fact that the Standard Model is based on local gauge invariance can be incorporated by the introduction of three gauge fields, referred to as $W_\mu^{(1)}$, $W_\mu^{(2)}$ and $W_\mu^{(3)}$ in the following. And the $W^\pm$ gauge bosons can be written as linear combinations of these fields:

$$W_\mu^\pm = \frac{1}{\sqrt{2}}(W_\mu^{(1)} \mp W_\mu^{(2)}).$$

The third quantum field $W_\mu^{(3)}$ is electrically neutral and therefore mixes with the neutral field B_μ that is introduced due to the $\mathrm{U}(1)_Y$ gauge symmetry of electromagnetism. Linear combination of these two fields can be identified with the quantum field of the photon, A_μ, and the field Z_μ of the Z boson:

$$A_\mu = +B_\mu \cos\theta_W + W_\mu^{(3)} \sin\theta_W,$$
$$Z_\mu = -B_\mu \cos\theta_W + W_\mu^{(3)} \sin\theta_W,$$

where θ_W denotes the so-called weak mixing angle. This is a free parameter of the model and has to be determined experimentally.

The masses of the $W^\pm$ and Z bosons are generated by the introduction of a complex scalar field Φ. This field spontaneously breaks the gauge symmetry and its excitation is the spin 0 particle called Higgs boson.

The generators of the weak SU(2) gauge group, which can be expressed in terms of the Pauli spin matrices, do not commute and therefore the gauge theory is called non-Abelian. In order to preserve gauge invariance in non-Abelian theories, gauge boson self interaction terms have to be added to the Lagrangian. In the electroweak sector of the Standard Model these self couplings predict the interaction of three and four electroweak gauge bosons. They are referred to as triple and quartic gauge coupling vertices respectively. The Standard Model describes the two triple gauge coupling vertices γW^+W^- and ZW^+W^-. Furthermore, four quartic vertices are predicted, namely $W^+W^-W^+W^-$, W^+W^-ZZ, $W^+W^-\gamma\gamma$ and $W^+W^-Z\gamma$. They are highly relevant for this thesis and are described by the following part of the Standard Model Lagrangian [13]:

$$\begin{aligned}\mathcal{L}_{QGC} = &-\frac{g^2}{4}[(2W_\mu^+W^{-\mu} + (A_\mu \sin\theta_W - Z_\mu \cos\theta_W)^2)^2 \\ &- (W_\mu^+W_\nu^- + W_\nu^+W_\mu^- + (A_\mu \sin\theta_W - Z_\mu \cos\theta_W)(A_\nu \sin\theta_W - Z_\nu \cos\theta_W))^2],\end{aligned}$$

where g is the coupling constant, which is also a free parameter of the model. A vertex with only electrically neutral bosons is not described in the Standard Model, but can easily be added in extended models (see Section 1.4).

1.3 The $WW\gamma$ Process

In the description of the Standard Model of particle physics, the gauge boson self interactions are completely determined by the non-Abelian nature of the $\mathrm{U}(1)_Y \times \mathrm{SU}(2)_L$ gauge symmetry. Therefore, their measurement yields a valuable test of the gauge structure of the model. Furthermore, the electroweak symmetry breaking can be studied with these measurements, since the $W^\pm$ and Z bosons masses result from the spontaneous symmetry breaking [14].

To this end, this thesis analyses the production of events containing two W bosons with opposite electrical charge and a photon in proton-proton collisions. It is referred to as $WW\gamma$ process in the following and the sign of the $W^\pm$ boson is omitted for shorter notation when not specifically needed. The full process under study is $pp \to W^+W^-\gamma \to \nu_{l_1}\bar{l}_1\bar{\nu}_{l_2}l_2\gamma + X$, where both W bosons decay to a lepton and a corresponding neutrino. The term X stands for additional particles present in the final state. The leading order computation of this process yields 110 Feynman diagrams [15] that represent the various ways this final state can be obtained. They can be grouped in three categories according to the number of bosons that interact with the incoming quarks. This is depicted in Figure 1.2, where this number increases from 1 to 3 from left to right. The leftmost Feynman diagram in the figure depicts the quartic gauge interaction. Since either a Z boson or a photon can be the mediating particle, the production of $WW\gamma$ events includes the quartic vertices $W^+W^-\gamma\gamma$ and $W^+W^-Z\gamma$.

The processes depicted in Figure 1.2 only show so-called tree level or leading order diagrams. This implies, that only the first order in perturbation theory is considered. In quantum chromodynamics, each order of perturbation theory is suppressed by a factor proportional to $0 < \alpha_s < 1$, which means that the largest contribution to the production of a certain process is expected to come from the leading order terms. Still, substantial contributions can arise from higher order terms since new production mechanisms can be available for example due to the incorporation of particle loops. Also, the production at leading order might be suppressed

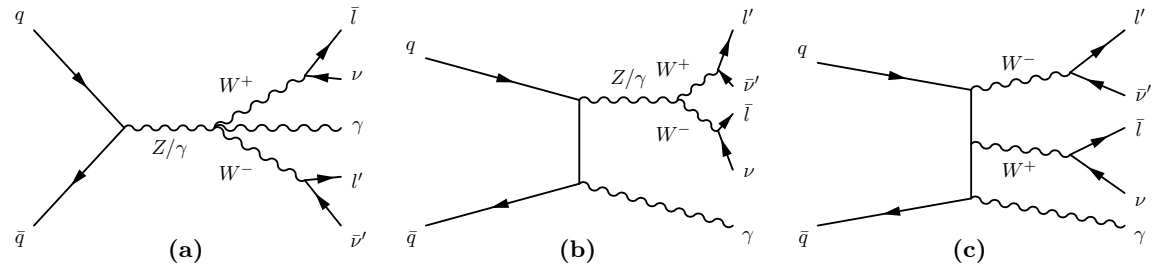

Figure 1.2: Examples of Feynman diagrams for $WW\gamma$ production. The left figure shows the quartic vertex where four bosons interact directly. The middle diagram depicts a process including a triple gauge boson interaction and the right figure features no direct gauge boson interaction.

due to conservation laws, which results in sizeable contributions from the higher order terms. For the $WW\gamma$ production, the next-to leading order terms in quantum chromodynamics have been computed [15] and found not to be negligible. This is expressed by a so-called k-factor that corresponds to the ratio of the production probabilities of a process computed at next-to leading order and at leading order.

Reference [15] also shows, that the next-to leading order terms affect the kinematic distributions of the final state particles, which means, that the k-factor is not constant, but varies with the energy of the photon. Therefore, in order to obtain reliable predictions, next-to leading order computations need to be used. This is also visible in Figure 1.3, where the differential cross-section is shown as a function of the transverse momentum, p_{T}, of the photon in the final state. The cross-section is a measure for the probability of a certain process to occur and is typically specified in units of barn: $1\,\mathrm{b} = 1 \cdot 10^{-28}\,\mathrm{m}^2$ [16]. Figure 1.3a shows the expected cross-section for the production of $WW\gamma$ events in proton collisions where the W bosons decay into a different flavour pair of light leptons, i.e. one electron and one muon. The computations are performed using the Monte Carlo generator VBFNLO (see Section 3.2); the leading order expectations are indicated by the round markers and the next-to-leading order expectations are indicated by the crosses. The lower panel of this figure shows the k-factor which is obtained by dividing the next-to-leading order cross-section by the leading-order computation. It shows a clear rise with increasing transverse photon momentum as presented in Reference [15]. Figure 1.3b shows the same observable, but no additional parton, i.e. quark or gluon, with a transverse momentum above 25 GeV is admitted in the final state. This corresponds to the phase space studied in this work, as it efficiently reduces the background containing top quarks as discussed in Section 5.4. Due to this additional requirement, the overall cross-section expectation is lower than in the inclusive case, but also the difference between the leading and next-to-leading order is smaller. This is indicated by a lower k-factor that is less dependent on the photon momentum.

The overall cross-section σ for the phase space considered in this thesis and detailed in Section 7.1 as shown in Figure 1.3b corresponds to:

$$\begin{aligned}\sigma^{\mathrm{LO}} &= (1.6899 \pm 0.0004)\,\mathrm{fb} \quad \text{and} \\ \sigma^{\mathrm{NLO}} &= (1.8113 \pm 0.0025)\,\mathrm{fb},\end{aligned}$$

where the uncertainty corresponds to the statistical uncertainty due to the computation only. Thus, the overall k-factor amounts to 1.07.

The $WW\gamma$ production cross-section has been measured in electron-positron collisions [3]

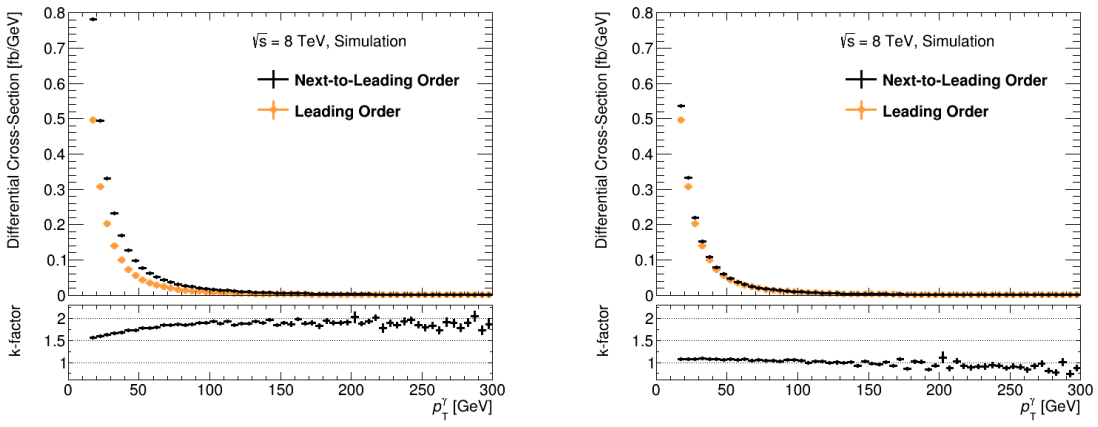

Figure 1.3: Differential cross-section as a function of the transverse photon momentum. Shown are the expectations for the production of $WW\gamma$ events in proton-proton collisions where the W bosons decay into a different flavour pair of light leptons. The cross-sections are computed at leading and at next to leading order using the VBFNLO [17–19] program. The figure on the right shows the differential cross-section without energetic partons in the final state. The lower panel of each figure shows the k-factor as a function of p_{T}^{γ}.

at centre-of-mass energies between 130 GeV and 209 GeV. This is complementary to the measurement of this cross-section using the proton-proton collisions provided by the LHC (see Section 2.1), where higher energy regimes are accessible. Semi-leptonic $WW\gamma$ final states, which means that one of the W bosons decays into two quarks, have been studied using the CMS detector [2]. Fully leptonic $WW\gamma$ final states presented in this thesis, have not been studied in hadron collisions before.

1.4 Anomalous Quartic Gauge Couplings

Although the Standard Model successfully describes numerous measurements, it has some shortcomings. For example, it has 25 free parameters [7] that have to be determined by measurements in order to give quantitative predictions. This is contrasting a fundamental theory which is purely based on symmetry principles and does not need fine tuning to the degree the current model requires. Another shortcoming of the Standard Model is, that it does not describe gravitational observations or the dark matter content of the universe. These weak points hint to the fact that the Standard Model might only be a low energy realisation of a Grand Unified Theory. Therefore, it is worthwhile to test the model with scrutiny to find possible extensions.

The measurement of the weak gauge boson self interactions yields a potential test of the Standard Model, since the $\mathrm{U}(1)_Y \times \mathrm{SU}(2)_L$ gauge symmetry completely determines the predictions for these couplings. The observation of any deviation from the Standard Model predictions would therefore directly hint to physics not described by the model [14], often called new physics.

High energy extensions of the Standard Model can be expressed by an effective field theory in a model independent way. This formalism is explained in References [20] and [21]

and is summarised in this section following their discussion. The additional interactions are incorporated in the theory by extending the Standard Model Lagrangian by a sum of higher dimensional operators, $\mathcal{O}$, which are the product of quantum fields:

$$\begin{aligned}\mathcal{L}_{eff} &= \mathcal{L}_{SM} + \mathcal{L}_{aQGC} \\ &= \mathcal{L}_{SM} + \sum_{d>4} \sum_{i} \frac{f_i}{\Lambda^{d-4}} \mathcal{O}_i,\end{aligned} \tag{1.1}$$

with d being the mass dimension of the operators and $\mathcal{L}_{eff}$ is referred to as effective Lagrangian. The dimensionless coupling parameters f_i determine the strength of the coupling $\mathcal{O}_i$, where i indicates a specific operator. The operators describe the additional couplings, which are referred to as anomalous, since they are not included in the Standard Model. They are chosen to be invariant under the symmetries of the Standard Model and suppressed by multiples of the energy scale Λ at which the new physics is supposed to occur. This scale needs to be larger than the energies tested experimentally, for the theory to work. For $\Lambda \to \infty$ the additional terms vanish and the Standard Model Lagrangian is recovered. The Standard Model expectation values of f_i are zero. Depending on the extent of the expansion the index i can become arbitrarily large.

Operators of uneven mass dimension are discarded in this discussion as they would lead to couplings that do not conserve baryon or lepton numbers. Therefore, the lowest dimensions of operators that contribute to this extension of the Standard Model are $d = 6$ and $d = 8$, since $\mathcal{L}_{SM}$ contains operators up to a dimension of 4. As the higher dimensional couplings are suppressed by a factor of $1/\Lambda$ with respect to the next lower dimensional ones, the dimension-6 and dimension-8 operators have the strongest potential contribution and are the only ones considered in the following.

A minimal set of 10 independent operators of dimension 6 can be found that express the interaction of three and four electroweak gauge bosons. Yet they do not describe all possible quartic interactions, like the coupling of neutral gauge bosons. But these can be included in the theory using dimension-8 operators. Dimension-8 operators have the additional advantage, that they can describe quartic interactions, while leaving the double and triple gauge boson vertices unchanged, which is one possible observable scenario.

18 genuine dimension-8 operators can be found of which 14 are accessible by the study of $WW\gamma$ events discussed in this thesis. Therefore, Equation (1.1) can be reduced to

$$\mathcal{L}_{eff} = \mathcal{L}_{SM} + \sum_{j=0}^{7} \frac{f_{M,j}}{\Lambda^4} \mathcal{O}_{M,j} + \sum_{j=0,1,2,5,6,7} \frac{f_{T,j}}{\Lambda^4} \mathcal{O}_{T,j} \tag{1.2}$$

for the purposes of this discussion. The naming convention from Reference [22] is followed and the operators $\mathcal{O}_{M,j}$ and $\mathcal{O}_{T,j}$ are given in Appendix A.2 for completeness. It is sufficient to note here, that they all describe the $W^+W^-\gamma\gamma$ and $W^+W^-Z\gamma$ vertices which are accessible with the study of $WW\gamma$ production.

Especially, if the new physics comprises an additional heavy boson, quartic vertices could be significantly more enhanced than triple gauge coupling vertices. This is because the heavy boson can be exchanged at leading order when four gauge bosons take part in the interaction, while it would only contribute a next-to leading order correction to the three boson vertex, leading to a suppression [22]. This is shown in Figure 1.4, where the quartic and the triple gauge coupling vertices, that are described as contact interactions in the Standard Model and

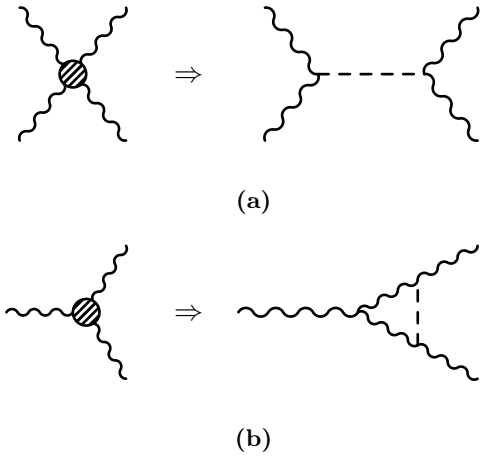

Figure 1.4: Feynman-style diagrams for possible interactions involving bosons not included in the Standard Model, depicted by dashed lines. The left diagram in Figure a) shows the contact interaction of four gauge bosons indicated by the hatched circle. In new physics scenarios this vertex can have a tree level contribution from the additional boson as is shown on the right hand side. Figure b) shows the same situation for the interaction of three gauge bosons. Here, the new particle can only enter at the one loop level, which suppresses its contribution.

depicted as the hatched circles, are resolved and get an additional contribution from a new boson.

Depending on the realisation of the new physics, the stronger enhancement of the quartic vertex with respect to the triple vertex can overcome the lower production probability of three boson events with respect to diboson production. This makes the study of three boson processes worthy although they are experimentally more challenging than diboson events due to the higher object multiplicity and rarer occurrence. Once anomalous quartic gauge couplings are observed, it is interesting to know which specific vertex is enhanced. This can be achieved by studying several triboson final states, as the quartic vertices have contributions from different operators. Therefore, the knowledge which of the processes exhibits an increased production yields important information on the type of enhanced vertex. This allows conclusions about the dynamics of the new physics [22].

The observation of new physics in triboson production has an advantage above direct searches: Since the final state is populated by Standard Model particles only, the new particles would occur as virtual particles mediating the new interaction. This implies that they do not have to be produced on the mass shell, i.e. the energy needed to produce them can be lower than their rest mass. In direct searches, where the new physics particle is observed in the final state, the particle has to be on its mass shell and therefore more energy is needed to produce it. Due to of this fact, indirect new physics searches complement direct searches, allowing to probe higher energies.

1.4.1 Unitarity Conservation

The concept of effective field theories is only valid when describing the dynamics below the scale of new physics, Λ. At large energy scales $\hat{s}$, the higher dimensional operators are no longer suppressed, since the suppression is proportional to $\hat{s}/\Lambda$. Therefore, additional couplings

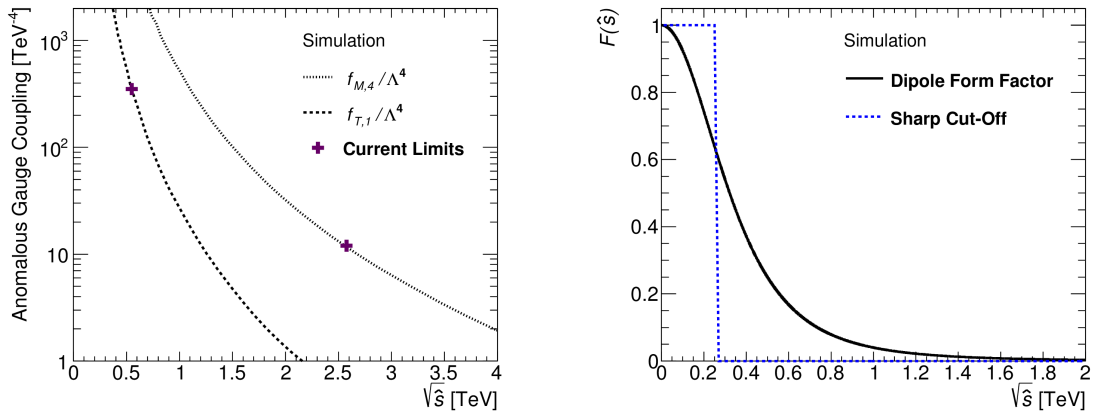

(a) **(b)**

Figure 1.5: Left: Unitarity bound as a function of the square-root of the tested energy scale $\hat{s}$. Two different anomalous quartic couplings are shown along with the current best exclusion limit [23, 24]. Right: Comparison of a dipole form factor and a sharp energy cut-off with $\Lambda_{FF} = 0.5\,\text{TeV}$.

become sizeable and the quantum mechanical unitarity can be violated. This means that the probability to produce a given particle can be larger than one, which is unphysical.

A prominent example of unitarity violation is the scattering of four W bosons. The probability of the process $W^+W^- \to W^+W^-$ is only below one, if the Feynman diagrams including the Higgs boson as a mediator are taken into account. This was a strong motivation for the existence of this particle even before it was found. A similar mechanism, the existence of an additional particle at the energy scale Λ, can restore unitarity also for effective field theories.

At hadron colliders, only energies below the centre-of mass energy of the collisions are probed. Still, these might be at the order of Λ, since new physics can already be expected in the TeV range. This is depicted for two examples of anomalous quartic gauge couplings in Figure 1.5a. The unitarity bound is shown for each coupling as a function of the scale $\sqrt{\hat{s}}$ that is probed in the interaction. All coupling values larger than the unitarity bound for the specific coupling violate unitarity at this scale. The curves are computed with a tool provided with the VBFNLO program that is further described in Section 8.3.2. Also shown are the current best upper limits on the two couplings [23, 24], that leave room for unitarity violation far below $\sqrt{\hat{s}} = 8\,\text{TeV}$.

An energy dependent cut-off can be introduced in order to restore unitarity. This ensures that no sensitivity to anomalous coupling parameters comes from the energy regime where the unitarity is violated. Technically this is done by multiplying the coupling parameters f_i of the effective Lagrangian by a form factor $F(\hat{s})$ that vanishes for large energies $\hat{s}$. The choice of the form factor is not unique, as several realisations are conceivable. A sharp cut-off above a certain energy Λ_{cut} is one option, where the form factor is zero for $\hat{s} > \Lambda_{cut}$. Then $F(\hat{s})$ can be written as

$$F(\hat{s}) = \Theta(\Lambda_{FF}^2 - \hat{s}), \tag{1.3}$$

where Θ is the Heaviside step function and Λ_{FF} is called the form factor scale. It is related to the cut-off scale via $\Lambda_{FF}^2 = \Lambda_{cut}$. In VBFNLO a smoother cut-off is employed by choosing a

form factor shape according to:

$$F(\hat{s}) = \left(1 + \frac{\hat{s}}{\Lambda_{FF}^2}\right)^{-p}, \tag{1.4}$$

where the parameter p is the cut-off power of the damping and is usually set to 2 for analyses including operators of dimension 8. This form factor with $p = 2$ is called dipole form factor and compared to the sharp cut-off in Figure 1.5b with $\Lambda_{FF} = 0.5\,\text{TeV}$.

The form factor scale Λ_{FF} needs to be chosen depending on the coupling parameter in question, in order for it not to violate its unitarity bound. VBFNLO provides the possibility to compute this value and apply the form factor in the simulation. This way unitarity is restored and meaningful values obtained.

The data always exhibit unitarity conserving behaviour. Therefore, once the energy regime of new physics is reached, the effective field theory with $\Lambda \sim \hat{s}$ is no longer applicable and a new theory incorporating the new particles is needed. Until then, the effective field theory approach yields a model independent way of describing the data and also provides a framework in which new physics effects exclusions can be quantified. This is done by setting exclusion limits on the anomalous coupling parameters divided by the energy scale, f_i/Λ^4.

2 Experimental Setup

The proton-proton collisions analysed in this thesis were recorded with the ATLAS detector that is located at the LHC, in Switzerland near Geneva. To date, the LHC is the most powerful hadron collider and puts the experiments in a unique position to probe particle collisions at the highest energies ever reached. In Section 2.1, an overview of the LHC is given following the detailed description in Reference [25]. Section 2.2 focuses on the ATLAS detector and its different subcomponents using Reference [26] .

2.1 The Large Hadron Collider

The LHC is a machine to accelerate and collide two counter rotating beams of hadrons based on superconducting technology. It is 26.7 km long and fully located in a tunnel underground at an approximate depth of 100 m. The tunnel was built in the 1980s for the Large Electron–Positron Collider, LEP [27], an electron-positron accelerator that provided particle collisions at lower energies than the LHC.

The beams of the LHC can either consist of protons or heavy ions, but only proton-proton collisions are considered in this work. The protons are accelerated stepwise by a chain of linear- and ring-accelerators depicted in Figure 2.1. Some of the accelerators existed long before the LHC was built. They had successful physics programs and still supply other experiments with high energetic particles when they are not used for pre-acceleration of particles for the LHC.

The maximum centre-of mass energy of the proton collisions the LHC is built to deliver is $\sqrt{s} = 14\,\text{TeV}$ and has never been reached in a man-made particle collision yet. These energies are attainable by using a superconducting radio frequency cavity system for the acceleration and storage of the particles. Due to the repeated use of these cavities in ring accelerators, the particles in the LHC beam are grouped in bunches and are not continuous. The magnetic field for the deflection of the protons is generated by superconducting niobium-titanium magnets that are cooled to a temperature of 1.9 K using suprafluid helium. This way, they are able to provide magnetic fields of 8.3 T and allow the LHC to reach the high collision energies. The centre-of mass energy is increased gradually since the start of the LHC running in 2009 with three major data taking campaigns for proton-proton collisions with a collision energy of 7, 8 and 13 TeV. Proton collisions with $\sqrt{s} = 14\,\text{TeV}$ will be reached in the coming years.

The LHC beams intersect at four collision points, each enclosed by a detector to analyse the particles produced in the interaction. The location of these experiments are indicated in Figure 2.1 and the experiments are:

- ALICE [29], a detector specialised for the analysis of heavy ion collisions and the investigation of the strong sector of the Standard Model of particle physics.

- ATLAS [26], an experiment designed to reconstruct the particle collision in the most complete way achievable in order to measure Standard Model processes and to search for new phenomena.

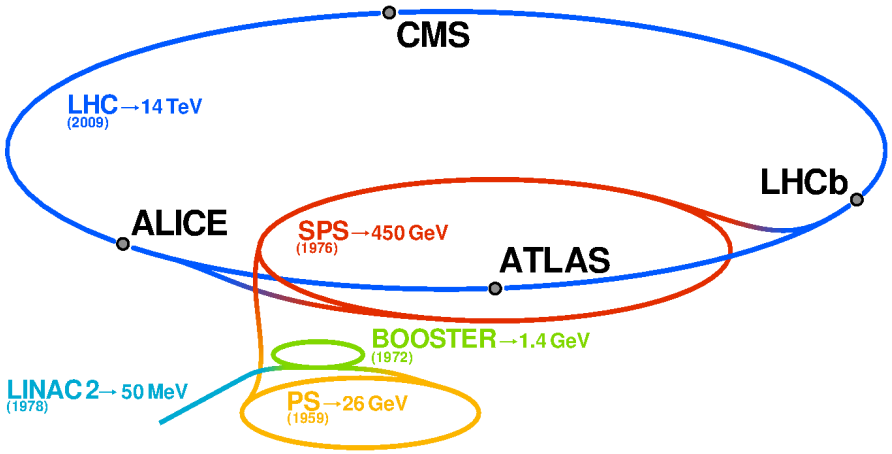

Figure 2.1: The accelerator complex at CERN. The protons colliding in the LHC are first accelerated by the linear accelerator LINAC 2 and increase their velocity gradually by passing the accelerators BOOSTER, PS and SPS. The beam energies reached by each accelerators are given along with the year of first operation. The location of the four main experiments, ALICE, ATLAS, CMS and LHCb, are indicated along the LHC ring [28].

- CMS [30], also a multipurpose detector like ATLAS, with the same physics goals, but with a different technical realisation.
- LHCb [31], an experiment to study the violation of the CP symmetry predicted by the Standard Model as well as hadron decays including a b-quark.

Not only the energy of the particles in the ring is unprecedented, but also the luminosity of the beams. The luminosity is a measure for the amount of particle collisions to occur. In collider experiments this quantity depends on the beam parameters: N_i the number of particles in beam $i \in \{1, 2\}$, A, the cross-section of the beam and f, the revolution frequency. The instantaneous luminosity is defined as:

$$\mathrm{L} = \frac{N_1 \cdot N_2 \cdot f}{A} \tag{2.1}$$

and since it is proportional to the total number of circulating particles, it decreases over time when collisions take place and remove particles from the beams. The design luminosity of the LHC is $\mathrm{L} = 10^{34}\,\mathrm{cm}^{-2}\mathrm{s}^{-1}$. The advantage of high instantaneous luminosity is that many particle collisions can be recorded in a certain time interval. Since the production probability of many interesting physics processes is rather low, a high number of collisions is needed in order to obtain a significant sample. The disadvantage of a high luminosity is that several particle collisions can occur simultaneously and therefore overlap. This so-called pile-up is one challenge for the LHC experiments. The amount of particle collisions in a given time interval is given by the integrated Luminosity, $\mathrm{L}_{\mathrm{int.}} = \int \mathrm{L}\mathrm{d}t$.

For the analysis in this thesis, proton-proton collisions recorded in the year 2012 at a centre-of mass energy of $\sqrt{s} = 8\,\mathrm{TeV}$ corresponding to an integrated luminosity of $\mathrm{L}_{\mathrm{int.}} = 20.3\,\mathrm{fb}^{-1}$ are used. The peak instantaneous luminosity is $\mathrm{L} = 7.7 \times 10^{33}\,\mathrm{cm}^{-2}\mathrm{s}^{-1}$ with an average of 21 simultaneous proton-proton collisions. Still, the major uncertainty of the final result is of statistical nature, meaning that the analysis could have benefited from an even larger data set. The data was recorded with the ATLAS detector that is subject of the next section.

2.2 The ATLAS Experiment

The ATLAS collaboration consists of over 3000 scientists from 174 institutions in 38 countries. This large international effort allows to design, build and operate a particle detector to study the high energy territory available at the LHC. Conceived in the late eighties and nineties of the last century [32] and ready for operation since 2008, the detector has the typical onion shell structure of a multi-purpose detector allowing to study numerous final states, including signatures of particles that have not been observed before.

The ATLAS detector is located at the interaction point 1 of the LHC in an underground cavern. The coordinate system used for its description has the origin at the collision point with the z-axis coinciding with the beam direction. The x-y-plane is defined transverse to the beam with the positive y-axis pointing upwards and the positive x-axis pointing to the centre of the LHC ring. Transverse quantities, like the transverse momentum p_{T} or transverse energy E_{T}, are defined in this plane. The azimuthal angle ϕ is measured around the z-axis and the polar angle θ corresponds to the angle from the z-axis. This angle is employed to define a more commonly used quantity, the pseudorapidity $\eta = -\ln\tan(\theta/2)$. Distances between two objects are stated in the pseudorapidity-azimuthal angle space as $\Delta R = \sqrt{\Delta\eta^2 + \Delta\phi^2}$, where $\Delta\eta$ and $\Delta\phi$ are the pseudorapidity and azimuthal difference of the objects.

The detector is designed in order to suit the physics program [33] of the ATLAS collaboration in the best possible way. One of the main targets was the search for the Higgs boson predicted by the Standard Model. Before the start of the LHC, limits on its mass had been set, but the particle itself had not been discovered. The production and decay of this boson strongly depends on its mass, which was unknown at the time of conception of ATLAS. Therefore, the detector design was optimised to cover the broad spectrum of possible final states of Higgs decays. This was rewarded with the successful observation of the boson by the ATLAS [11] and CMS [12] collaborations in July 2012, just three years after the initial start up of the LHC.

The ATLAS detector is also designed to precisely measure other Standard Model processes. While the particles themselves were measured before, the LHC allows the observation of processes that have not been accessible previously. For example in the field of quartic gauge boson couplings, the scattering of four W bosons with the same electrical charge has been observed with ATLAS for the first time [34], as well as the production of a W boson in association with two photons [5]. Also a higher precision in the measurement of the known Standard Model particles, like the W boson and top quark mass, can be achieved with the ATLAS detector. Therefore, an excellent object identification with the possibility to observe secondary vertices and precise momentum resolution was implemented.

Another key physics aspect of the ATLAS program is the search for particles that are not described by the Standard Model. These include, for example, heavy copies of the W and Z bosons, which decay leptonically and therefore require good lepton measuring capabilities over wide ranges of energy. Composite quarks would reveal themselves in an increased quark production measured by the reconstruction of so-called jets. These are sprays of hadrons produced by the quarks when building colour neutral objects. The detector needs to be able to measure jets up to momenta of the order of TeV. Other Standard Model extensions like Supersymmetry [35] or extra dimensions [36] predict particles that are not interacting with the detector material. They still leave traces in form of momentum imbalance called missing transverse energy, $E_{\mathrm{T}}^{\mathrm{miss}}$. A good momentum resolution is needed to detect this. Extra dimensions also predict mini black holes that decay into final states with multiple particles. A good spacial resolution of the detector is therefore needed in order to resolve these and

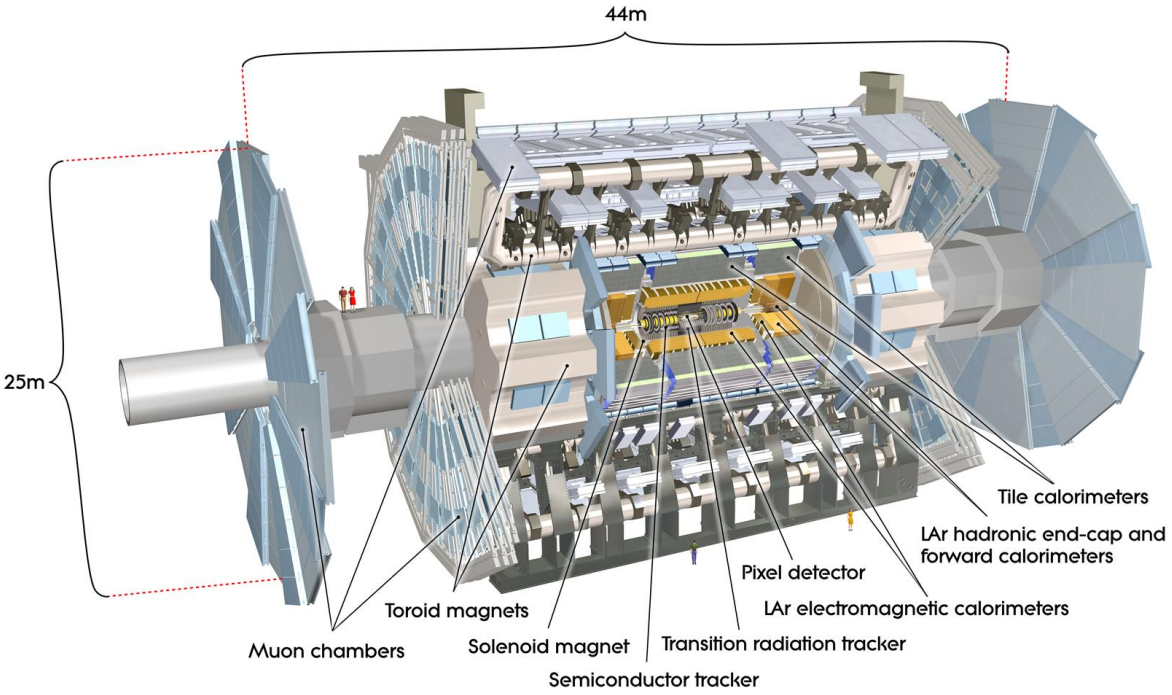

Figure 2.2: Layout of the ATLAS detector with cut-away view. The subcomponents of the detector are shown along with its dimensions [26].

separate them from pile-up events.

All these measurements furthermore require a large coverage of the detector to reconstruct the majority of the outgoing particles. Especially the azimuthal angle needs to be fully instrumented, to be able to measure the quantities transverse to the beam correctly. Since the detector is located at the LHC which provides collisions with highest luminosities, all detector components have to be radiation hard to guarantee a stable operation over time.

The concept of triggering allows the detector to cope with high instantaneous luminosities by only recording events that were accepted by several consecutive filters and discarding the others. This is feasible, as most processes under study with the ATLAS detector have low production probabilities but the particles in the final state have high momenta, since they originate from a so-called hard-scattering process. This feature is used by the trigger in order to distinguish them from the multitude of events that occur but do not have a large momentum transfer.

All theses considerations were made when planning the ATLAS detector. The final design is a cylinder shaped machine that is forward-backward symmetric with respect to the collision point. The detector is 44 m long, has a diameter of 25 m and weighs approximately 7000 t. It consists of several subsystems that are specialised in different aspects of particle measurements; these are depicted in Figure 2.2. From the inside out the subcomponents of the ATLAS detectors are: the inner detector surrounded by a solenoid magnet, the electromagnetic and the hadronic calorimeter and the muon system together with the toroid magnets.

In the years 2013 and 2014 several components of the detector underwent an upgrade after the completion of the first data taking period, called LHC Run 1. Since this thesis analyses

data that were recorded in 2012, the layout of the detector before these upgrade efforts is described in the following sections.

2.2.1 The Magnet System

The measurement principle of the inner detector and the muon system relies on the curvature of charged particles in a magnetic field. Therefore, each system has its dedicated superconducting magnet system operating at about 4.5 K.

The innermost magnet is the solenoid located inside the calorimeters as depicted in Figure 2.2. It is a cylinder aligned with the beam axis and made of an aluminium stabilised niobium-titanium conductor. This material was chosen to achieve a high magnetic field strength with a minimal material budget in order to avoid energy absorption in the magnet causing dilution of the energy measurement in the calorimeters. The solenoids thickness corresponds to a radiation length of $0.66\,X_0$. One radiation length is the average distance an electron can travel until its energy is reduced to $1/e$ of the starting value due to interactions with the material. The solenoid is realised as a single layer coil and yields an axial magnetic field of 2 T for the inner detector. This field leads to a deflection of charged particles in the x-y-plane. The solenoid is 5.8 m long and has a diameter of 2.56 m. Its magnetic flux is returned via the calorimeters.

The magnetic field for the muon system is provided by three toroid magnets also shown in Figure 2.2: the barrel toroid covers the central part of the detector and two end-cap toroids optimise the bending power in the high-η region. The layout of the three systems is similar, as each magnet consists of 8 air core coils to minimize multiple scattering. The coils are made of an aluminium stabilised alloy of niobium, titanium and copper providing a field in which charged particles are bent in the R-z-plane. The barrel toroid is the largest of the three and is 25.2 m long with an outer diameter of 20.1 m. It provides a toroidal field of 0.5 T in the region of $|\eta| < 1.4$. The two end-cap toroids are nested between either end of the barrel magnet. They are 5 m long and 10.7 m wide and provide a field of 1 T in the region $1.6 < |\eta| < 2.7$. The magnetic field in the region $1.4 < |\eta| < 1.6$ is a superposition of fields of the barrel and the end-cap magnets. The toroid field is constantly monitored by several hundred Hall sensors to assure a stable magnetic field needed for precise muon measurement.

2.2.2 The Inner Detector

The inner detector of the ATLAS experiment is designed for the precise momentum measurement of charged particle tracks with $p_{\mathrm{T}} > 0.5\,\mathrm{GeV}$. This also provides the ability to determine the position of the primary collision point as well as so-called secondary vertices, where particles produced in the hard interaction decay. Furthermore, the inner detector provides electron identification for transverse electron momenta between 0.5 and 150 GeV. To achieve this, the inner detector consists of a combination of three independent systems: a central silicon pixel detector surrounded by layers of silicon microstrips which are located in a transition radiation tracker. This is shown in Figure 2.2 and Figure 2.3. Each system itself is segmented in a cylindrical central barrel region and the so-called end-cap regions, where the components are arranged in wheels transverse to the beam line. The inner detector is 6.2 m long and has a diameter of 2.1 m. Since its detection principle is based on ionisation, only charged particles are measurable. This is done by reconstructing their trajectory using the position information provided by the single detector components.

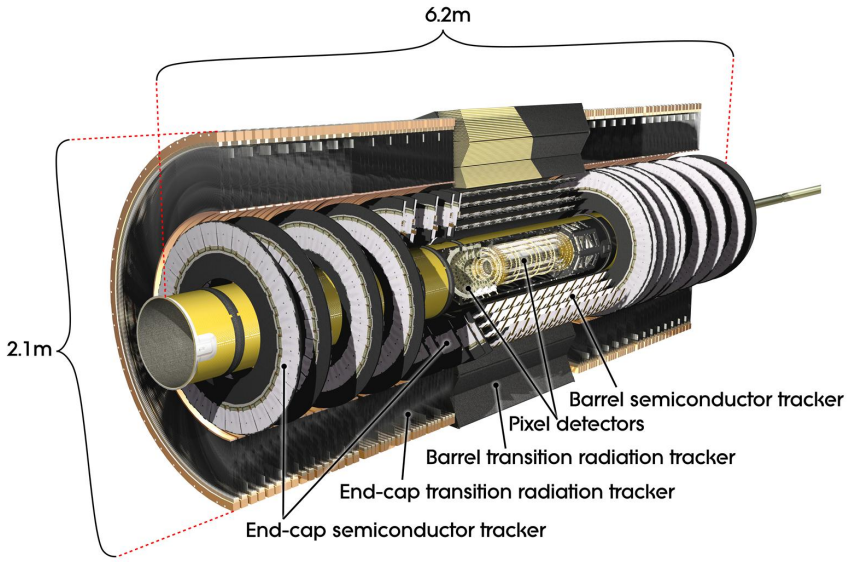

Figure 2.3: Layout of the ATLAS inner detector with cut-away view. The dimensions of the detector are indicated as well as its subcomponents [26].

The silicon pixel and microstrip sensors cover the range of $|\eta| < 2.5$. They are operated at a temperature of -5 to $-10\,^{\circ}\mathrm{C}$ in order to have low noise even with radiation damage due to the proximity of these components to the interaction point. As the particles traverse the inner detector before their energy is determined in the calorimeters, a minimal material budget is required to avoid dilution of the measurement by energy loss in the material and multiple scattering. The pixel and microstrip sensors are made of semiconducting silicon whose depletion zones are ionized by the traversing charged particles. This leads to an electronic signal in the sensor which is translated into a spacepoint whose resolution depends on the dimensions of the sensor. The spacepoints are combined to tracks that are bent due to the magnetic field of the solenoid. The momentum and charge of the track can be extracted from its curvature since they are connected via the Lorentz force.

The component closest to the beryllium beam pipe is the silicon pixel detector, since it has the best resolution of the system. It consists of three cylindrical barrel layers, with the innermost being about 5 cm away from the nominal interaction vertex, and of 6 wheels, 3 at each end. The minimum pixel size in R-$\phi \times z$ is $50 \times 400\,\mu\mathrm{m}^2$, providing an intrinsic accuracy of $10\,\mu$m in R-ϕ and $115\,\mu$m in z in the barrel and in R in the end-cap region.

The silicon microstrip detector encloses the pixel layers and yields typically 4 spacepoints per particle track, since it consists of 4 stereo strip layers in the barrel and 18 wheels. Each silicon strip is 6.4 cm long and $80\,\mu$m wide. In the stereo layers, one strip is axially aligned with the z-axis and the opposing strip is at a 40 mrad angle with respect to the first one in order to increase the resolution. For the end-cap wheels, the strips are aligned radially and also have a set of stereo strips with a 40 mrad angle. The intrinsic accuracy per module reached with this setup is $17\,\mu$m in R-ϕ and $580\,\mu$m in z in the barrel part and in R in the region of the end caps.

The transition radiation tracker constitutes the outer part of the inner detector. It is made of gas filled straw tubes interleaved with polypropylene and extends up to $|\eta| = 2$. It

typically yields 36 hits per charged particle track which significantly improves the momentum measurement, since the track length is largely extended. The straw tubes have a diameter of 4 mm and are filled with a gas mixture of xenon, carbon dioxide, and oxygen which is ionized by a passing particle. A gold plated tungsten wire runs trough the centre of the tubes and serves as anode that picks up the ionisation charges indicating a signal. The tubes in the barrel are 144 cm long and have anodes segmented in two halves, but they do not contribute to the resolution in the z direction. The end-cap tubes are 37 cm long, but again only the R-ϕ information is relevant. The intrinsic accuracy per straw is 130 μm. The tracker is operated at room temperature.

Besides tracking information, the transition radiation detector also yields electron identification information complementary to the one obtained by the calorimeter. This is achieved by using polypropylene as transition radiation material between the straw tubes. Electrons and hadrons passing this material both emit X-ray photons, but due to the mass difference, the electron signal is higher and thus the particles can be discriminated. The signal amplitude of low energetic transition radiation in the straw tubes is much larger than the one of minimal ionising particles, which is how the two signals can be distinguished.

The design resolution of the charged track momentum measurement for the inner detector is $\sigma_{p_\mathrm{T}}/p_\mathrm{T} = 0.05\,\% \, p_\mathrm{T}\,[\mathrm{GeV}] \oplus 1\,\%$ and has been experimentally determined to be $\sigma_p/p = (0.0483 \pm 0.0016)\,\% \, p_\mathrm{T}\,[\mathrm{GeV}]$ for high momentum tracks [37].

2.2.3 The Calorimeters

The ATLAS calorimeter system is employed for precise energy measurements of electrons, photons, τ leptons and jets up to $|\eta| < 4.9$. It is also used to measure the missing transverse momentum and is independent of the momentum measurement of the other systems. The inner part up to $|\eta| < 2.5$ is used for precision measurement of electrons and photons which profits from a finer granularity of the calorimeter in that region and from the fact that the tracks of the inner detector can be matched to calorimeter energy deposits. The ATLAS calorimeters are realised as so-called sampling calorimeters where an active material to measure the energy of particles is alternating with an absorber to decelerate the particles and induce the so called showering of the particles. This term describes the process during which, the initial particle creates secondary particles that in turn also create showers of new particles or ionise the material until the energy of the single particles is too low and the process dies out. These showers need to be completely contained in the calorimeter volume for a precise energy measurement and are reconstructed as so-called energy clusters. Their shape can also be used for particle identification. Therefore, the calorimeters are designed to have a large material budget in contrast to the design guidelines of the inner detector. Thus materials with high atomic numbers are employed. The electromagnetic calorimeter yields about 22 radiation lengths, X_0 and the end of the hadronic calorimeter corresponds to about 9.7 interaction lengths, λ; where λ is the mean free path of a strongly interacting particle in matter due to nuclear interactions with the material. The calorimeter system is cylinder symmetric and covers the full azimuthal angle ϕ; it is shown in Figure 2.2 and Figure 2.4. The ATLAS calorimeter system can be divided into several subsystems that use either liquid argon or scintillating tiles as active material.

The electromagnetic calorimeter is the innermost component of the system and has the objective to precisely measure electrons and photons. It is divided into a barrel component with $|\eta| < 1.475$ and two end-caps at $1.375 < |\eta| < 3.2$. The electromagnetic calorimeter uses

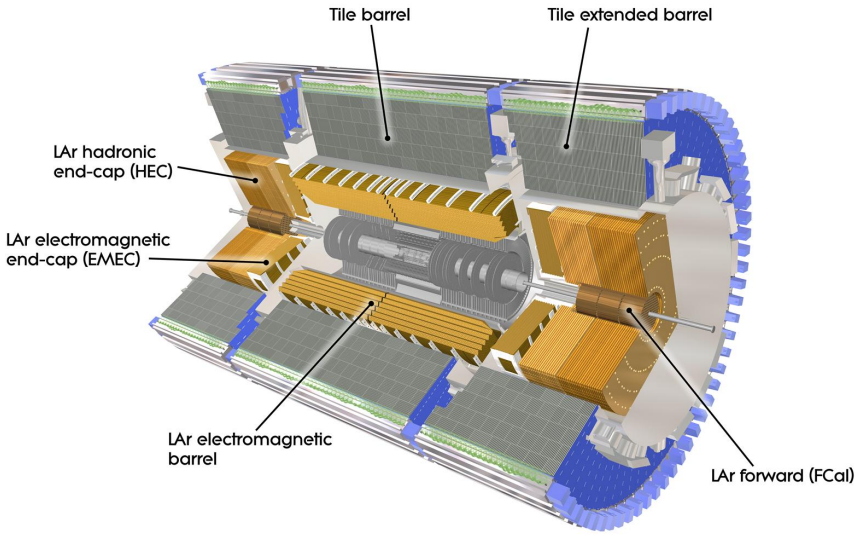

Figure 2.4: Layout of the ATLAS calorimeter system with cut-away view. Both the electromagnetic and the hadronic detector components are shown [26].

liquid argon as active material between accordion shaped lead absorbers and kapton electrodes that allow for full azimuthal symmetry without cracks. This calorimeter is segmented into three layers with varying granularity in the region $|\eta| < 2.5$. To precisely measure the position of the incoming objects, especially the photons, the first layer is finely segmented in η. This gives the calorimeter cells a strip like shape, and the layer is called strip layer. The fine segmentation allows to discriminate photons from neutral mesons made of light quarks, called π^0. These predominantly decay into a pair of photons whose signature can be resolved the better the smaller the cell size. In the middle layer of this calorimeter, most of the energy of electromagnetic particles is deposited as it is the thickest layer with $16\,X_0$. The back layer only constitutes two radiation length and can provide additional information about the depth and the shape of the particle shower. The region up to $|\eta| < 1.8$ is instrumented with an additional inner layer of liquid argon to correct for the energy the objects loose due to interaction with material before they arrive in the calorimeter.

The hadronic calorimeter, that surrounds the central part of the electromagnetic component, consists of steel absorbers and polystyrene tiles that serve as scintillators. Passing particles cause the emission of scintillation light in the tiles that is measured by photomultiplier tubes via wavelength shifting fibres. The hadronic calorimeter is also divided in three transverse layers and into a barrel and two extended barrels in z-direction. Its main objective is to measure particle showers from hadrons. It is completed by the hadronic end-caps that are located between $|\eta| = 1.5$ and $|\eta| = 3.2$. They consist of liquid argon between copper plates due to the different radiation conditions in this region.

The forward calorimeter is located at $3.1 < |\eta| < 4.9$ in the so-called forward region of the detector. It consists of three wheels on either end of the barrel part. The forward calorimeter utilises liquid argon between copper and tungsten absorbers to extend the coverage of the calorimeter system to large values of η.

The design resolution of the electromagnetic calorimeter is $\sigma_E/E = 10\,\%/\sqrt{E[GeV]} \oplus 0.7\,\%$

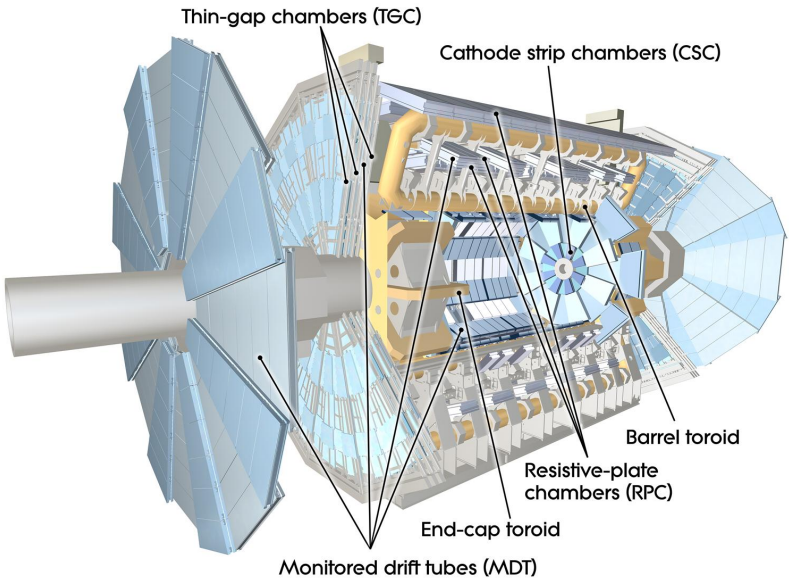

Figure 2.5: Layout of the ATLAS muon system with cut-away view. The four different muon chamber types are indicated along with the toroid magnets [26].

and was confirmed in test beam measurements already before the installation [38]. For hadronic objects, i.e. jets, the energy resolution goal is $\sigma_E/E = 50\,\%/\sqrt{E[GeV]} \oplus 3\,\%$ in the barrel region. Test beam measurements nearly reached this target [39, 40]. The energy resolution in the forward region is $\sigma_E/E = 100\,\%/\sqrt{E[GeV]} \oplus 10\,\%$ [41].

2.2.4 The Muon System

The ATLAS muon system together with the toroid magnets constitutes a standalone detector for precise muon measurement and triggering of the readout. In practise, the information of this system is combined with the measurements of the other subcomponents of ATLAS for optimal performance. The measurement principle is again tracking based on ionisation, but using different technologies than for the inner detector. The muon system is shown in Figure 2.2 and Figure 2.5 and makes up the majority of the detector volume. It covers $|\eta| < 2.7$ and relies on the fact that muons are not stopped in the calorimeter system and only deposit little energy there. The system is again divided into a cylindrical barrel part consisting of 3 layers of muon chambers and of end-cap wheels perpendicular to the beam. Four different types of ionisation detectors are used: monitored drift tube and cathode strip chambers for precise coordinate measurement in the bending plane, and resistive plate and thin gap chambers specialised in triggering.

The monitored drift tubes consist of several layers of tubes with a diameter of 30 mm. The tubes are filled with a mixture of argon and carbon dioxide which gets ionized by a passing particle. The charges are collected by a tungsten-rhenium anode and a 35 μm resolution is obtained per chamber. The cathode strip chambers are used in the innermost layer at $2.0 < |\eta| < 2.7$, since a higher rate capability and time resolution is needed in this region due to the higher particle flux. They are realised as multiwire proportional chambers with segmented cathodes also using a gas mix of argon and carbon dioxide. Their position resolution in the

bending plane is 40 μm and in the transverse plane about 5 mm.

The fast trigger chambers provide information to identify the specific bunch crossing a track belongs to and well defined p_{T} thresholds up to $|\eta| < 2.4$. They also measure the muon coordinate in the direction orthogonal to the one of the precision tracking chambers for a three dimensional combination. The resistive plate chambers consist of parallel electrode plates with a high voltage difference. A passing muon creates avalanches of secondary particles in the gas between the electrodes that induce an electronic signal. This technology is used in the barrel part up to $|\eta| < 1.05$. The end-cap regions of $1.05 < |\eta| < 2.7$ are populated with thin gap chambers. These are multiwire proportional chambers with a shorter distance between the electrodes than between the wires filled with a highly quenching gas mixture.

The standalone transverse momentum resolution of the muon system is designed to be $\sigma_{p_{\mathrm{T}}}/p_{\mathrm{T}} = 10\,\%$ for a muon momentum of $p_{\mathrm{T}} = 1\,\mathrm{TeV}$ and muons above $p_{\mathrm{T}} \approx 3\,\mathrm{GeV}$ can be measured in this mode. The muon tracks can also be matched to the tracks measured with the inner detector and have a momentum resolution of 1.7 % at $p_{\mathrm{T}} \approx 10\,\mathrm{GeV}$ and 4 % at $p_{\mathrm{T}} \approx 100\,\mathrm{GeV}$ [42]. To achieve this precision, the muon chambers are aligned using cosmic muons and an optical alignment system.

2.2.5 Luminosity Measurement

Beside the main detector components, the ATLAS experiment also has a number of smaller subsystems for dedicated measurements and triggering. Some of these are used in order to determine the luminosity delivered by the LHC. This quantity is of high importance to many measurements performed by the ATLAS collaboration and it is needed for the estimation of the cross-section of a physics process. For some analyses, the uncertainty on the luminosity determination is amongst the largest ones, hence a precise measurement of the luminosity is crucial.

Therefore, several independent detectors are used for the luminosity estimation of ATLAS. The most important ones for the dataset used in this thesis are the beam conditions monitor and the LUCID detector. They are located in the forward region of the ATLAS experiment which is why they have to be radiation hard. Both have a fast readout that allows to distinguish between the single bunch crossings. These detectors measure the particle flux in real-time to monitor the run conditions and can even trigger the dump of the beam if the conditions are harmful for the ATLAS detector.

LUCID consists of 2 modules, each containing 16 tubes that are filled with C_4F_{10} gas. The tubes are 1.5 m long, have a diameter of 15 mm and are arranged to enclose the beam axis. The detector is specialised in measuring inelastic proton-proton scattering in the forward region. A particle traversing the tubes stimulates Cherenkov light that is read out by photomultiplier tubes. The modules are located at $\pm$ 17 m from the interaction point which corresponds to $|\eta| \approx 5.8$.

The beam conditions monitor consists of tow sets made of four diamond sensors that are arranged around the beam pipe in a cross-pattern. Each sensor has a cross-section of about $1\,\mathrm{cm}^2$ which means that the acceptance of the detector is much smaller than the one of LUCID. The modules are located at a distance of $\pm$ 1.84 m from the interaction point at a radius of $R = 5.5\,\mathrm{cm}$ corresponding to $|\eta| \approx 4.2$. The detection principle is the same as for other semiconducting detectors and relies on ionisation. This way, the rate of incident particles is measured and the instantaneous luminosity can be deduced.

Both detectors only measure the relative luminosity and thus need to be calibrated. This is

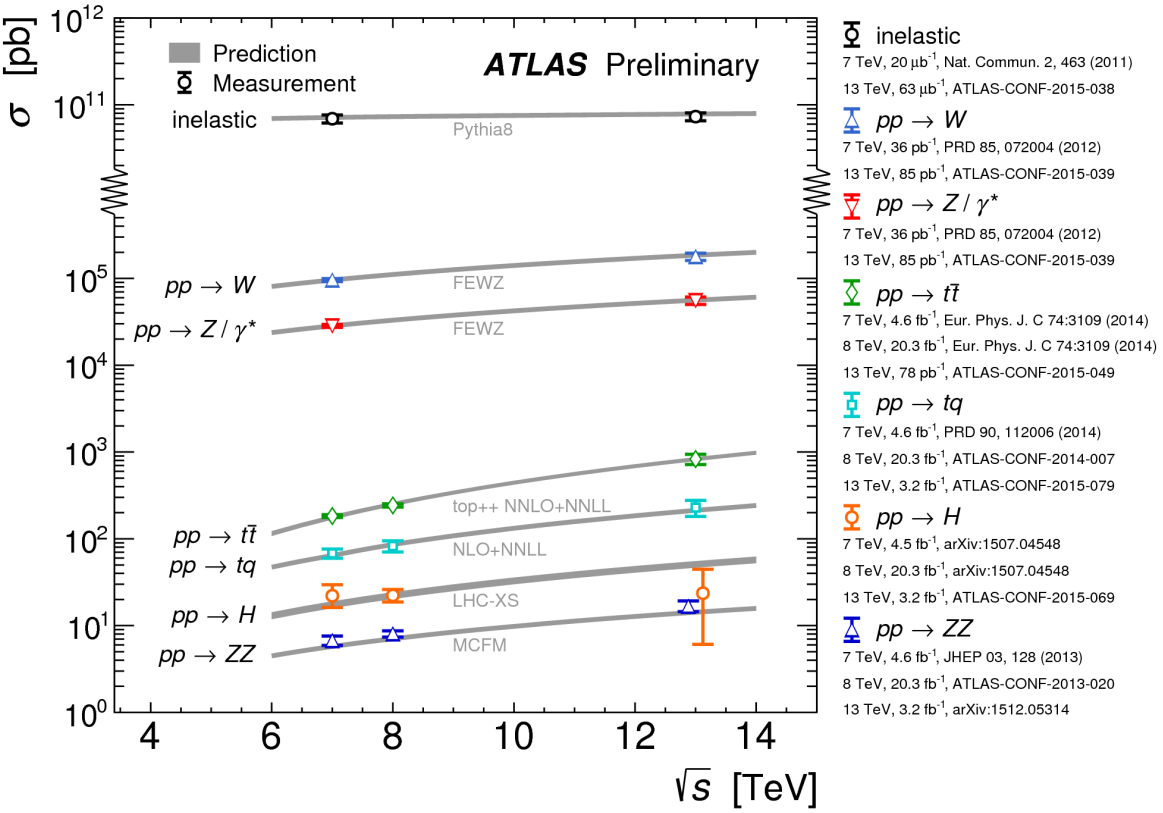

Figure 2.6: Summary of cross-section measurements performed by the ATLAS collaboration. A large difference in cross-section is visible between inelastic processes and boson production. It is of the order of 10^6 over the full range covered by the LHC [45].

done using dedicated LHC runs called Van der Meer scans [43]. During the course of these runs, beams with rather low intensity are scanned through each other in both x- and y- direction. This way the profile of the beam is obtained and is employed to compute the instantaneous luminosity. More details can be found in Reference [44]. Other components of the ATLAS detector are employed for cross-checks and the estimation of the systematic uncertainty of the luminosity estimation. For the data set studied in this work, this yields $\mathrm{L_{int.}} = (20.3 \pm 0.6)\,\mathrm{fb}^{-1}$.

2.2.6 The Trigger System

The high instantaneous luminosity at the LHC is beneficial for the production of processes with low cross-sections, like the generation of bosons which is shown in Figure 2.6 for the different centre of mass energies accessible at the LHC. Also indicated is the probability for inelastic collisions to occur, which is more than 6 orders of magnitudes higher than the boson production. Recording all these collisions is technically not possible, since the full detector information cannot be written to disc at the rate of the proton collisions, which is about 40 MHz. Therefore, an online event selection is crucial and additionally saves resources, since less events are stored. In ATLAS this event pre-selection is implemented as a levelled process where 3 consecutive triggering stages refine each others decisions. The systems are called Level-1, Level-2 and event filter. Where the first level is realised in custom built hardware and

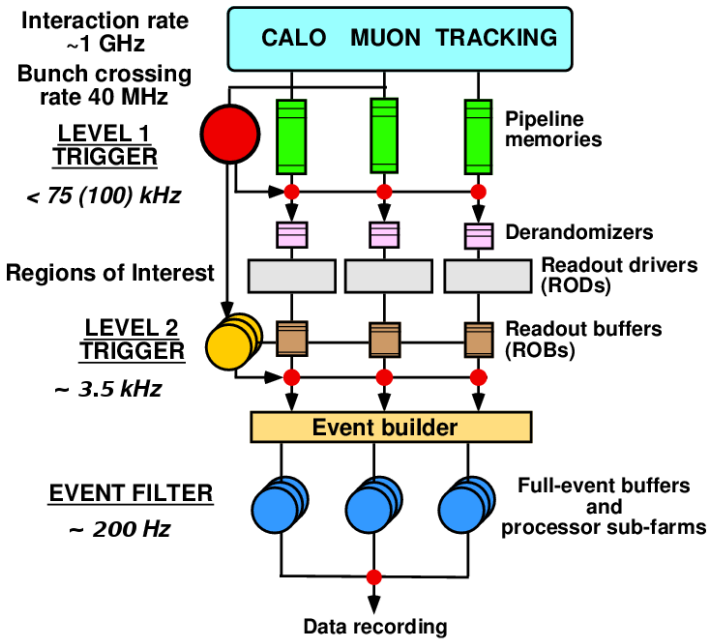

Figure 2.7: Block diagram of the trigger system of the ATLAS experiment. Indicated are the output rates the different triggers levels can provide as well as the different stages of data readout and storage. The figure is taken from Reference [46] and the trigger rates are updated to the design values from Reference [26].

the latter two are implemented using commercially available computer and network hardware. A block diagram of the system is shown in Figure 2.7 where also the path of the data governed by the data acquisition system is indicated.

The Level-1 trigger decision is based on a subset of the detector information. The design goal is to reduce the incoming rate to 75 kHz with a latency of 2.5 μs. This is done by selecting events containing objects that exceed certain transverse momenta thresholds or exhibit large total energy or missing transverse energy. For the muons, the muon trigger chambers are used. Electrons, photons, jets, hadronically decaying τ leptons as well as the energy sums are reconstructed using calorimeter information with a coarser granularity. The level-1 trigger decision based on the muon and calorimeter subsystems is performed by the central trigger processor that combines the different trigger objects to trigger items. Once an event is accepted on the first level, the detector information is read out and buffered. The central trigger processor also allows for the so-called pre-scaling of certain trigger items. This is the artificial reduction of a trigger item rate by discarding a certain fraction of triggered events, thus optimising the use of the available bandwidth.

The Level-2 trigger uses the full granularity of the detector in the regions where a high occupancy is indicated by the first trigger level. Within 40 ms each event is processed and evaluated, reducing the level-1 rate to 3.5 kHz. Events accepted by the second level of the ATLAS trigger are completely reconstructed using algorithms that are also used for the offline analysis. The event filter analyses these events reducing the output rate to 200 Hz on average with a latency of about 4 s per event. In practise, the system proofed to be even more powerful than its design and level-2 rates of up to 5 kHz were reached as well as a 400 Hz rate with the event filter. The events accepted by the full trigger chain are written out and have an

approximate size of 1.3 Mbyte. The data is processed in several steps afterwards where physics objects are reconstructed from the detector information as described in Chapter 4 and the data format is changed. These data sets are the ones studied by physics analysis like the one presented in this thesis.

3 Event Simulation

The Standard Model of particle physics yields precise predictions of the interaction of particles as described in Chapter 1. The theory can also be used to simulate the particle collisions using Monte Carlo methods. This is done by so-called event generators [47] and the detector is emulated using dedicated programs to describe the interactions of particles with matter. The ATLAS detector is simulated using the toolkit GEANT4 [48], details are given in Reference [49]. The output of this simulation are reconstructed using the same algorithms as used for the data recorded with the detector described in Chapter 4. Therefore, simulated events can be used to test the methods and prospects of a data analysis. But also the detector performance and acceptance can be evaluated by the use of simulated data. Furthermore, the interpretation of an analysis with respect to a certain physics model can be done using the predictions provided by simulation programs. Due to these and many more applications the simulation of particle collisions is an important ingredients for many particle physics measurements.

The simulation of particle collisions is a multi step procedure and is described in this chapter based on References [47] and [50]. Many event generator programs for these simulations exist. The ones of relevance for this thesis are outlined in Section 3.2. Section 3.3 gives a short overview of the event simulation for the ATLAS experiment.

3.1 Simulation of Proton-Proton Collisions

The collision of two protons is not a simple elastic scattering of two pointlike particles, but involves several processes: Protons have substructure and consist of quarks and gluons, also referred to as partons. The scattering of two incoming partons with high momentum transfer, the so-called hard process, is at the core of the simulation of particle collision. It can be described with good precision using perturbative Quantum Chromodynamics and electroweak theory. The remains of the beam do not participate in the hard interaction, but still carry a considerable amount of energy and are simulated as the so-called underlying event. Particles of the beam remnants can also interact with each other leading to another hard scattering which is referred to as multiple particle interaction. These basic building blocks of proton collisions are visualised in Figure 3.1. The particles leaving the collisions usually have a considerable momentum and tend to split into more particles during the so-called fragmentation process. Since only colour neutral particles can exist at large timescales, the outgoing particles form these states during the so-called hadronisation process. At all stages, unstable particles can decay producing secondary particles. The particles can emit electromagnetic and gluon bremsstrahlung which are referred to as initial or final state radiation depending on whether the radiating particle is incoming or outgoing of the hard process. Due to the high instantaneous luminosities at the LHC, multiple proton pairs can collide at the same time. This is called the pile-up of events and all the above considerations apply for all hard interactions that occur simultaneously. The interaction vertex with the highest transverse momentum is referred to as

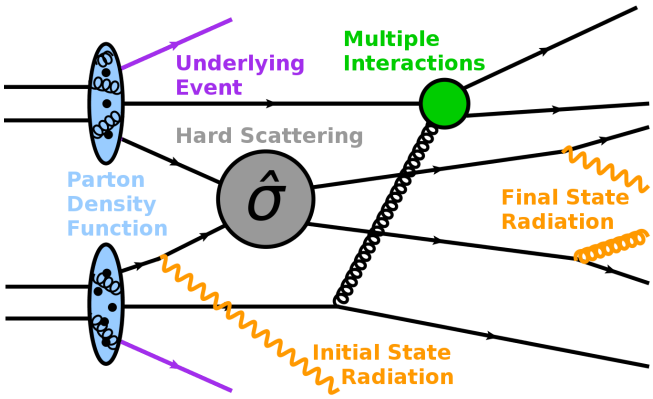

Figure 3.1: Feynman-style sketch of a proton-proton collision. Shown are the incoming protons with their substructure described by the parton density functions in blue, the hard scattering with the partonic cross-section $\hat{\sigma}$ in grey and an additional parton interaction with lower momentum transfer in green. Initial and final state radiation is drawn in orange and the underlying event is indicated in purple. Not shown are the factorisation and hadronisation of the particles, neither are pile-up events indicated.

the primary vertex of the event.

Monte Carlo generators allow to consider each of the above aspects separately. The production cross-section, $\sigma_{pp\to X}$, which is a measure of how likely it is to observe a certain final state X in a proton collision can furthermore be split into the hard scattering process and soft processes that are dominated by non-perturbative Quantum Chromodynamics effects. While the hard scattering can be computed from the matrix elements extracted from the Lagrangian of the theory, the soft contributions have to be evaluated using experimental data. According to the factorisation theorem, the production cross-section of a process X in proton-proton collisions can be written as the product of the partonic subprocess cross-section $\hat{\sigma}_X$ and the parton distribution function f_k of each of the incoming protons (referred to as a or b):

$$\sigma_{pp\to X} = \int dx_a dx_b f_a(x_a, Q^2) f_b(x_b, Q^2) \hat{\sigma}_X. \tag{3.1}$$

The parton distribution function is a measure of the probability that the parton k carries a fraction x of the proton momentum. Q^2 refers to the momentum scale of the hard scattering and the evolution of the parton density functions is governed by the DGLAP [51–53] equations. The variable x is a measure for the momentum fraction of the proton carried by the parton entering the collision and thus can obtain values between 0 and 1. The functional dependence between x and the parton distribution function can be studied for example in deep inelastic scattering processes. Several groups combine the experimental data to obtain the parton distribution functions. The ones used in this theses are CT10 [54] and CTEQ6 [55] from the CTEQ collaboration and the MSTW2008 [56] functions are used for cross-checks. The contribution from the parton distribution function is indicated in Figure 3.1 by the proton substructure in blue and $\hat{\sigma}$ is attributed to the parton collision with the highest momentum shown in grey.

Equation (3.1) can be explicitly written as an expansion in perturbation theory using the strong coupling constant, α_S:

$$\sigma_{pp\to X} = \int dx_a dx_b f_a(x_a, \mu_F^2) f_b(x_b, \mu_F^2) [\hat{\sigma}_0 + \alpha_S(\mu_R)\hat{\sigma}_1 + ...]_X, \tag{3.2}$$

where the index of $\hat{\sigma}$ indicates the order in perturbation theory. μ_F is called the factorisation scale and can be considered as being the scale separating long- and short-distance physics. The renormalisation scale, μ_R, refers to the scale at which the ultraviolet divergences of Quantum Chromodynamics are cancelled. The effect of these scales vanishes, if the cross-section is computed to all orders in perturbation theory, but usually only calculations for the first few orders are available. Therefore, the specific choice of the scales is relevant for cross-section predictions and will directly influence the numerical results. Typically the scales are chosen to be in the range of the momentum scale of the hard scattering process and μ_R and μ_F are set to be equal.

The parton distribution function is just one example of soft contributions to the proton scattering. In fact, only the hard scatter is computed using perturbation theory and all other components are simulated based on empirical models due to theoretical or computational restrictions. The Monte Carlo programs differ in the model they use for the simulation of the soft processes, but also in the specific hard process they can calculate.

3.2 Monte Carlo Generators

The predictions of quantum mechanics, the theory foundation of particles physics, are of a probabilistic nature. The event-by-event outcome of a reaction is unknown but a probability can be assigned to each possible outcome. Since the goal of Monte Carlo generators is to simulate single events, they employ random numbers in order to reproduce the quantum mechanical probabilities at various stages of the simulation process.

Monte Carlo programs differ in the order in perturbative Quantum Chromodynamics up to which they compute the matrix element of the hard scatter and in the different theoretical models they can describe. Also they have different implementations of phenomenological models of the soft part of the collision which are tuned to experimental data. During the parton showering one initial particle gives rise to many others with lower momentum due to bremsstrahlung. This could be described in perturbation theory, but due to the large multiplicity, the computation gets very extensive and models of angular- or p_{T}-ordered emissions of secondary particles are employed.

Special care has to be taken when combining the hard scatter and the parton shower in order to avoid double counting of particles and not to create any gap in the phase space. This is due to the fact that the hard scatter can not only describe a two-to-two particle scattering, but can have several particles in the final state. A real emission arising from the matrix element computation can also be emulated by the first splitting due to the parton shower but should only be simulated once. Therefore, several methods exist to combine the matrix element computation and the parton shower model. These methods can be distinguished by their order in perturbative Quantum Chromodynamics: for example the CKKW [57] or MLM [58] methods can be employed at leading order and the POWHEG [59] method for next to leading order matrix element calculations.

The showering in the initial state is modelled by a backwards evolution of the production process starting again from the hard scatter. The parton shower connects the energy scale of the hard process to the hadronisation scale, where colourless objects form, which is at the order of GeV. This step includes the decay of particles and the formation of hadrons involving so-called fragmentation models. They have to be employed, as the Quantum Chromodynamics becomes strongly interacting at these energy scales and the perturbative approach no longer holds.

Typical examples are the Lund string model [60] that simulates the long range confinement forces and the cluster-hadronisation model [61] that is based on the assumption of local parton-hadron duality [62].

The hadronisation process yields a large number of final state particles. Still, the overall energy flow is determined by the hard scattering and the hadronisation process can be viewed as a smearing of this scale [63]. The final step of the event generator is the embedding of the hard process in the context of underlying event, pile-up and multi-parton interactions.

There are many programs to calculate the hard scattering matrix elements for all different kind of theoretical models. While some of them are specialised in specific extensions of the Standard Model the so-called general-purpose generators usually implement the Standard Model and a limited number of extensions. Yet, they provide the showering of the particles, the decays and hadronisation as well as the underlying event and a description of pile-up. This functionality can also be interfaced with one of the specialised generators, which focus on the matrix element calculations, to simulate a full particle collision. The Monte Carlo generators used in this thesis are:

- SHERPA [62]: One of the general purpose generators. It computes the hard scattering at tree-level and includes a parton shower model to describe the emission of additional partons in the initial and final state. This is matched to the matrix element computation using the CKKW method [64–66]. The fragmentation is implemented using the cluster-hadronisation model. SHERPA also simulates the underlying event.

- Pythia [63, 67]: A general purpose Monte Carlo generator that can generate both the soft and the hard part of proton collisions. The matrix elements are evaluated at leading order and the Lund string model is used for the hadronisation of particles.

- MadGraph [68, 69] interfaced to Pythia: MadGraph is a matrix element generator that can generate the hard scattering of any theory formulated using the Lagrangian approach. For the event generation it is interfaced with Pythia.

- POWHEG [59, 70] interfaced to Pythia: POWHEG can compute the hard scattering at next-to leading order in Quantum Chromodynamics and implements a special matching scheme to the parton showering, called the POWHEG method. It is interfaced with Pythia for the full simulation of the collision.

- Alpgen [71] interfaced to HERWIG [72] and JIMMY [73] or Pythia: Alpgen is a generator to compute the hard scattering resulting in multi-parton final states. The matrix element calculations are in leading order in Quantum Chromodynamics and electroweak interactions. The output of the generator is at the parton level, which means that they have to be interfaced with a general purpose generator to describe the parton showering and hadronisation. The HERWIG generator is used to this end and employs an angular ordered showering. The multiple parton scattering is simulated using the JIMMY generator. Alternatively, Alpgen can also be interfaced to Pythia for the event generation.

- GG2WW [74] interfaced to HERWIG and JIMMY: GG2WW is a generator dedicated to simulate the loop induced gluon fusion to two W bosons: $gg \to WW \to l\nu l'\nu'$. The output is interfaced to HERWIG and JIMMY for the full event generation.

- VBFNLO [17–19]: The VBFNLO program is specialised in the computation of vector boson fusion as well as the production of two and three vector bosons in hadron collisions. The processes are computed at next-to leading order in Quantum Chromodynamics and the program is also able to simulate anomalous quartic gauge couplings in the framework of effective field theory (see Section 1.4). It can be interfaced to general purpose event generators, but in this thesis it is used for the computation of expectation values only. No event simulation with VBFNLO is used and the Version 2.7.1 is employed throughout this work.

For completeness, the simulated processes used in this thesis are given in Appendix A.3 along with the name of the Monte Carlo generator and the parton density function used to generate the events.

3.3 Event Simulation for the ATLAS Experiment

The simulation of collision events [49] in the ATLAS detector is realised using the software framework Athena [75] developed by the ATLAS collaboration. It integrates the event generation which is performed by a Monte Carlo generator (see Section 3.2) with the simulation of the detector implemented using GEANT4 [48]. The final step is the digitisation, the conversion of energy deposits in the active detector material to voltages and currents. The output format of this simulation is the same as the data read out from the detector, which means that the same reconstruction algorithms (described in Chapter 4) can be used. This fact ensures a good comparability between simulated and recorded events and also allows to estimate the efficiency of the reconstruction software. This is because for each simulated event the so-called truth record, the object information generated by the Monte Carlo program, is stored and can be compared to the information reconstructed using the detector emulation.

The digitisation step also includes the simulation of detector noise and the pile-up of events. The average number of pile-up interactions per bunch crossing, $\langle\mu\rangle$, is generated as discrete values. During data taking, this variable changes continuously, such that simulation and data disagree in this variable. This effect is corrected for by assigning weights to the simulated events such that the weighted distribution of $\langle\mu\rangle$ corresponds to the one in the data set used for the analysis. The distribution of the interaction vertices along the z-axis is also unknown before the actual data is recorded. To modify the generated distributions such that they agree with the one observed in data, again event weights are assigned to the Monte Carlo simulation.

The large scale production of Monte Carlo events is done using the LHC Computing Grid [76], a global network of interconnected computing centres providing computing resources for the LHC experiments. This way, about 1 million of events can be simulated per day [49].

4 Event Reconstruction with ATLAS

The physical quantities defining the final states of the particle collisions are computed during the reconstruction step of the data processing. To this end, the ATLAS software framework Athena [75] is employed to convert the energy deposits in the detector first to tracks and clusters and then to physical objects like photons, electrons and jets. Since the data format is identical for recorded and simulated events, the same algorithms can be used, preventing differences between data and simulation to arise due to the reconstruction step of the computation. Efficient algorithms are needed to fully reconstruct the final state particles and elaborate identification criteria are crucial to distinguish signal from background processes. This is especially crucial for the analysis of final states with a low production cross section, since the signal might not be observable if too many background events pass the selection criteria.

The reconstruction of the physics objects and observables used in this thesis is described in the following sections. The general description of the methods is based on Reference [77] but many performance studies have been published since it was released. Section 4.1 describes the reconstruction and selection of electromagnetic objects, followed by the description of muons. The reconstruction and calibration of jets is described in Section 4.3 and the definition of the missing transverse energy of an event is given in Section 4.4.

4.1 Electrons and Photons

The signature of electrons and photons in the detector is rather similar and their reconstruction is based on the same quantities: Tracks of the inner detector and energy clusters within the calorimeter. Therefore, special care is taken to distinguish the two types of objects during the reconstruction.

The tracks of the inner detector are reconstructed using global-χ^2 and Kalman-filter techniques as well as more specialised filters such as the Gaussian-sum filters. After the extraction of the spacepoints from the detector components, these methods are used to find track candidates starting from the innermost silicon layers and extending them throughout the whole of the tracking volume. Quality criteria, such as the number of spacepoints per track, are imposed to avoid the reconstruction of fake tracks caused by detector noise, malfunction or combinatorial effects. In a complementary approach of track finding, mostly tracks not originating from the primary vertex are recovered. This method extends track segments of the transition radiation tracker that are not matched by the inside-out approach into the inner volume of the detector. This way tracks from secondary vertices that stem from the decay of long lived particles can be reconstructed, as they might start outside the innermost detector layers. But also photons that produce an electron-positron pair when interacting with the detector material create these vertices. The neutral photon does not leave any trace in the tracking material, but after the conversion, the tracks of the electron and positron are visible in the detector. Due to asymmetric conversion or resolution effects, the tracks might appear

as one single track, but they are distinguishable from tracks of genuine electrons, since the latter originate from the primary interaction vertex. Therefore, the inner layer of the pixel detector is especially important for the discrimination of converted photons and electrons, but secondary vertices can be resolved up to radii of 800 mm [78].

The energy deposited by electrons or photons in the electromagnetic calorimeter is reconstructed as energy clusters. These consist of 15 energy towers, which are the transverse sums of energy deposited in all layers of the electromagnetic calorimeter with a granularity of $\Delta\eta \times \Delta\phi = 0.025 \times 0.025$. This corresponds to the granularity of the middle layer of the accordion calorimeter where most of the energy of electromagnetic objects is deposited. The energy of cells contributing to several towers is split uniformly. Clusters of the size 3×5 towers in η-ϕ with transverse energies exceeding 2.5 GeV are formed using a sliding window algorithm avoiding duplication [79].

In a consecutive step, the energy clusters are matched with the tracks from the inner detector which allows for the classification of the objects. Therefore, a hierarchy of the tracks is built depending on several criteria. These are for example, the distance between the track extended to the middle layer of the electromagnetic calorimeter and the centre of the energy cluster or the spacepoints associated to the track. But also the type of track, i.e. if it is identified as a photon conversion or as a prompt electron track, plays a role and precedence is given to converted tracks. All energy clusters that are not matched to a track or matched to a track with low p_{T} are categorised as unconverted photon candidates [80].

The energy clusters are recomputed and calibrated to the so-called electromagnetic energy scale, which corrects for energy losses and depositions of electromagnetic showers in the insensitive material. This is achieved using the decay of Z bosons to electron pairs, as the invariant mass of the Z resonance is known with a high precision [81]. Slightly different cluster sizes and corrections are employed for electrons, converted photons and unconverted photons, as they are subject to different losses. The decay of J/ψ hadrons to electrons and the radiative decay $Z \to ll\gamma$ are used to confirm the calibration. The uncertainty due to the energy scale varies with the transverse momentum of the object and its pseudorapidity. For low energetic electrons it amounts to 1.1 % and drops to 0.04 % for central electrons with $E_{\mathrm{T}} > 40$ GeV. For unconverted photons the uncertainty ranges from 0.2 % to 0.9 % and for converted photons it is below 0.4 %. The energy resolution has a relative uncertainty below 10 % for objects with $E_{\mathrm{T}} < 40$ GeV and decreases with increasing transverse energy.

The efficiency to reconstruct electrons is over 97 %, if the transverse momentum of the electron exceeds 15 GeV [82] and slightly decreases with increasing η. For photons with a transverse momentum above 20 GeV, the reconstruction efficiency is (97.82 ± 0.03) % [80].

4.1.1 Electron and Photon Identification

The identification of the electromagnetic objects is completed by imposing a set of requirements based on calorimetric variables and for the electrons additionally on track quality requirements. These criteria are needed in order to reject the reconstruction of electromagnetic objects coming from jets. Especially at hadron colliders jets are much more abundant than electromagnetic objects. For example, for transverse momenta between 20 and 50 GeV the production rate of jets exceeds the production of isolated electrons by five orders of magnitude [77]. Therefore, meaningful requirements have to be implemented to discriminate the objects.

Different sets of identification criteria are defined by the ATLAS collaboration and in this thesis the so-called tight criteria are used both for electrons and photons. This is done as

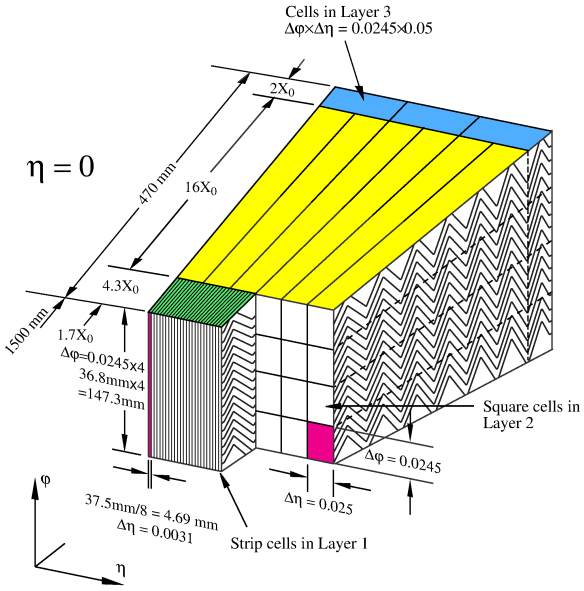

Figure 4.1: Layout of a barrel module of the liquid argon calorimeter. The strip, middle and back layer of the calorimeter are coloured in green, yellow and blue respectively. Their granularity in η-ϕ is indicated along with their depth. For better visibility of the dimensions, one cell of the strip and the middle layer is each coloured in pink. Modified from [26].

the signal requires a very high background rejection in order to become visible. The varying amount of material that is traversed by the particles in the different regions of the detector is taken into account by optimising the criteria in bins of $|\eta|$. For electrons, an additional dependence on E_{T} is found and incorporated in the identification requirements. The criteria are optimised independently for converted and unconverted photons.

The identification of electromagnetic objects is based on variables related to the different calorimeter regions described in Section 2.2.3 and depicted in Figure 4.1. The regions and the respective criteria are:

- Full calorimeter: A requirement is imposed on the ratio of the transverse energy deposited in the electromagnetic and the hadronic layers of the calorimeter. The energy in the hadronic calorimeter is summed in a window of 0.24×0.24 in η-ϕ around the centre of the electromagnetic cluster. For objects in the range $0.8 < |\eta| < 1.37$, the energy deposited in all layers of the hadronic calorimeter is considered, for all other electromagnetic objects, only the hadronic energy deposited in the first layer of the hadronic calorimeter is taken. This energy is divided by the transverse energy associated with the electromagnetic cluster and objects with high energy fractions in the hadronic calorimeter are rejected. This is done, since the showers of hadronic objects are much more extended, than electromagnetic showers.

- Middle layer of the electromagnetic calorimeter: The shape of the cluster in the middle layer of the electromagnetic calorimeter has to have a narrow lateral width and the energy ratios of energy clusters with a different number of cells in η- or ϕ-direction has to be close to one. This is because electromagnetic showers have a rather narrow energy profile concentrated at the core of the cluster in contrast to jets [83]. The lateral width in η is

computed using the Energy E_{C} deposited in a cell and its corresponding pseudorapidity η_{C}. The energy weighted sum over all cells C in a window of 3×5 cells in η-ϕ around the cluster position is computed according to:

$$w_2 = \sqrt{\frac{\sum(E_{\mathrm{C}} \times \eta_{\mathrm{C}}^2)}{\sum E_{\mathrm{C}}} - \left(\frac{\sum(E_{\mathrm{C}} \times \eta_{\mathrm{C}})}{\sum E_{\mathrm{C}}}\right)^2}$$

and a correction is applied to reduce the bias from the finite cell size [46]. The Energy ratios in pseudorapidity and in azimuthal angle are defined using the energy deposited in windows of different sizes in terms on middle layer cells in η-ϕ around the cluster centre:

$$R_\eta = \frac{E_{3\times7}}{E_{7\times7}} \text{ and } R_\phi = \frac{E_{3\times3}}{E_{3\times7}}.$$

- Strip layer of the electromagnetic calorimeter: The total shower width has to be narrow in η and the asymmetry E_{ratio} between the cells with the largest and second largest energy deposition in the cluster has to be small. The shower width is computed in a window of $\Delta\eta \times \Delta\phi = 0.0625 \times 0.2$ around the cluster centre. In the barrel, this window size corresponds to 20 strips. When i_{max} denotes the strip with the highest energy deposit and E_i is the energy deposited in strip i, the total shower width is defined as:

$$w_{\mathrm{stot}} = \sqrt{\frac{\sum_i E_i (i - i_{\mathrm{max}})^2}{\sum_i E_i}}$$

and i runs over all strips in the window.

For the definition of E_{ratio}, a window of $\Delta\eta \times \Delta\phi = 0.0625 \times 0.2$ around the cell with the highest energy deposit is considered and the strip $i_{\mathrm{max,\,2}}$ with the second highest energy deposition is determined. E_{ratio} can be written as:

$$E_{\mathrm{ratio}} = \frac{E_{i_{\mathrm{max}}} - E_{i_{\mathrm{max,\,2}}}}{E_{i_{\mathrm{max}}} + E_{i_{\mathrm{max,\,2}}}}. \tag{4.1}$$

Requirements on this variable rejects energy clusters from two sources that are merged in the middle layer, but can be resolved by the strip layer granularity.

Three additional criteria on the strip layer variables are introduced for photons, since the largest background for prompt photons arises from the decay of neutral pions to two photons. The granularity of the strip layer has a high efficiency in discriminating the two. The energy difference ΔE between the energy deposition associated with the second maximum in the cluster and the lowest energy deposition in a strip between the two maxima has to be small in order to reject clusters merged in the middle layer. When i_{min} denotes the strip with the lowest energy deposition located between the two maximal energy depositions $E_{i_{\mathrm{max}}}$ and $E_{i_{\mathrm{max,\,2}}}$ defined above, ΔE can be defined as:

$$\Delta E = E_{i_{\mathrm{max,\,2}}} - E_{i_{\mathrm{min}}}. \tag{4.2}$$

The rejection of clusters from two sources that are already merged in the strip layer is achieved by imposing requirements on the lateral shower width $w_{s\,3}$. This quantity is

defined similar to the total shower width, but it is computed using a smaller window size of three consecutive strips containing the strip with the highest energy deposition.

$$w_{s3} = \sqrt{\frac{\sum_{i=1}^{3} E_i (i - i_{\max})^2}{\sum_i E_i}}. \tag{4.3}$$

Also, the fraction F_{side} of the energy deposited in seven strips around the first maximum, excluding the three core strips, is required to be low.

$$F_{\text{side}} = \frac{E(\pm 3) - E(\pm 1)}{E(\pm 1)}, \tag{4.4}$$

here $E(\pm n)$ denotes the energy deposited in n strips around the strip $i_{\min}$.

- Back layer of the electromagnetic calorimeter: A requirement on the ratio of the cluster energy deposited in the last layer of the electromagnetic calorimeter and the total energy measured in this calorimeter is introduced for further background rejection.

$$f_3 = \frac{E_{\text{back layer}}}{E_{\text{cluster}}},$$

- Inner detector: Additional requirements on the quality of the tracks associated with the electromagnetic cluster are introduced for electrons. These include the number of spacepoints reconstructed in the different tracking detectors and criteria on the detected transition radiation. Also the position and energy matching criteria of the tracks to the electromagnetic clusters is refined for better background rejection.

Since the pion rejection of the photons strongly depends on the strip layer, photon candidates are rejected in the regions where this information cannot be relied upon. This is the region that is not sufficiently instrumented at $|\eta| > 2.37$. Also, photons in the region where the electromagnetic barrel and end caps overlap at $1.37 < |\eta| < 1.52$, are not used in this analysis, as a photon might not be fully contained in one of the components. Similarly, electrons in the region of the transition of the barrel and the end caps are excluded, but due to the less harsh criteria on the strip layer, they are limited in η by the acceptance of the inner detector and considered up to $|\eta| = 2.47$ in this thesis.

The efficiency to identify electrons with the criteria described above varies with the transverse energy and the η position of the electrons as well as with the number of vertices in the event. The first two distribution are shown in Figure 4.2 as expected from Monte Carlo simulation using the open markers and as measured in data using the full markers. The electrons used in this thesis employ the Tight criterion indicated by the square markers in the figures. Their identification efficiency is about 75 % on average [82], since a minimum electron p_{T} of 20 GeV is required.

Similarly, the efficiency for identifying photons is also not constant and depends on the type of the photon, i.e. converted or unconverted, in addition. A measurement of this efficiency is described in Reference [78] and an excerpt of the results is shown in Figure 4.3. The identification efficiency for unconverted (converted) photons is shown in the upper (lower) part of the figure as a function of E_{T} for two different regions in $|\eta|$. The measurement is shown by the round markers and the Monte Carlo expectation by the triangles. Slightly better efficiencies are observed for energetic photons than for electrons.

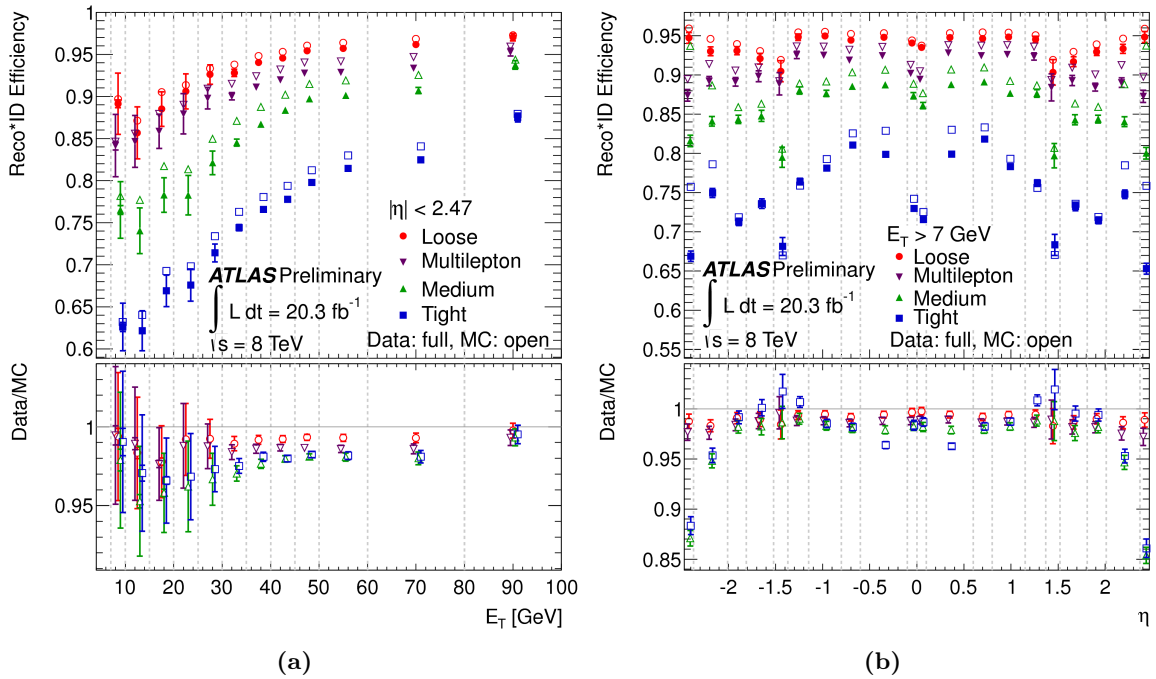

(a) (b)

Figure 4.2: Combined reconstruction and identification efficiency for electrons in dependence of the transverse energy (a) and of η (b). The values measured in data are shown in full markers and the expectations from Monte Carlo simulations is shown by the open markers. In this thesis the Tight criterion shown by the square markers is employed. The lower panel of each figure shows the ratio of the efficiencies measured in data divided by the Monte Carlo expectations [82].

4.1.2 Electron and Photon Isolation

The selection of objects passing all identification criteria for either electrons or photons still has a non negligible contribution from hadronic objects. They can further be discriminated from electromagnetic objects by using the transverse isolation energy, short isolation, of the object. It is defined as the transverse energy deposited in a cone around the object, excluding the object's energy itself. The choices of the radius of the cone offers a trade-off between robustness against pile-up and a better background rejection. For the objects used in this thesis, the size of the isolation cone is chosen to be $R = 0.4$.

Technically, the isolation is computed by summing all energy deposits in the electromagnetic and hadronic calorimeter within the defined cone, but excluding the contribution from the central electromagnetic cluster with a size of 5×7 cells in $\eta \times \phi$. This is indicated in Figure 4.4 where a sketch of the calorimeter cells in the η-ϕ-plane is shown along with the isolation cone. Energy deposits are indicated by filled squares. Since the whole electromagnetic shower of the object might not be contained in the central cluster, the leakage of the shower into the isolation cone is corrected for in dependence of the E_{T} of the object. Typically these corrections are of the order of a few per cent of the objects transverse energy [83]. After this correction, the isolation of prompt objects is nominally independent of the object's E_{T}.

The isolation energy is furthermore corrected for contributions of the underlying event and pile-up, to ensure comparability to theory predictions on parton level. The corrections are computed on an event by event basis as significant fluctuations are observable depending on

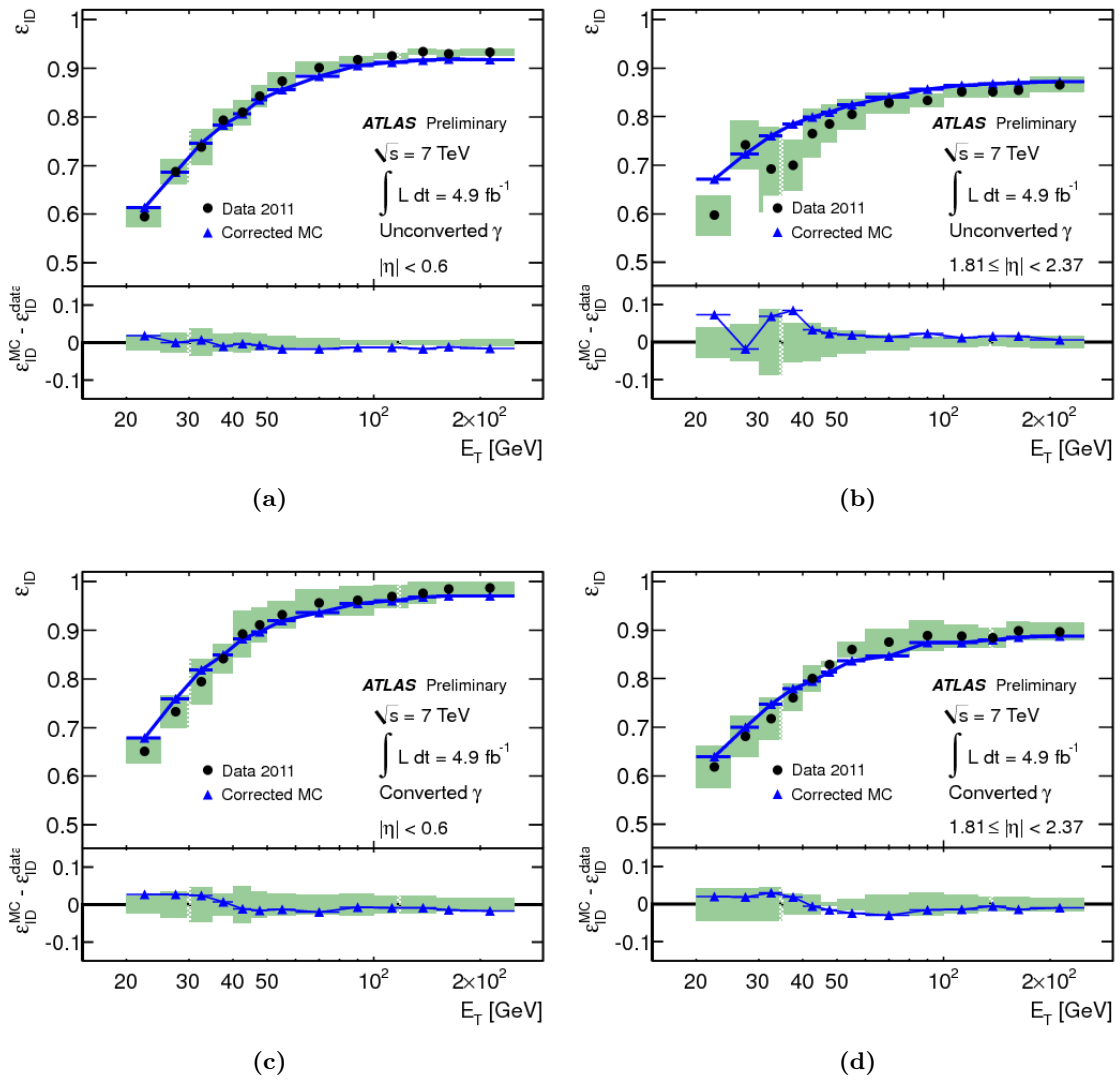

Figure 4.3: Identification efficiency for photons in dependence of the transverse energy measured in data (circular markers) and in simulation (triangles). The upper figures show the efficiency for unconverted photons in two different regions of $|\eta|$ and the lower ones show the same distributions for converted photons. The green error band indicates the combination of the statistical and systematic uncertainties of the data driven estimation of the efficiency. The lower panels in each figure show the difference between the observed efficiency and the expectations from simulation [78].

the number of hard interactions in the event. The correction is based on the median energy density of the jets in the event and subtracted from the isolation energy. Typical values of the correction are several hundred MeV [83]. After the corrections, the distribution of the isolation energy of prompt electromagnetic objects is centred around zero with a width of a few GeV. This also includes negative values of the isolation energy, which arise from the described corrections.

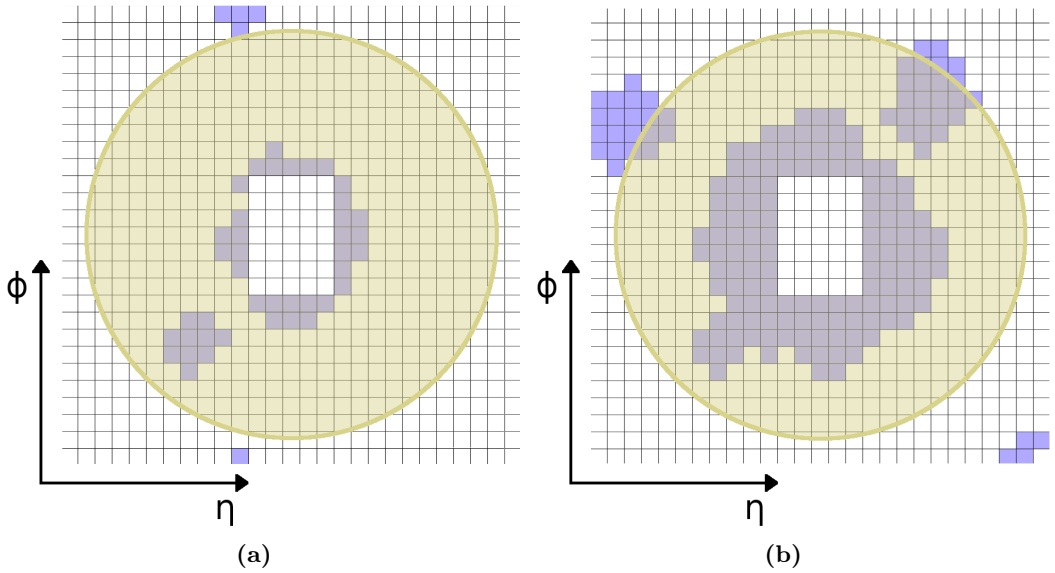

Figure 4.4: Sketch of the expected calorimeter isolation for an electromagnetic object (a) and a jet (b). The squares represent the calorimeter cells in the second layer of the electromagnetic calorimeter in the η-ϕ-plane and energy deposits are indicated by filled squares. The isolation cone is drawn in yellow and the inner 5×7 cells are drawn empty, as they are excluded from the computation. Additional energy deposits from the underlying event, pileup or detector noise are also indicated as they can distort the object's isolation.

4.1.3 Corrections to the Simulation of Electrons and Photons

The reconstructed objects from simulation and from the detector readout show small deviations due to mismodelling as can be seen in the lower panels of Figure 4.2. These are corrected for by assigning a weighting factor to each electromagnetic object and by incorporating these object weights to the total weight of the simulated events. The estimation of these weights for the reconstruction and identification of electrons is described in Reference [82]. It is based on the decay of J/ψ mesons and Z bosons to electron pairs and employs a so-called tag-and-probe method. The mismodelling of the data is found to be small with deviations of a few percent. The uncertainties of the event weights drop with increasing electron E_{T} from 1.5 % to 0.5 % The determination of the corrections applied to the simulated photons is described in Reference [78] and relies on radiative Z bosons decays ($Z \to ll\gamma$). The discrepancy is also assessed by extrapolating the photon shower shapes from electrons and by using a track based isolation to discriminate between photons and background objects. The results of the different methods are combined to compute the event weights. The uncertainties associated with these scale factors decrease with increasing photon E_{T} from a few percent to about 1 %.

Furthermore, the transverse momentum of the simulated objects is smeared such that the energy resolution in simulation agrees with the one measured using electron pairs from the Z resonance [81]. The relative uncertainty of this measurement increases with the transverse momentum of the objects up to 40 %, but is below 10 % for electrons and photons with $E_{\mathrm{T}} < 50\,\mathrm{GeV}$.

4.2 Muons

The reconstruction of muons relies on tracks detected in the muon system combined with the tracks of the inner detector [42]. Dedicated strategies to overcome the limitations in η of either detector part exist, but are not used in this thesis. Therefore, the acceptance of muons is restricted to $|\eta|$ <2.4 in the following discussion.

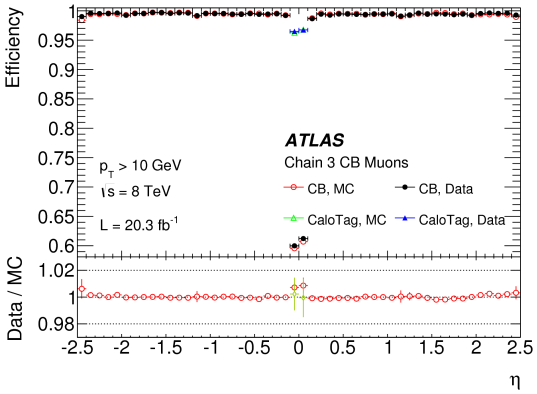

Figure 4.5: Reconstruction efficiency for muons as a function of η for different muon reconstruction types. In this thesis the combined muons are used and their efficiency is indicated with the open round markers for Monte Carlo simulation and with full round markers for the measurement using data. The bottom panel shows the agreement between data and simulation and the error bars correspond to the combination of the statistical and systematic uncertainties [42].

4.2.1 Muon Reconstruction and Identification

Tracks in the muon system are reconstructed by combining track segments of different muon chambers to full tracks spanning all layers of this subdetector. Independently the tracks in the inner detector are reconstructed as described in Section 4.1. For the identification of a muon, a track from the muon system and the inner detector have to be combined successfully. This is examined by the combination of two methods: either the two tracks have to satisfy the criteria of a statistical combination of the parameters of the two tracks, or the tracks are matched by a global refit of the full track by using the information of both detector subsystems. The extrapolation of the track accounts for multiple scattering and energy loss in the calorimeter. In this way, a reconstruction efficiency close to 99 % is reached for muons with a p_{T} larger than 10 GeV in most of the covered η-region as can be seen in Figure 4.5. The muons used in this thesis are indicated by the round markers. The open markers show the expected muon efficiency using simulation and the full markers correspond to the measured values. A drop in efficiency is observable around η values of zero, since the muon system is not fully equipped there to leave some room for service structures.

4.2.2 Muon Isolation

Prompt muons have a similar signature to muons being produced by the outgoing particles of the hard interactions, like the decay of hadrons, such as pions or kaons. Usually these hadrons are part of a jet and therefore accompanied by other particles. In contrast, the muon coming directly from the hard interaction is usually isolated. Therefore, a measure for the

isolation of muons can be introduced and utilised to discriminate prompt muons from hadronic backgrounds.

The track isolation is defined as the sum of the momenta of all tracks with a transverse momentum larger than 1 GeV in a cone with radius $R = 0.2$ around the muon track. The p_{T} of the muon track is excluded from the sum. A calorimeter based isolation criterion as introduced for electromagnetic objects (see Section 4.1.2) is conceivable, but not used, since the muon reconstruction is based on tracks. Also, the track based isolation is more robust to contributions from the underlying event and pile-up, when imposing the requirement that all tracks should come from the primary interaction vertex. In order to obtain a robust quantity over a large range of muon transverse momenta, in this thesis the relative track isolation $p_{\mathrm{T}}^{\mathrm{rel}}$ is used. It is obtained by dividing the track isolation of the muon by its transverse momentum.

4.2.3 Corrections to the Simulation of Muons

The differences of the momentum scale and resolution between simulated and recorded muons is corrected for in simulation. The correction is based on measurements using the decay of Z bosons, J/ψ and Υ hadrons to muon pairs [42]. The uncertainty of these corrections for the momentum scale are below 0.2 % and drop to 0.05 % for certain ranges of pseudorapidity. The muon energy resolution is studied and corrected individually for the inner detector (ID) and the muon system (MS). The associated uncertainties range between 3 % and 10 % depending on the transverse momentum and pseudorapidity of the muon.

The reconstruction efficiency of muons is studied with a tag-and-probe method again using muon pairs from resonances [42]. A good agreement between data and Monte Carlo is found, but still improved by applying small corrections to the simulation. The precision of the muon efficiency determination and thus the corrections is at the one permil level.

4.3 Jets

Jets arise from partons leaving the interaction or from the remnants of the protons. Therefore, they do not consist of a single particle only, but are composed of many constituents. Their measurement mostly relies on the calorimeter system of the ATLAS detector. To this end, the energy deposits in the calorimeters are summed to clusters from which the jets are reconstructed in a consecutive step.

4.3.1 Jet Reconstruction

The calorimeter clusters used in the reconstruction of jets are built from the energy deposits in all calorimeter layers. In contrast to the towers used for the electromagnetic objects, they do not necessarily include all cells in a certain transverse direction, which makes them more robust against noisy cells. The clusters are formed based on cells with a high signal-to-noise ratio: $\Gamma = {}^{E_{\mathrm{cell}}}/_{\sigma_{\mathrm{noise,\ cell}}} > 4$. The neighbouring cells in all directions are added to the cluster and their respective neighbouring cells are included, if their signal-to-noise ratio exceeds two. The cluster is extended until no adjacent cells with large energy deposits are found and in a final step all neighbouring cells of the formed cluster are included. The clusters formed in this way are split if they contain multiple maxima whose energy exceeds 500 MeV.

These clusters form the input for the reconstruction of the jets, also called jet finding [84]. This term refers to the grouping of the energy clusters to correspond to the spray of hadrons

produced during the fragmentation and hadronisation of partons. The jet finding has to fulfil a set of requirements in order to obtain a theoretically well defined object. For example, it must be insensitive to additional particles with low momenta, and robust against the collinear splitting of a particle. For the jets used in this work the sequential recombination algorithm anti-k_{T} [85] is employed which fulfils the aforementioned requirements. It can either have energy clusters or four-momentum vectors of final state particles from Monte Carlo simulation as inputs, which leads to a high degree of comparability between truth-level and reconstructed jets.

The anti-k_{T} algorithm proceeds as follows: For each input object i the distance d_{iB} between the input and the beam as well as the distances d_{ij} to all other inputs j are computed. They are defined according to:

$$d_{iB} = p_{\mathrm{T},i}^{-2} \text{ and}$$
$$d_{ij} = min(p_{\mathrm{T},i}^{-2}, p_{\mathrm{T},j}^{-2}) \frac{\Delta_{i,j}^2}{R^2},$$

where $\Delta_{i,j}^2 = (y_i - y_j)^2 + (\phi_i - \phi_j)^2$ and y is the rapidity defined as $y = 1/2 \ln[(E+p_z)/(E-p_z)]$. R refers to the radius of the jet and is chosen to be 0.4 in this thesis. The smallest of all distances is determined and in case the distance is of type d_{ij}, the inputs are merged by adding their four-vectors to form a new object k. The distances are recomputed with respect to the new input k and without the inputs i and j and the procedure is repeated. In case the distance is of type d_{iB}, the input i is considered as a jet and removed from the input list. These steps are repeated until all inputs are clustered to jet objects. In this way, generally jets with a circular shape in the η-ϕ plane are obtained and centred around the inputs with the highest p_{T} contribution.

The energy of the jets is computed from the energy of the underlying clusters. Since the energy of the calorimeter cells is calibrated to be at the electromagnetic scale, further corrections are needed to account for the lower detector response to hadrons, that are abundant in jets. This is done via a correction on cluster basis that depends on the location and the shape of the clusters. Corrections for energy losses due to not instrumented regions or threshold effects are applied and the jets are formed from these clusters. The jet objects themselves are calibrated in a consecutive step to account for noise, pile-up and algorithm effects. More details are given in Reference [86]. These corrections are sizeable and lead to relative uncertainties on the jet p_{T} that range from 1 to 6 % depending on the transverse momentum and the position in η of the jet. This can be seen in Figure 4.6, where the fractional uncertainty on the jet energy is shown as a function of p_{T} (a) and η (b). The methods to estimate these uncertainties rely on the momentum balance between a jet and another object like a boson or different jet, but also the response of the calorimeter to single hadrons in test-beam and collision data is used [87]. A residual correction is applied to Monte Carlo simulation in order to correct the observed deviation from the measurement. The measured resolution of the jet energy is found to agree with the simulation within its uncertainty of 10 % [88]. Therefore, no correction to the simulated energy resolution is applied.

Low momentum jets are likely to originate from pileup. Therefore, all jets that are reconstructed well within the tracking volume of $|\eta| < 2.4$ and have a transverse momentum below 50 GeV have to pass a requirement based on their vertex fraction [89]. This is a measure for the probability of the jet to originate from the primary interaction vertex. It is computed as the ratio of the sum of transverse momenta of tracks associated to the jet that originate

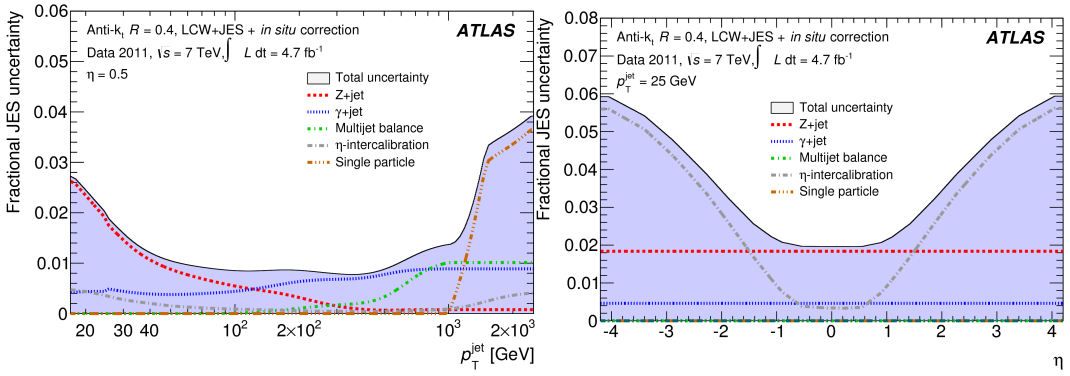

(a) **(b)**

Figure 4.6: Fractional systematic uncertainty on the jet energy scale in dependence of the jet p_T (a) and of the η of the jet (b). The other variable is respectively fixed to the indicated value. The contributions from different calibration methods are shown individually in colour [87].

from the primary vertex and the sum of p_T of all tracks associated with the jet and coming from any hard interaction vertex. This ratio must exceed 0.5, meaning that at least 50 % of the energy of the jet must be originating from primary vertex tracks in order to suppress jets from pileup while suppressing only a small amount of prompt jets. The potential mismodelling of the jet vertex fraction distribution of the simulation jets, is studied using events where a jet recoils against a Z boson and is on the percent level.

4.4 Missing Transverse Energy

The missing transverse energy, E_T^{miss}, is a measure of the momentum imbalance in the transverse plane of the collision. Since there is basically no momentum in the transverse direction prior to the particle interaction and all physics processes obey momentum conservation, the vectorial sum of energy deposits in the transverse plane of the detector should be zero. Yet, there are particles, like the neutrino, that do not interact with the detector but still carry energy. Therefore, their energy is observable as imbalance in the transverse plane. This way, neutrinos do leave a signature in the detector, even if they do not interact with it. Missing transverse energy can also arise due to detector effects like noise and energy resolution. As these distort the energy measurement, they can give rise to a momentum imbalance that is not caused by a physics object.

4.4.1 Missing Transverse Energy Reconstruction

The missing transverse energy is defined as the absolute value of the negative vector sum of the momenta of all particles detected in the collision. Its reconstruction is based on the full detector information and due to its large coverage, the calorimeter information plays an important part. Technically, the E_T^{miss} is determined by clustering the energy deposits in the calorimeter and matching them to physical objects. This is done in the order that at first all electrons are associated with their corresponding cluster, then the photons, the hadronically decaying τ leptons, the jets and finally the muons of the event. The electromagnetic objects are calibrated as for their regular reconstruction and the clusters associated with τ leptons are

calibrated to the hadronic scale as described in Section 4.3 for the jet clusters. For jets, the same algorithm and calibration described in Section 4.3 are used if their transverse momentum exceeds 20 GeV. Otherwise the cluster stays unmatched. All energy clusters not associated with any object are called soft terms. For each of the matched object categories the components of the missing transverse energy in x- and y-direction are computed according to:

$$E_x^{\text{miss}} = -\sum_{i=1}^{N_{\text{cluster}}} E_i \sin\theta_i \cos\phi_i \quad \text{and}$$

$$E_y^{\text{miss}} = -\sum_{i=1}^{N_{\text{cluster}}} E_i \sin\theta_i \sin\phi_i,$$

where the sum runs over all calibrated clusters in the respective category [90]. The missing transverse energy of the muon objects is computed as the negative vector sum of the momenta of the reconstructed muons. Calorimeter clusters associated with reconstructed muons are discarded to avoid double counting. The total transverse energy imbalance of the event in x-direction (y-direction) is obtained as the sum over the different object categories:

$$E_{x(y)}^{\text{miss}} = E_{x(y)}^{\text{miss},\,e} + E_{x(y)}^{\text{miss},\,\gamma} + E_{x(y)}^{\text{miss},\,\tau} + E_{x(y)}^{\text{miss,\,jet}} + E_{x(y)}^{\text{miss},\,\mu} + E_{x(y)}^{\text{miss,\,soft terms}}$$

and $E_{x(y)}^{\text{miss,\,soft terms}}$ refers to the energy depositions not associated with any object. This term can be obtained by using calorimeter information, but in this thesis its magnitude is determined using information from the inner detector: It is determined from tracks with a transverse momentum larger than 0.5 GeV that are not associated with any reconstructed object. This has the advantage, that it is robust against pile-up, as the precise position information from the tracks can be employed. Only tracks associated with the primary vertex are used and therefore contributions from multiple collisions or underlying event can be kept low. The disadvantage of this method is, that the contributions from neutral particles cannot be reconstructed, in the inner detector, such that their contribution to the soft terms is not accounted for. The uncertainties due to the energy scale and resolution of the soft terms can be assessed by studying leptonic W boson decay. This is done in Reference [90] for the calorimeter based soft terms and found to be of the order of a few percent.

4.4.2 Relative Missing Transverse Energy

The use of the full object reconstruction and calibration already suppresses the contributions to the missing transverse energy from detector effects or mismeasured objects by a large amount. Still, also a geometrical requirement can be imposed to further reduce the influence from mismeasurement. This is done by defining the relative missing transverse energy $E_{\text{T, rel}}^{\text{miss}}$. Therefore, the difference in azimuthal angle between the missing transverse energy and all final states objects is computed and the object closest to the $E_{\text{T}}^{\text{miss}}$ is determined. If this object is in the same hemisphere as the missing transverse energy, i.e. $|\Delta\phi| < \pi/2$, $E_{\text{T, rel}}^{\text{miss}}$ corresponds to the projection of the $E_{\text{T}}^{\text{miss}}$ on the axis perpendicular to the object. This is because in case the energy of an object is mismeasured, it will provide a component to the $E_{\text{T}}^{\text{miss}}$ along its axis. By projecting the missing transverse energy away from this axis, the contribution can be reduced. If there is no object in the same hemisphere, the original value of $E_{\text{T}}^{\text{miss}}$ is used:

$$E_{\text{T, rel}}^{\text{miss}} = \begin{cases} E_{\text{T}}^{\text{miss}} \times \sin(\Delta\phi), & \text{if } |\Delta\phi| < \pi/2 \\ E_{\text{T}}^{\text{miss}}, & \text{otherwise.} \end{cases}$$

By imposing requirements on this variable, events containing neutrinos, and thus genuine energy imbalance can be distinguished from events where all final state particles can be reconstructed, but $E_{\mathrm{T}}^{\mathrm{miss}}$ is present due to detector malfunction.

5 Selection of $WW\gamma$ Events

For the study of $WW\gamma$ events a data sample that is rich in this process and contains as little background as possible is needed. This is achieved by imposing selection criteria optimised to produce a sample with a high signal significance. The selection requirements include the proper functioning of the detector to avoid backgrounds from mismeasurement and several criteria on the final state objects and their kinematic variables to reject the background from events that have a similar topology as the signal. A good background rejection is crucial for the study of $WW\gamma$ events, as it is a rare process with a low cross-section. The production of other final states is several orders of magnitudes more likely, which is why even processes with objects in the final states that differ from the signal can contribute to the background, as these objects might be misidentified.

In this chapter, at first the $WW\gamma$ signal is defined and secondly the background processes are described. The data set used in this analysis is defined in Section 5.3 and the event selection criteria are described in Section 5.4. This is followed by a discussion of the stability of the selection as a function of time or pileup in Section 5.5.

5.1 Signal Definition

The production of $WW\gamma$ events has several signatures, as the W bosons can either decay leptonically into a lepton and the corresponding lepton neutrino or hadronically producing two jets. The study of either final state topology can yield the same physics message: a precise test of the Standard Model and its quartic gauge couplings. Still, the signature defines the analysis and the signal selection. For this analysis only $WW\gamma$ events decaying into light leptons are considered as signal. This has the advantage of less background due to jet production compared to the hadronic decay channel of the W boson, since no jet originates from the hard interaction. As jet events are abundant in hadron collisions, a good suppression of this background is valuable. An additional motivation for the study of the fully leptonic $WW\gamma$ final state is, that it has not been studied in proton collisions before and thus this study extends the test of the Standard Model of particle physics. The disadvantage of this signature is the low statistics, as the decay of W bosons to hadrons is more than twice [16] as likely as the decay into leptons.

The signature also comprises a photon which comes from the hard interaction. Therefore, it is expected to be more energetic than photons coming from initial or final state radiation and isolated. The electrical charge of the two W bosons is required to be opposite, as this corresponds to the signature of the quartic gauge boson interaction. Since it is mediated by either a Z boson or a photon which are both electrically neutral, the W bosons and thus the corresponding leptons in the final state need to have opposite electrical charge. Furthermore, a certain imbalance in transverse momentum is expected, as the leptonic decay of W bosons includes the production of a neutrino.

5.2 Background Processes

The iconic features of the $WW\gamma$ process described in the previous section can be used to define criteria to select $WW\gamma$ events, but other final states that have a similar signature exist. They have to be considered when determining the event selection criteria, since they are backgrounds to the $WW\gamma$ signal and should thus be rejected while keeping most of the signal events. The irreducible background processes to the $WW\gamma$ final states are:

Leptonic $Z\gamma$ events and Drell-Yan processes in association with a photon: Leptonically decaying Z bosons have the same signature as Drell-Yan processes, where a quark-antiquark annihilation leads to the creation of two leptons via a virtual photon or Z boson mediator. Therefore, they are discussed together in this analysis and also simulated as one background component. In principle, only lepton pairs with the same flavour and opposite electrical charge are produced, i.e. e^+e^-, $\mu^+\mu^-$ or $\tau^+\tau^-$, but also electron-muon pairs can be created through the consecutive decay of the τ leptons. The additional photon in the event yields a signature that is very similar to the one of the $WW\gamma$ events, and in the case of leptonically decaying τ pairs there is also an imbalance in the transverse energy observable due to the neutrinos in the final state. This process is labelled $\gamma^*/Z\gamma$ in the following discussion and constitutes the dominating background to the $WW\gamma$ signal.

WZ production: In case of fully leptonic decays of WZ events their final states contain three leptons. One of the leptons might not be reconstructed if it is outside the coverage of the detector in the forward region. Additionally, electrons that are reconstructed in the region of transition between the barrel of the electromagnetic calorimeter and the end caps are excluded from this analysis due to large reconstruction uncertainties. For muons the reconstruction efficiency is low for η values close to zero, because of the service structures of the detector. Thus, if a lepton is not reconstructed and the WZ event contains an additional photon, for example from radiation processes, it can mimic the signal. The failure to reconstruct a lepton in the detector is not very probable, but since the cross-section of WZ production is about three orders of magnitude [91] larger than the $WW\gamma$ production, this background is the second largest one.

The production cross-section of leptonic $WZ\gamma$ final states with a hard photon is about one order of magnitude lower than the one for the signal. This also includes the production via the quartic $WWZ\gamma$ vertex. Due to the fact that to mimic the signal one of the leptons must fail reconstruction, the direct production of $WZ\gamma$ events can be neglected as a background source.

Top pairs in association with a photon: Top quarks principally decay into a W boson and a quark [16]. In the case where both W bosons decay leptonically, the top quark pair production in association with a photon only differs from the signal signature by the presence of the two quarks that give rise to jets. The production cross-section of $t\bar{t}$ events is in the order of hundreds of picobarn [92], which is much larger than the probability to produce the signal and therefore their contribution to the background is non-negligible.

$WW\gamma$ final states containing τ leptons: τ leptons are not directly measured in ATLAS, but are reconstructed either from light leptons or as jets in case they decay hadronically. Therefore, the production of $WW\gamma$ events containing τ leptons is not considered to be

part of the signal, but part of the background. In case the τ decays leptonically, the same signature as the signal process is obtained. However, τ leptons are much more likely to decay hadronically [16] and thus only a small contribution from this process is expected.

Wt production: Single top quark production in association with a W boson can also mimic the signal if there is an additional photon from radiation in the event. The second W boson arises again from the decay of the top quark. Yet, the production probability of Wt events is about an order of magnitude lower than the probability for the production of top-antitop pairs due to the different production modes. Therefore, this process also contributes less to the $WW\gamma$ backgrounds than the top-antitop production.

ZZ production: The signature of ZZ events is also similar to the signal signature in case of leptonically decaying Z bosons. While one of the Z bosons creates the lepton pair, the other one can decay into two neutrinos and cause momentum imbalance. If the event contains an additional photon from radiation, the event looks like the signal in the detector. Again, it is the large production cross-section [91] compared to the signal that makes this background non-negligible.

Apart from the irreducible backgrounds, that are generally well modelled in simulation, there are also backgrounds that arise from the wrong identification of physical objects during the event reconstruction described in Chapter 4. Although this misidentification is rather rare, it needs to be taken into account in the study of rare processes, like the production of $WW\gamma$ events. As there are several orders of magnitude between the production probabilities of the respective processes even low misidentification rates can make significant contributions to the selected events. For this study the following faking mechanisms are of relevance:

Electrons misidentified as photons: Due to the similar signatures of photons and electrons in the detector, electrons can be mistakenly identified as photons. If an electron track is wrongly associated with a conversion vertex or even not reconstructed at all due to some inefficiency of the inner detector, the electron is reconstructed as a photon. For the $WW\gamma$ analysis this means that for example WZ events can mimic the signal, if they contain one of these fake photons from electrons.

Misidentified Jets: Due to the abundant jet production at the LHC, special care has to be taken in order to reconstruct jets only from hadronic clusters and not from electron, muon or photon objects. This is done using the identification criteria of the respective object, but due to fluctuations some hadronic jets might even fulfil these rather strict requirements. Therefore, if the jet is misidentified as a photon, the production of Z bosons, WW or $t\bar{t}$ events in association with jets can contribute to the background of the $WW\gamma$ signal. If the jet fulfils the selection criteria of electrons, $W(\rightarrow \mu\nu)\gamma$ events containing jets can mimic the signal. In the case where the jet is misidentified as a muon, $W(\rightarrow e\nu)\gamma$ in association with jets can fulfil the signal requirements.

All these backgrounds have to be considered when defining the signal selection criteria in order to obtain a sample with an acceptable signal purity.

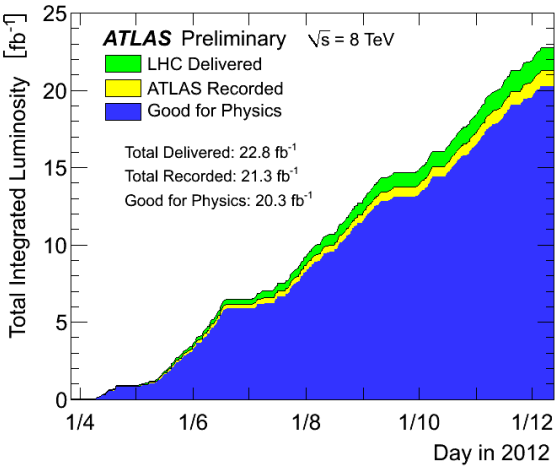

Figure 5.1: Total integrated luminosity of the data set used in this thesis as a function of time. The luminosity delivered by the LHC is shown in green and the fraction of the luminosity that was recorded with the ATLAS detector in yellow. The data used in the analysis are indicated by the blue histogram. They exclude time windows where only parts of the detector were functioning properly [93].

5.3 Data Set and Quality Selection

The proton-proton collisions recorded with the ATLAS detector in the year 2012 are studied in this analysis, as this corresponds to the data set with the largest statistics obtained to date. A sample with high statistics is needed in order to study rare processes such as the $WW\gamma$ final state.

The LHC delivered a total of $22.8\,\text{fb}^{-1}$ of proton-proton collisions to the ATLAS detector which recorded $21.3\,\text{fb}^{-1}$ of data [44]. The difference between delivered and recorded data comes from the inefficiency of the data acquisition system and the time the detector needs to be in full operational mode after the LHC declared the beam conditions to be stable. Following the recording, the operational status of each subdetector is carefully checked and only when all major subsystems are functioning, the data is used for the physics analysis in order to prevent backgrounds due to unwanted behaviour of some detector component. The evaluation of the run conditions is done with the approximate accuracy of one minute in order to balance data loss and bookkeeping efforts. The integrated luminosity of the data fulfilling all requirements is $20.3\,\text{fb}^{-1}$ and depicted in Figure 5.1 as a function of time. Some detector defects are furthermore excluded on an event-by-event basis. These include events that contain noise bursts in the liquid argon calorimeter or misbehaving cells in the tile calorimeter. But also events containing corrupted data or where some information is missing after one of the detector component's readout saturated are discarded.

5.4 Event Selection

The criteria to discriminate the signal from background processes are based on the expected topology of the $WW\gamma$ events. In case both W bosons decay into light leptons of the same flavour, the only difference between these final states and the $\gamma^*/Z\gamma$ background is the transverse energy imbalance and the shape of the distribution of the invariant mass of the

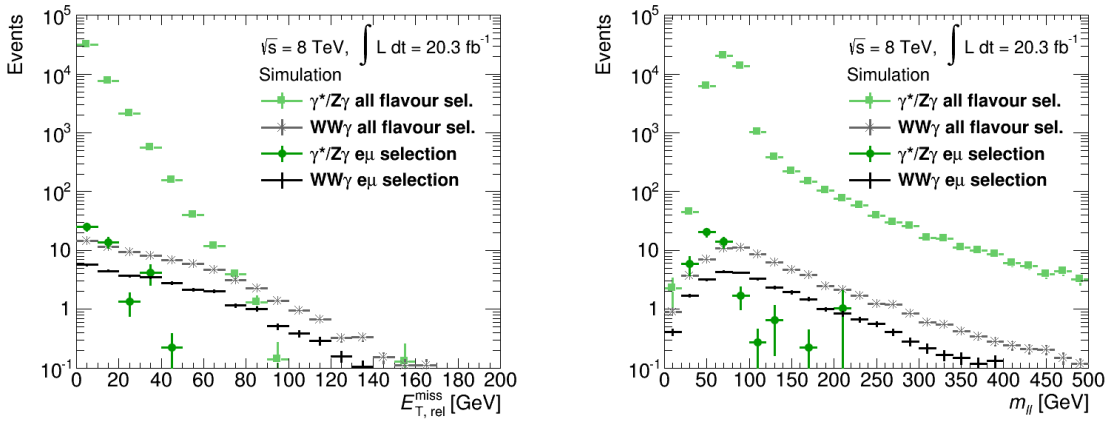

(a) **(b)**

Figure 5.2: Expected number of signal and $\gamma^*/Z\gamma$ events in dependence of $E^{\text{miss}}_{\text{T, rel}}$ (a) and of m_{ll} (b) for fully leptonic $WW\gamma$ events. Two different sets of selections are shown: "all flavour selection" refers to final states containing any combination of electrons and muons and is shown in the lighter set of colours. The $\gamma^*/Z\gamma$ events (square markers) dominate this selection over the $WW\gamma$ signal (star markers). The "$e\mu$ selection" shows the number of expected events when only light leptons with different flavour are selected. Again $\gamma^*/Z\gamma$ events (round markers) and $WW\gamma$ signal processes (crosses) are shown. The events shown correspond to an integrated luminosity of 20.3 fb^{-1}.

dilepton system, m_{ll}. The expected distribution of both variables is shown after a basic object selection in Figure 5.2. The distributions labelled "all flavour selection" depict the expected number of events in 20.3 fb^{-1} of data when all combinations of light leptons are allowed in the final state. The $\gamma^*/Z\gamma$ background depicted in green is dominating the signal and only at values of $E^{\text{miss}}_{\text{T, rel}}$ around 70 GeV are their contributions comparable. The m_{ll} distribution of the $\gamma^*/Z\gamma$ shows a peak at around 70 GeV which arises due to the transverse momentum requirements imposed on the lepton pair and because the events have only been simulated with a lower threshold of $m_{ll} = 40$ GeV. Therefore even more events with low values of m_{ll} are expected, but not included in the simulation shown here. Still, the conclusion is the same as for the $E^{\text{miss}}_{\text{T, rel}}$-distribution: the $\gamma^*/Z\gamma$ background completely dominates the signal and background rejection criteria based on either observable introduce a high loss of signal events.

The ratio of signal to background events is better for final states that only contain light leptons of different flavour, i.e. one electron and a muon. They are also depicted in Figure 5.2 using the darker set of colours. With this selection the contribution of $\gamma^*/Z\gamma$ events comes from final states with leptonically decaying τ leptons. This way the phase space of the background is largely reduced and the number of signal and background events is comparable. When applying the different flavour criterion, the number of signal events is only suppressed by a factor of two which comes from the combinatorics of the final state. Therefore, the event selection in this thesis is based on the different flavour channel only, resulting in the study of $e\nu\mu\nu\gamma$ final states, referred to as $e\mu\gamma$ in the following discussion. Including the same flavour channels is possible, but would require harsh background suppression cuts to obtain a sample with a reasonable purity.

A sample enriched in $e\mu\gamma$ final states is obtained using the selection criteria detailed in the following sections. These event selection criteria are applied to the recorded data and to Monte Carlo simulations in order to obtain meaningful expectations.

Trigger The trigger item used for the recording of $e\mu\gamma$ final states needs to consider every event, i.e. run without pre-scales, as the process is very rare and therefore a loss of even a small fraction of events would limit the feasibility of this analysis. To this end, the number of events to be recorded is restricted using kinematic observables of the event in order to cope with the bandwidth limitation of the detector readout. Since the distribution of the transverse momentum of the final state objects is steeply falling with increasing p_{T}, one of the options to restrict the number of events to be recorded is by requiring a minimal transverse momentum. Another option is to impose criteria on the object multiplicity in the event. This is beneficial for analyses of final states containing several object as for example the one presented here. A dedicated trigger object for triboson analyses was implemented in 2012: a trigger that selects events containing one muon with at least 18 GeV of transverse momentum and two electromagnetic objects each carrying at least 10 GeV. This trigger imposes less harsh criteria on the objects' transverse momenta compared to the single object triggers that recorded data without pre-scales in 2012, as it has a lower rate due to the higher multiplicity required. Therefore, it is better suited for this analysis, as the requirements on the objects' transverse momenta do not contribute to the rejection of backgrounds at this scales, but are simply imposed due to technical reasons. Events that fulfil the requirements of this trigger, called `EF_mu18_2g10_medium` are studied in this analysis.

Event Quality The events used in this analysis have to fulfil a set of basic quality criteria to ensure that a proton collision took place and that the missing transverse energy can be computed correctly. In order to achieve the first goal, events are only considered for analysis, if they contain at least one reconstructed vertex with at least three associated tracks that have a transverse momentum exceeding 500 MeV. For the measurement of the missing transverse energy it is important, to assign the correct energy to each of the objects. Events are therefore discarded, when they contain jets that are likely to be mismeasured. This can happen due to cosmic particles in the detector, bad LHC beam conditions or misbehaviour of parts of the detector. These jets have a slightly distorted shape in the calorimeter and a set of requirements to discard them is defined based on calorimetric variables. Events containing jets that fail the calorimeter criteria are rejected, if their p_{T} exceeds 20 GeV, since this might distort the energy imbalance too much.

Object Selection Events of interest for this analysis contain an electron, a muon and a photon. Therefore, the event selection criteria require these objects to be reconstructed in the detector according to the procedure described in Chapter 4. After the reconstruction, objects of different types can overlap, meaning that their coordinates are very close together and they probably originate from the same source. For the electrons and photons this overlap is already resolved during the reconstruction step, but jets, for example, are reconstructed from all energy depositions in the calorimeter and therefore have to be discarded if the energy is also associated to an electron or a photon, to avoid double counting. To this end, electrons that are closer than $\Delta R = 0.1$ to a reconstructed muon or to an electron with a higher transverse momentum are discarded. Photons are rejected, if they are closer than $\Delta R = 0.5$ to any remaining electron or muon. Jets are discarded, if they lie within a cone of $\Delta R = 0.3$ of an electron or within a cone of $\Delta R = 0.5$ of a photon. Muons are discarded, if they overlap with any remaining jet with a transverse momentum larger than 25 GeV in a cone of $\Delta R = 0.3$. This rejects mainly muons that are produced during the fragmentation and hadronisation

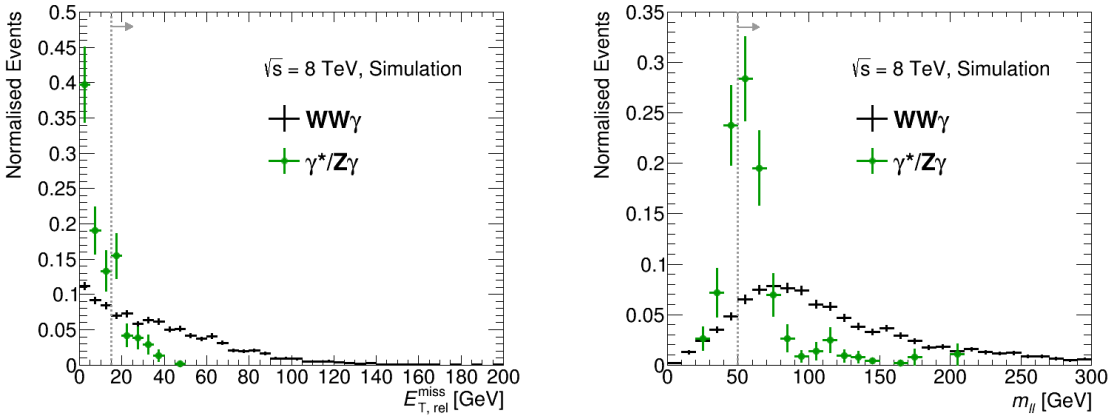

(a) **(b)**

Figure 5.3: Expectations of signal and $\gamma^*/Z\gamma$ events in dependence of $E_{\mathrm{T,rel}}^{\mathrm{miss}}$ (a) and of m_{ll} (b) for $e\mu\gamma$ final states after a basic event selection. The area of the distribution is normalised to one for easier comparison of the shapes of the distributions. The dashed line indicates the chosen threshold value and the arrow indicates the events that are accepted by the respective selection.

process and helps reducing the background where jets are misidentified as muons.

Due to the trigger item used, the transverse momentum of the leptons is required to exceed 20 GeV and the photon p_{T} needs to be larger than 15 GeV, to select events where the trigger is fully efficient. If any other lepton with a transverse momentum larger than 7 GeV is reconstructed, the event is discarded, as this is not expected to be present in the signal process.

The electrical charge of the leptons has to be opposite as the mediator of the quartic gauge coupling is electrically neutral. Therefore, lepton pairs with the same charge originate from background processes and hence these events are discarded.

Background Suppression Apart from the selection criteria that define well measured $e\mu\gamma$ events, further requirements are imposed in order to reject specific background processes. Although these criteria discard parts of the signal events, they are employed, as they improve the purity of the selected data sample.

The $\gamma^*/Z\gamma$ background can be distinguished from the signal by the relative frequency of events that have small values of $E_{\mathrm{T,rel}}^{\mathrm{miss}}$. This can be seen in Figure 5.3a where the distribution of signal and background events normalised to unit area is shown after the object selection described above. To suppress the background events at low values of $E_{\mathrm{T,rel}}^{\mathrm{miss}}$, a lower threshold of 15 GeV is introduced. This requirement also suppresses jet production events. These typically contain two or more jets and no prompt leptons, i.e. no source of missing transverse energy. Therefore, they are also discarded by the minimum $E_{\mathrm{T,rel}}^{\mathrm{miss}}$ threshold.

Another variable that discriminates the signal from the $\gamma^*/Z\gamma$ background is the invariant dilepton mass. Its normalised distribution is shown in Figure 5.3b for the signal in black and for the background in green. Again, the Monte Carlo simulation has a minimum requirement of $m_{ll} > 40$ GeV applied, which is why the lower bins are not populated by the background. Still it is observable that a lower threshold on m_{ll} only discards a minor fraction of the signal while rejecting a substantial amount of $\gamma^*/Z\gamma$ background events. Therefore, this threshold is chosen to be 50 GeV in this analysis.

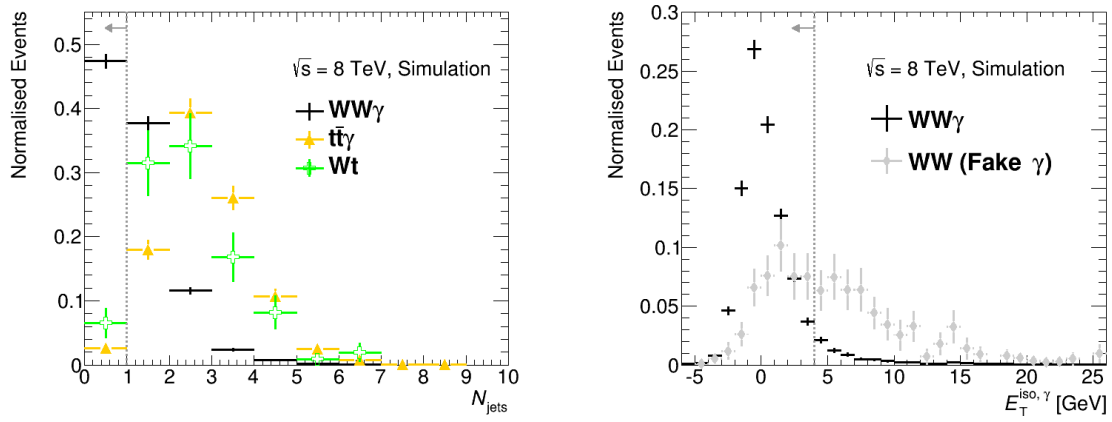

Figure 5.4: Expectations of signal and background events in dependence of N_{jet} (a) and of $E_{\text{T}}^{\text{iso},\gamma}$ (b) for $e\mu\gamma$ final states after a basic event selection. The signal is shown in black and the different background sources are shown in colours. The events labelled "WW (Fake γ)" show simulated WW where the photon is not present in the truth record of the hard interaction, but comes from a falsely identified jet. The area of the distribution is normalised to one for easier comparison of the shapes of the distributions. The upper threshold value chosen for the event selection is indicated by the dashed line and the arrow shows the events that are accepted by the respective requirement.

Another source that is largely contributing to the background is the production of top quarks. The $e\mu\gamma$ final states produced by these processes contain additional jets which can be used to distinguish them from the $WW\gamma$ signal. This can be seen in Figure 5.4a, where the normalised distributions of $WW\gamma$, $t\bar{t}\gamma$ and Wt production are shown after the object selection. While the signal distribution peaks in the bin containing no jets, the simulated top quark events have very few events where no jet is reconstructed. Therefore, only events with no reconstructed jets are analysed in this thesis to reject the top backgrounds. The fraction of top quark events without reconstructed jets arises, as the jets might lie outside of the detector coverage of $|\eta| < 4.5$. Furthermore, the transverse momentum threshold for the reconstruction of jets is chosen to be $p_{\text{T}} = 25\,\text{GeV}$ and some of the jet momenta lie below this value and are therefore not reconstructed.

In order to discriminate prompt objects from the hard interaction against misreconstructed jets, requirements on the objects' isolation are introduced. Electrons and photons are showering electromagnetically in the detector while the energy loss of jets is mainly due to nuclear interactions. The electromagnetic showers are much more contained than the hadronic ones and therefore the isolation energy of the objects is lower. This is as an example shown for photons in Figure 5.4b. The normalised $E_{\text{T}}^{\text{iso},\gamma}$ of the photon with the highest p_{T} in $WW\gamma$ and WW events is shown after the object selection. The photons from the WW sample are only accepted, if they cannot be associated with a photon from the truth record of the event generation, but with a hadron. Therefore, the distribution labelled "WW (Fake γ)" shows the expected distribution of $E_{\text{T}}^{\text{iso},\gamma}$ for jets mistakenly identified as photons. While the signal shows the expected peak around $E_{\text{T}}^{\text{iso},\gamma} = 0\,\text{GeV}$, the background distribution is much wider and shifted towards larger values of $E_{\text{T}}^{\text{iso},\gamma}$. Therefore, an upper limit of $E_{\text{T}}^{\text{iso},\gamma} = 4\,\text{GeV}$ is introduced in order to discard background events. The situation is very similar for electrons

and accordingly the requirement $E_{\mathrm{T}}^{\mathrm{iso,\,e}} = 4\,\mathrm{GeV}$ is employed. Muons typically only deposit a very low fraction of energy in the calorimeter. Their isolation criterion is based on the momentum of their tracks as described in Section 4.2.2 and chosen to be: $p_{\mathrm{T}}^{\mathrm{iso}}/p_{\mathrm{T}} > 0.1$.

5.5 Selection Stability

The event selection criteria select a very specific region in phase space that is enriched in $e\mu\gamma$ final states coming from $WW\gamma$ events. In the full data set of $20.3\,\mathrm{fb}^{-1}$, 26 events fulfil all the requirements and a visualisation of one of them is shown in Figure 1. In order to check that the selection does not enhance a certain point in time in data taking and thus the events might originate from special run conditions or detector effects, the event yield per data taking period is shown in Figure 5.5a. A data taking period corresponds to a certain time interval, typically a few weeks, in which the detector conditions are not expected to change. Usually the periods correspond to the time span between two openings of the detector cavern for repairs. Ten of these periods are used for this analysis and have integrated luminosities between 0.8 and $5.1\,\mathrm{fb}^{-1}$. Figure 5.5a shows the event yield of the selection normalised to one femtobarn per run period. Due to the low statistics, no events of periods A, G and H are selected, which is why the corresponding bins are empty. The bin entries are fitted the constant value of $(1.2 \pm 0.2)\,\mathrm{Events}\,/\,\mathrm{fb}^{-1}$ indicated by the line in the figure. The agreement of the data and the hypothesis of a constant selection efficiency can be evaluated using a so-called χ^2-test, that quantifies the deviation of the fit and the data. The values of χ^2 divided by the degrees of freedom of the distribution should be small for the fit to describe the data. The fit shown in Figure 5.5a corresponds to $\chi^2/NDF = 6.4/6.0$ indicating good agreement. The selection stability is also checked as a function of the average number of interactions, which is an indicator for the pileup in the event, as shown in Figure 5.5b. Here the event yield is normalised to the event yield per $\langle\mu\rangle$ before the event selection is applied and again the fit to a constant value is shown in the figure. The χ^2-test yields $\chi^2/NDF = 5.9/10.0$ confirming a selection efficiency independent of $\langle\mu\rangle$.

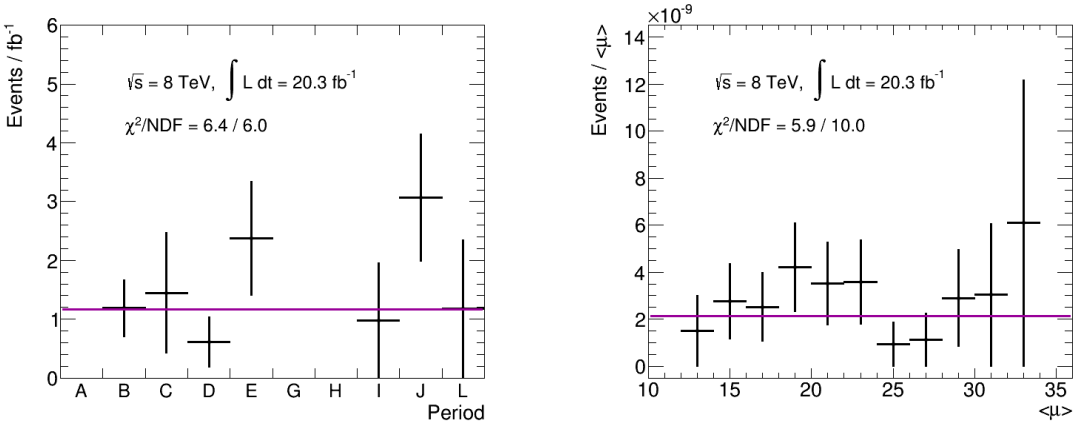

(a) **(b)**

Figure 5.5: Selection stability of $e\mu\gamma$ final states in dependence of the data taking period (a) and as a function of the average number of interactions (b). The straight line fit is shown along with its value of χ^2/NDF.

6 Signal Extraction

The data sample selected using the criteria introduced in the preceding chapter does not only contain signal events, but has non-negligible contributions from various background processes. For the extraction of the number of signal events, the event count of each background component is estimated. The irreducible background from physics processes with similar final states as the $WW\gamma$ signal in $e\mu\gamma$ final states, is computed using Monte Carlo simulation. This is feasible as the cross-sections of these processes are well measured and the description in simulation is good. Backgrounds that arise due to detector effects are less well-modelled by simulation. Therefore, they are estimated using methods that employ recorded data. This analysis is subject to two different sources of backgrounds from fake objects: misidentified electrons and misidentified jets. In this chapter, first the estimation of the irreducible backgrounds and their uncertainties is described in Section 6.1. Section 6.2 outlines the method used to evaluate the contribution of electrons that are misidentified as photons. Jets misidentified as one of the final state objects are described in Section 6.3 along with the ABCD method to estimate their contribution. The computation of the most likely value for the number of signal events is presented in Section 6.4 where the estimation of all backgrounds to this analysis is combined.

6.1 Backgrounds from Irreducible Processes

All irreducible processes that contribute to the background of the $e\mu\gamma$ signal were measured with the ATLAS detector as highlighted in Figure 6.1. Good agreement between the measurements and the theory predictions (indicated in grey) is observed for all processes in question. This justifies the use of Monte Carlo simulation for their estimation, as they are well understood. This analysis uses three different Monte Carlo generators for the estimation of the irreducible backgrounds, which are:

- SHERPA, that computes the cross-sections at leading order. It is used for the simulation of $\gamma^*/Z\gamma$, WZ and ZZ events with up to three additional partons in the final state. The SHERPA generator is also used for the computation of the signal sample and the background component from $WW\gamma$ events containing τ leptons. To this end, up to one additional parton is simulated in the final state.

- MadGraph is used to simulate top pair production in association with a photon. The cross-section is computed at leading-order and the Pythia generator is employed for the showering and hadronisation.

- POWHEG interfaced with Pythia is used to generate Wt events. This yields cross-section expectations at next-to-leading order.

More details on the sample statistics, the computed cross-sections and on the parton density functions used in the simulation can be found in Appendix A.3.

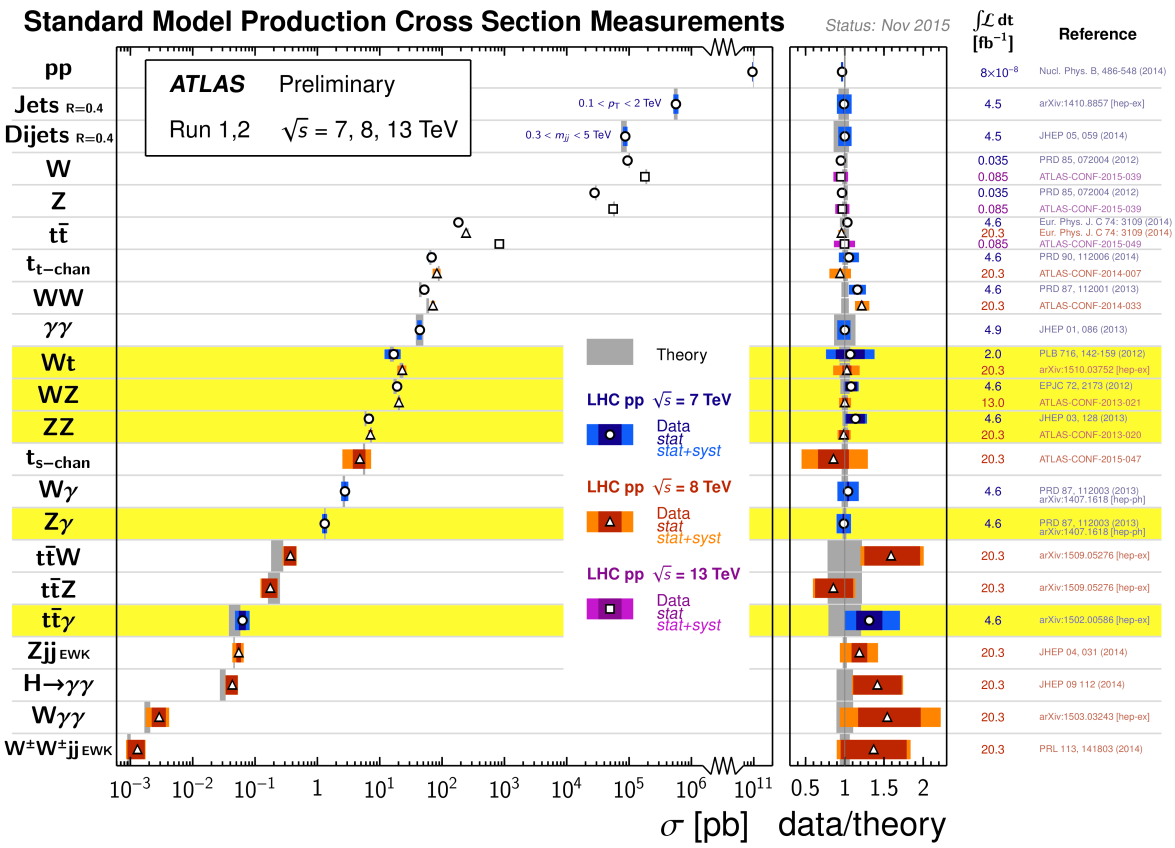

Figure 6.1: Summary of some of the cross-section measurements of standard model processes performed by the ATLAS collaboration. The values corrected for the leptonic branching fractions are compared to the theoretical expectations at next-to-leading order or higher. The ratio of the measured cross-section to the theoretical expectations is shown in the right panel of the figure along with the respective references. The highlighted processes correspond to the irreducible backgrounds to the $e\mu\gamma$ signal. Modified from Reference [94].

In order to prevent double counting between the Monte Carlo predictions and the estimation of backgrounds from misidentified objects, the truth record of the simulated events is used. Only events containing prompt photons, electrons and muons are counted as contributions to the irreducible backgrounds. The expected number of irreducible background events using the selection described in Chapter 5 is given in Table 6.1. For comparison, the signal expectation is also quoted. The cross-section of the signal is normalised to the next-to-leading order expectation from VBFNLO. The number of signal and irreducible background events are comparable and the low statistics of the analysis becomes evident. The statistical uncertainty on the Monte Carlo predictions is in the order of several tens of percent and can only be lowered by simulating more events. This was not done, as the main uncertainty comes from the finite statistics of the recorded data set as described in Section 6.4 and not from the Monte Carlo statistics. Also, the systematic uncertainties related to the simulation of the events are of the order of the statistical ones for most processes, such that the overall uncertainty on the predictions cannot be lowered by much, by generating more Monte Carlo events.

Process	Expected Events in 20.3 fb^{-1}
$WW\gamma \to e\mu\gamma$	7.9 ± 0.2(stat.) ± 0.4(syst.)
$\gamma^*/Z\gamma$	2.7 ± 0.8(stat.) ± 1.1(syst.)
WZ	2.5 ± 0.5(stat.) ± 0.5(syst.)
$t\bar{t}\gamma$	1.8 ± 0.5(stat.) ± 1.2(syst.)
$WW\gamma$ (τ contribution)	0.9 ± 0.1(stat.) ± 0.1(syst.)
Wt	0.3 ± 0.1(stat.) ± 0.05(syst.)
ZZ	0.3 ± 0.2(stat.) ± 0.05(syst.)

Table 6.1: Monte Carlo expectations for the number of signal and irreducible background events that fulfil the event selection criteria.

6.1.1 Systematic Uncertainties on the Monte Carlo Predictions

The systematic uncertainties for the estimation of the number of irreducible background events correspond to the uncertainty on the cross-section prediction due to the theoretical computations and the detector calibration and modelling. The theoretical uncertainties of the Monte Carlo cross-sections depend on the generator and its specific settings for the event generation.

- SHERPA: The cross-sections of the samples generated with SHERPA do not correspond to a fixed-order expectation, as they are calculated at leading order, but also consider higher order corrections in form of additional partons in the final state. The uncertainty of the cross-section is therefore taken as the difference between the leading order and next-to-leading order expectation. This deviation is computed using the VBFNLO generator and corresponds to about 15 % for the $\gamma^*/Z\gamma$, WZ and ZZ simulations. For the sample generated with one additional parton, i.e. the $WW\gamma$ finals states containing τ leptons, the difference is 9.3 %, due to the different kinematics of the final state. The influence of the used parton density function on the cross-section is estimated by computing the difference of the cross-section expectations obtained when using the CT10 and the MSTW2008 functions as inputs. This yields a deviation between 0.7 % and 5.2 % and is considered as additional source of systematic uncertainty. The renormalisation and factorisation scales are set to the invariant mass of the electroweak system. Their variation is taken into account by changing the scales by a factor of two. Therefore, the scales are either multiplied or divided independently by a factor of two which yields an overall of eight possible variations. The systematically varied cross-section of each variation is computed and the largest deviation from the nominal value is quoted as the scale uncertainty. They amount to 5.2, 4.2, 2.4 and 2.0 % for the $WW\gamma$ (τ), $\gamma^*/Z\gamma$, ZZ and WZ samples, respectively. All systematic components are added in quadrature to obtain the total uncertainty due to the theoretical computation for each process individually. For all samples generated with SHERPA, the largest contribution arises from the difference between the leading order and the next-to-leading order computation.

- MadGraph: The systematic uncertainties of the top pair production in association with a photon is evaluated with MadGraph, as this generator was also used for the production of the samples. The difference between the leading and the next-to-leading order computation amounts to 56 %. As additional production modes are accessible at next-to-leading order compared to the leading order, the corresponding cross-section is

also larger [95]. This difference is attributed as the systematic uncertainty from higher order corrections, as only leading order computations are used for the generation of the sample. The difference of the cross-section when using CT10 or MSTW2008 for the generation is 0.6 % and the scale uncertainty corresponds to 12.6 %. Therefore, also for this sample, the uncertainties associated with the higher order corrections are dominating the uncertainties from the theoretical computation.

- POWHEG: The Wt events are generated at next-to-leading order, resulting in smaller systematic uncertainties than for the other processes. The measurement of the fiducial cross-section of this process [96] has an uncertainty of 10 %, which is used as systematic uncertainty in this analysis, as this corresponds to the accuracy to which the theory is tested.

Other sources of systematic uncertainty of the Monte Carlo simulation arise from the detector modelling and include uncertainties of the calibration and resolution of the different subdetectors as well as the reconstruction efficiencies of the single objects in the final state. The estimation of these uncertainties is described along with the reconstruction of the objects in Chapter 4. The effect of these uncertainties on the number of selected events is assessed by varying the object momentum or efficiencies by one standard deviation, depending on the component that is under test. The uncertainties usually depend on the position and energy of the respective object, such that the whole event selection needs to be rerun on the systematically varied sample in order to evaluate the overall effect attributed to one source of systematic uncertainty. For the study of one specific uncertainty component the nominal value of the objects momentum or efficiency is first raised by one standard deviation and in a second step lowered. The maximum deviation of the event count from either variation from the nominal event yield is quoted as symmetric systematic uncertainty associated with the specific component, if it is statistically significant. The following systematic sources are taken into account:

- Energy scale, energy resolution and efficiency uncertainties for electrons.
- Energy scale, energy resolution and efficiency uncertainties for photons.
- Energy scale, energy resolution and efficiency uncertainties for muons.
- Energy scale, energy resolution and pileup suppression uncertainties for jets.
- Energy scale and resolution of the soft term of the missing transverse energy.
- Pileup description of the simulation.

The effect of the energy scale is assessed simultaneously for photons and electrons, as they are both calibrated to the electromagnetic scale. Therefore, their calibration is correlated. The resolution of the muon momentum is varied independently for the inner detector and the muon system, as no correlation between these two independent subsystems is expected. The effect of the jet pileup suppression criteria is assessed by changing the threshold value of the jet vertex fraction by ± 6 % as this covers the uncertainties introduced by the criteria, see Reference [89] for details. The missing transverse energy is also changed, when varying the momenta of the objects in the events, as $E_{\mathrm{T}}^{\mathrm{miss}}$ is computed from these objects. Still, the uncertainties due to the soft terms have to be assessed individually, as they do not enter into any other quantity.

The uncertainty attributed to the reweighting of $\langle\mu\rangle$ in simulation to match the distribution in data is $\pm 4\,\%$ and the event weights are varied accordingly to assess the influence of this systematic source.

The largest contribution of systematic uncertainty from the detector modelling for most of the samples arises due to the uncertainty on the energy measurement of the jet. Even though jets are not part of the $e\mu\gamma$ signature, their energy scale and resolution has an impact on the event yield, as all events containing jets with a p_{T} larger than 25 GeV are rejected. The jet energy uncertainty also has an impact on the relative missing transverse energy, as jets are employed for its computation. Therefore, the jet energy has an influence on two requirements imposed on the events and due to its large uncertainty, it has a sizeable impact on the event count. For the simulated $\gamma^*/Z\gamma$ events, the jet energy resolution is dominating the total systematic uncertainty and amounts to 28 %.

The single components of systematic uncertainty are added in quadrature for each background process and are summarised in Table 6.1. For all backgrounds but $\gamma^*/Z\gamma$, the uncertainty is dominated by the higher order corrections of the theoretical computation and the detector modelling has a minor systematic effect on them.

The cross-section of the signal expectation is computed at next-to-leading order. The systematic uncertainty on the signal quoted in Table 6.1 corresponds to the uncertainties due to the choice of the renormalisation and factorisation scales, the parton density variation and the uncertainties due to the detector modelling. It is only quoted for reference and is not used in the signal extraction described here.

6.2 Background from Misidentified Electrons

The signature of electrons and photons in the detector is rather similar, as explained in Section 4.1, which leads to the fact that a few percent of electrons are wrongly identified as photons. Electrons can either be misidentified as unconverted or converted photons. The former arises, for example, if an electron track is not reconstructed due to some reconstruction inefficiency of the inner detector, or if it is discarded due to bad track quality. Then no track can be associated to the energy cluster in the calorimeter and the corresponding electrons are classified as unconverted photons in the event reconstruction. The wrong identification of electrons as converted photons can happen, if their track is falsely associated to a conversion vertex. This is the case when the spacepoint in the innermost layer of the pixel detector is not reconstructed, or matched to the wrong track.

When electrons are misidentified as photons, $WZ \to \mu\nu ee$ events can mimic the $e\mu\gamma$ signal. These contributions are non-negligible, as the probability to produce WZ processes is several orders of magnitude larger than the probability to produce $WW\gamma$ events. While the effect is modelled in simulation, cross-checks have to be performed to test the validity of the description of this effect. This study was performed by the ATLAS collaboration [97] using the full data set analysed in this thesis. A discrepancy between the measurement in data and simulation of the order of a few percent was observed. Therefore, correction weights for the Monte Carlo events were computed and are applied to the simulation used in this thesis to improve the description of the misidentification of electrons. The following sections describe this study and are based on Reference [97].

6.2.1 Method Description

The electron to photon fake rate, $f_{e\to\gamma}$, can be estimated from the number of $Z \to ee$ events that contain one reconstructed electron and one reconstructed photon, $N_{e\gamma}$:

$$N_{e\gamma} = 2\epsilon \cdot f_{e\to\gamma} \cdot N_{ee}^{\text{true}}, \tag{6.1}$$

where ϵ is the average reconstruction and identification efficiency for the required electron selection criteria and N_{ee}^{true} is the true number of $Z \to ee$ events. The factor two comes from the fact that either of the electrons can be misidentified as a photon, which means that no distinction is made between $N_{e\gamma}$ and $N_{\gamma e}$. The number of true dielectron pairs, N_{ee}^{true} can also be used to describe the number of expected reconstructed electron pairs:

$$N_{ee} = \epsilon^2 \cdot N_{ee}^{\text{true}}, \tag{6.2}$$

where the efficiency is squared, as there are two electrons in the event. Acceptance effects of the detector are not covered by this description, which means that both the true and the reconstructed events are assumed to be part of the same phase space corresponding to the detector acceptance.

Equations (6.1) and (6.2) can be combined to express the electron to photon fake rate:

$$f_{e\to\gamma} = \frac{N_{e\gamma}}{2\epsilon \cdot N_{ee}^{\text{true}}} = \frac{\epsilon \cdot N_{e\gamma}}{2N_{ee}}. \tag{6.3}$$

The reconstruction and identification efficiency ϵ of the electron that is misidentified is taken into account, as it represents the probability of the electron to be reconstructed. Since the fake rate of any electron in the event is of interest, not only the reconstructed ones represented by N_{ee}, this factor has to be considered and is estimated using Monte Carlo simulation.

The event counts are obtained from two different regions in phase space: Dielectron events are selected by requiring the reconstruction of at least two electrons and electron-photon events are required to hold at least one electron and one photon. The requirements on the object reconstruction and identification are very similar to the ones employed in this thesis with a slightly tighter isolation criterion - an isolation cone radius of $R = 0.2$ is used - and a minimum transverse object momentum of $p_{\text{T}} = 20\,\text{GeV}$. Both event categories are triggered using the same trigger, to eliminate a possible bias due to this selection. The trigger requires two electromagnetic objects with a transverse momentum larger than 20 GeV in the event. For the suppression of background events arising from sources other than $Z \to ee$ decays, the invariant mass of the two objects with the largest p_{T} in the event, m_{ee} or $m_{e\gamma}$, respectively, is required to be close to the Z boson mass resonance: $85\,\text{GeV} < m_{e\kappa} < 95\,\text{GeV}$, where κ stands either for an electron or a photon. The data sample selected this way mainly consists of Z boson decays to electrons, as verified by the comparison of selected events in recorded data and from simulation.

The electron to photon fake rate is computed for the full recorded data set and for $Z \to ee$ events simulated with the Monte Carlo generator POWHEG interfaced to Pythia. A significant difference between the Monte Carlo expectations and the observations in data is found, especially for converted photons with a single track associated to them. The difference mainly arises from the incorrect estimation of the response of some pixel modules whose efficiency degraded at certain periods during the running. Due to the geometry of the modules, the discrepancy of the event simulation and observation are mainly evident in the η-distribution,

while smaller regions in ϕ are concerned. No strong dependence of the mismodelling on the transverse momentum of the photon or the average number of interactions, $\langle\mu\rangle$, is found. Therefore, the event weights to mitigate this effect are computed in nine different bins in η for the three different photon categories: unconverted or converted and associated with a single track or a double track. The correction weights range from 1.0 to 1.23 and the largest scale factors are obtained for converted photons associated with a single track, as expected. These scale factors are applied to all Monte Carlo simulations used in this thesis independent of the generator used. This is a valid assumption, as the difference in fake rate stems mainly from the mismodelling of the detector which is in common to all samples. The truth record of each event is used to determine if the photon originates from an electron or whether it is genuine. Only events where the photon with the highest p_{T} comes from an electron are reweighted. Background events containing genuine photons are considered without additional event weights as reported in Section 6.1.

6.2.2 Systematic Uncertainties on the Fake Rate Estimation

Systematic uncertainties on the event weights are computed for the following sources:

- Method bias: The event selection employed does not distinguish between whether the electron with the higher or the lower p_{T} fakes the photon. This can introduce a bias, as the photon fake rate might not be independent of the transverse electron momentum. The influence of this bias on $f_{e\to\gamma}$ is evaluated by recomputing the scale factors using the Monte Carlo simulation of single electron production. The kinematic difference with respect to Z boson decays is corrected for and the discrepancy of these event weights to the original ones is quoted as systematic uncertainty. It corresponds to 3.9 % [97].

- Z-mass window restrictions: The criteria on the ee or $e\gamma$ invariant mass selects a specific sample of Z boson decays where the boson is mostly on its mass shell. Due to bremsstrahlung and final state radiation, electrons from Z bosons that are not on the mass shell can have a different probability to fake photons. To estimate the impact of this effect on the Monte Carlo mismodelling, the electron to photon fake factor is reestimated when relaxing the criterion on the invariant mass of the two objects to: $80\,\mathrm{GeV} < m_{e\kappa} < 100\,\mathrm{GeV}$. A maximal deviation of 2 % is observed [97].

- Background contamination: In this study, jet background processes are suppressed due to the object identification criteria and the requirements on the invariant di-object mass. Still there might be events containing jets misidentified as electrons. These might have a different value of $f_{e\to\gamma}$ than prompt electrons and their potential impact needs to be taken into account. It is partly covered by the variation of the mass window restrictions explained above and can further be investigated by varying the identification requirements on the electron as well as the isolation criteria for electrons and photons. The difference of the nominal event weights and the event weights obtained with the modified selection is used as a systematic component. The variation of the identification criteria of the electrons has a maximal impact of 2.8 % and the change of the isolation criteria yields an uncertainty of 1.7 % [97].

- Electron efficiency determination: The uncertainties associated with the determination of the electron efficiency are propagated to $f_{e\to\gamma}$. This quantity has a direct effect on the

rate as can be seen in Equation (6.3). It constitutes the smallest source of systematic uncertainty, corresponding to 0.6 % [97].

The uncertainties from the different sources are summed in quadrature and yield a total uncertainty of 7 %. These uncertainties are smaller than the systematic uncertainty due to the event simulation explained in Section 6.1. They amount to 21 % and have to be taken into account, as the background estimation is based on Monte Carlo simulation. The systematic uncertainty of the estimation of the fake rate event weights is negligible compared to those.

All in all, the Monte Carlo simulation slightly underestimates the rate at which electrons are misidentified as photons. A correction is applied to mitigate this effect. Using these corrections, $(2.5 \pm 0.5(\text{stat.}) \pm 0.5(\text{syst.}))$ events from the simulation of WZ production are expected to contribute to the number of selected events.

The background arising from the misidentification of photons reconstructed as electrons is negligible for the analysis of $e\mu\gamma$ events. This is because the final state would need to contain two photons and a muon, which is the signature of $W\gamma\gamma$ events, that have a similar production probability as the $WW\gamma$ signal. Since the rate of fake electrons from photons is comparable to $f_{e\to\gamma}$, the contribution of fake electrons from the $W\gamma\gamma$ process is negligible, as verified using Monte Carlo simulations.

6.3 Background from Misidentified Jets

The detector signature of jets might be similar to the one of muons, electrons or photons. While the misidentification is rather unlikely, it is not impossible and since the probability to produce jets is orders of magnitudes larger than the one to produce $e\mu\gamma$ final states, the contribution of fake objects due to misidentified jets has to be accounted for in this analysis.

Jets can be detected in the muon system in case their shower is not fully contained in the calorimeter. Therefore, a muon can be reconstructed even though it originates from a jet and not from the hard interaction vertex. The probability of a jet being misidentified as a muon is very low and in this analysis it is further suppressed by the way the overlap between the two objects is resolved. Any muon that is close to a jet is discarded, which means that only jets which are not reconstructed in the calorimeter, but in the inner detector and the muons system, can mimic a muon, since otherwise the muon is discarded to begin with. The study of simulated $W\gamma$ processes in association with jets shows that the contribution of jets misidentified as muons to the selected events is negligible. Therefore, this Monte Carlo sample is used to estimate their contribution and a conservative uncertainty of 100 % is assumed, since the simulation might underestimate the contribution. In total (0.1 ± 0.1) selected events are expected to come from jets being misidentified as muons.

The energy deposition of a jet in the calorimeter can be misidentified as an electron or a photon in case the shower fulfils the identification criteria of the specific object (see Section 4.1.1). Studies using simulated events show that this contribution is not negligible. It is estimated using a sideband method referred to as ABCD method in the following discussions. Three additional event selections are defined for each background in order to derive the number of events containing misidentified jets.

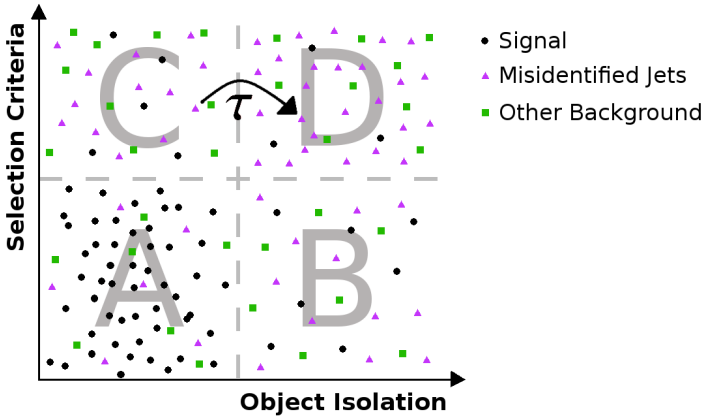

Figure 6.2: Schematic sketch of the four phase space regions A, B, C and D of the ABCD method. The distribution of signal (round markers) and background events containing misidentified jets (triangles) is indicated along with the other background components (squares) that are estimated using Monte Carlo. Also shown is the transfer factor τ that relates the number of events containing misidentified jets in the different regions.

6.3.1 The ABCD Method

The ABCD method [83] can be used to estimate the contribution of specific background events to the selected data sample. The advantage of the method is that it does not only rely on Monte Carlo simulation, but uses four disjoint phase space regions in order to estimate the background contribution. This way, processes that are not well-modelled in simulation can be estimated. Yet, the method can only be used, if the sideband selections can be defined based on two sets of uncorrelated observables.

A general sketch of the method can be seen in Figure 6.2. There, the four disjoint regions in phase space are indicated along with the distribution of the signal and background events. The contribution labelled "misidentified jets" is the one being estimated with the method. The component labelled "other background" refers to the contribution of other physics processes in the selected phase space. Ideally, this contribution is low and can be corrected for. The signal should be concentrated in the signal region labelled A and only have small contributions to regions B, C and D. The distributions along the two axes of the background component being estimated have to factorise, which is also indicated in the sketch.

The above requirements have to be considered when defining the requirements for the different regions of the method. The starting point for the selection criteria is the event selection described in Section 5.4 which defines the signal region. The method requires the additional regions, referred to as control regions, to be enriched in the background process that is being estimated. For photons or electrons from misidentified jets, this can be achieved by inverting the selection criterion on the object isolation and keeping the remaining requirements of the event selection. As depicted in Figure 5.4b for the photon case, a sample with fewer prompt photon objects is selected when inverting the requirement on $E_{\mathrm{T}}^{\mathrm{iso},\gamma}$. The control region defined this way is called region B in the following. For the estimation of electrons from misidentified jets, the observable $E_{\mathrm{T}}^{\mathrm{iso,\,e}}$ is used to define region B.

The definition of the two additional control regions, C and D, also needs to enrich the selected data with background events while at the same time not influencing the distribution of

the object isolation. The definition of region C introduces additional criteria to deviate from the signal region selection, but keeps the object isolation requirement fixed. The selection criteria of region D are the same as for region C with the only difference being the object isolation which is inverted. These selection criteria differ for electrons and photons from misidentified jets and are detailed in the respective sections below.

If the conditions described above are met, the number of events containing fake objects from misidentified jets in the different regions are related. Since the event counts of this background component in the signal region, $N_{\mathrm{A}}^{\mathrm{fake}}$, and the control region B, $N_{\mathrm{B}}^{\mathrm{fake}}$, are related by the same requirements as the event counts in regions C and D, their ratio is the same. Therefore, the transfer factor τ can be defined as:

$$\tau = \frac{N_{\mathrm{B}}^{\mathrm{fake}}}{N_{\mathrm{A}}^{\mathrm{fake}}} = \frac{N_{\mathrm{D}}^{\mathrm{fake}}}{N_{\mathrm{C}}^{\mathrm{fake}}}. \tag{6.4}$$

If the two sets of selection criteria defining the method do not factorise exactly, this bias can be corrected for by introducing the correlation factor ρ that is estimated using Monte Carlo simulation:

$$\tau = \rho \cdot \frac{N_{\mathrm{B}}^{\mathrm{fake}}}{N_{\mathrm{A}}^{\mathrm{fake}}} = \frac{N_{\mathrm{D}}^{\mathrm{fake}}}{N_{\mathrm{C}}^{\mathrm{fake}}} \Rightarrow \rho = \frac{N_{\mathrm{A}}^{\mathrm{fake}} \cdot N_{\mathrm{D}}^{\mathrm{fake}}}{N_{\mathrm{B}}^{\mathrm{fake}} \cdot N_{\mathrm{C}}^{\mathrm{fake}}}, \tag{6.5}$$

and $\rho = 1$ if the distributions factorise.

The above relations only hold for the background process being estimated, but the event count in the four different regions i consists of three components: the number of $WW\gamma$ signal events, $N_i^{WW\gamma}$, the number of background events from other physics processes, N_i^{MC}, and the number of events containing misidentified jets, N_i^{fake}. Therefore, the event count in each region i can be written as:

$$N_i = N_i^{WW\gamma} + N_i^{\mathrm{fake}} + N_i^{\mathrm{MC}}. \tag{6.6}$$

The number of other background events, N_i^{MC}, is estimated using the Monte Carlo simulation described in Sections 6.1 and 6.2. Since the number of signal events in the signal region is the quantity being estimated in this analysis, only the relative normalisation of this component in the different regions is taken from simulation. This is done by introducing the signal leakage c_i that is defined as the ratio of signal events in region i to the number of signal events in the signal region:

$$c_i = \frac{N_i^{WW\gamma}}{N_{\mathrm{A}}^{WW\gamma}}. \tag{6.7}$$

The signal leakage is supposed to be small in each of the control regions and it is by definition equal to one in the signal region.

With these definitions, the expected event count in each of the regions can be written as:

$$\begin{aligned}
N_{\mathrm{A}}^{\mathrm{exp.}} &= N_{\mathrm{A}}^{\mathrm{MC}} + c_{\mathrm{A}} * N_{\mathrm{A}}^{WW\gamma} + N_{\mathrm{A}}^{\mathrm{fake}}, \\
N_{\mathrm{B}}^{\mathrm{exp.}} &= N_{\mathrm{B}}^{\mathrm{MC}} + c_{\mathrm{B}} * N_{\mathrm{A}}^{WW\gamma} + \tau * N_{\mathrm{A}}^{\mathrm{fake}}, \\
N_{\mathrm{C}}^{\mathrm{exp.}} &= N_{\mathrm{C}}^{\mathrm{MC}} + c_{\mathrm{C}} * N_{\mathrm{A}}^{WW\gamma} + N_{\mathrm{C}}^{\mathrm{fake}}, \\
N_{\mathrm{D}}^{\mathrm{exp.}} &= N_{\mathrm{D}}^{\mathrm{MC}} + c_{\mathrm{D}} * N_{\mathrm{A}}^{WW\gamma} + \rho * \tau * N_{\mathrm{C}}^{\mathrm{fake}}.
\end{aligned} \tag{6.8}$$

The unknowns of this equation are the number of signal events in the signal region, $N_{\mathrm{A}}^{WW\gamma}$, the number of events with fake objects in regions A and C, $N_{\mathrm{A}}^{\mathrm{fake}}$ and $N_{\mathrm{C}}^{\mathrm{fake}}$ respectively, as

well as the transfer factor τ. All other observables are estimated using Monte Carlo simulation and the four unknowns can be determined using the event counts in the four regions defined by the method.

Solving the set of equations (6.8) can be done analytically, but in this work a likelihood method is used. This has the advantage, that the results are robust even for low statistics which is present in this analysis. The likelihood formulation also facilitates the simultaneous estimation of the number of background events coming from jets misidentified as electrons and from jets misidentified as photons. As both components can be derived using the ABCD method, their estimation can be combined, as described after the discussion of the single methods.

The construction of the likelihood function is based on the fact that the expected number of events in each of the four regions obey Poisson statistics. Therefore, the likelihood for the observation of N_i events in region i, is given by:

$$\mathcal{L}(N_i|N_i^{\text{exp.}}) = Pois(N_i; N_i^{\text{exp.}}) = \frac{e^{-N_i^{\text{exp.}}}(N_i^{\text{exp.}})^{N_i}}{N_i!}, \tag{6.9}$$

where $N_i^{\text{exp.}}$ is defined in Equation (6.8). The joint likelihood function for the measurement of the observed event counts in the four regions is obtained by the product of the Poissonian probabilities:

$$\mathcal{L}(N_{\text{A}}, N_{\text{B}}, N_{\text{C}}, N_{\text{D}}|N_{\text{A}}^{WW\gamma}, N_{\text{A}}^{\text{fake}}, N_{\text{C}}^{\text{fake}}, \tau) = \prod_{i=1}^{4} Pois(N_i; N_i^{\text{exp.}}), \tag{6.10}$$

where the input parameters from Monte Carlo simulation, N_i^{MC}, c_i and ρ, are fixed. In order to take their respective uncertainty into account, the input parameters can be included into the model as distributed according to a Gaussian distribution whose mean corresponds to the expected value of the parameter and whose standard deviation corresponds to the expected uncertainty of the parameter. For the correlation factor, for example, this yields:

$$\mathcal{L}(\rho^{\text{obs.}}|\rho, \sigma_\rho) = Gauss(\rho^{\text{obs.}}; \rho, \sigma_\rho) = \frac{1}{\sigma_\rho\sqrt{2\pi}} e^{-\frac{(\rho^{\text{obs.}}-\rho)^2}{2\sigma_\rho^2}}, \tag{6.11}$$

where the index obs. refers to the observed value of ρ after the maximisation of the likelihood. The input parameters from Monte Carlo simulation, i.e. N_i^{MC}, c_i and ρ are collectively referred to as constrained parameters $\boldsymbol{\mathcal{C}}$. They are included in the model by multiplying the likelihood function from Equation (6.10) with their respective likelihoods, i.e. Gaussian distributions. Therefore, the likelihood of the signal can be formulated in terms of the observables $\boldsymbol{\Omega} = \{N_{\text{A}}^{WW\gamma}, N_{\text{A}}^{\text{fake}}, N_{\text{C}}^{\text{fake}}, \tau\}$ and the constrained parameters $\boldsymbol{\mathcal{C}} = \{N_i^{\text{MC}}, c_i, \rho\}$:

$$\mathcal{L}(N_i|\boldsymbol{\Omega}, \boldsymbol{\mathcal{C}}) = Gauss(\rho^{\text{obs.}}) \cdot \prod_{i=1}^{4} Pois(N_i; N_i^{\text{exp.}}) \cdot Gauss(N_i^{\text{MC, obs.}}) \cdot Gauss(c_i^{\text{obs.}}), \tag{6.12}$$

where $Gauss(c_{\text{A}}^{\text{obs.}}) = 1$ and for shorter notation the parameters of the Gaussian distributions are omitted.

The number of signal events in the signal region is obtained by fitting the joint model to the observed event counts in the four regions. Therefore, the likelihood function (6.12) is maximised with respect to its parameters considering the data. Numerical methods implemented in the MINUIT package [98] interfaced to the framework ROOT [99] are used to this end.

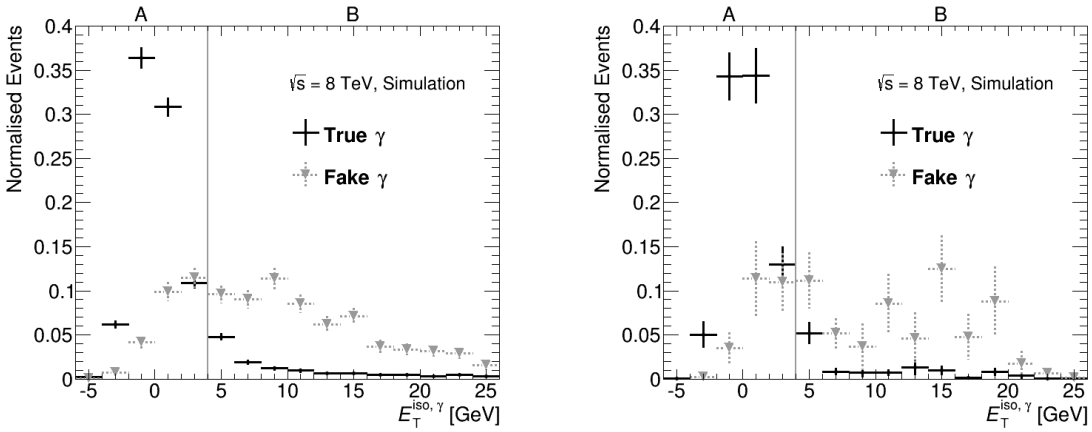

Figure 6.3: Normalised $E_{\mathrm{T}}^{\mathrm{iso},\,\gamma}$-distribution for prompt and fake photons after the object selection (a) and after the full event selection (b). The classification of the photon is done using the truth record of the event generation. The selection with $E_{\mathrm{T}}^{\mathrm{iso},\,\gamma} < 4\,\mathrm{GeV}$ corresponds to region A of the ABCD method and $E_{\mathrm{T}}^{\mathrm{iso},\,\gamma} \geq 4\,\mathrm{GeV}$ to region B.

6.3.2 The ABCD Method for Jets Misidentified as Photons

The ABCD method is employed for the determination of the number of events in the signal region that contain photons which are actually jets, but still fulfil all photon identification criteria. The distinction between region A and B as well as region C and D is made by inverting the requirement on the isolation energy of the photon with the highest p_{T} in the event. The expected discrimination power of this criterion between prompt photons and photons originating from jets can be seen in Figure 6.3. The normalised event count distribution of the transverse photon isolation energy is shown for simulated events. Reconstructed photons are matched to a photon from the generator using its truth record. They are shown in black and labelled "True γ". The term "Fake γ" refers to photons that are reconstructed but cannot be associated with an electromagnetic object on generator level. These photons originate from hadrons and have a wider $E_{\mathrm{T}}^{\mathrm{iso},\,\gamma}$-distribution. Figure 6.3a shows the distributions after the basic object selection and Figure 6.3b shows the events selected by the full event selection. The distributions are shown for two different steps in the event selection process, as the statistical uncertainties are sizeable after the background rejection criteria. Still both figures depict the same situation: a clear peak around $E_{\mathrm{T}}^{\mathrm{iso},\,\gamma} = 0\,\mathrm{GeV}$ is visible for the prompt photon distribution, while fake photons exhibit a large tail towards high values of the transverse photon isolation. The Monte Carlo simulation of all irreducible processes listed in Section 5.2 is used along with the simulation of the production of W boson pairs and pairs of top-antitop quarks, where additional jets in the event can be misidentified as photons.

For the ABCD method to work, the selection criteria separating regions A and C as well as regions B and D, should not influence the isolation distribution of the fake photons while enriching the control samples with many events containing photons from misidentified jets. This is achieved by defining an event selection with slightly modified photon identification criteria (see Section 4.1.1). Reference [83] describes these so called non-tight identification criteria, that require the photon to fail at least one out of four identification criteria associated

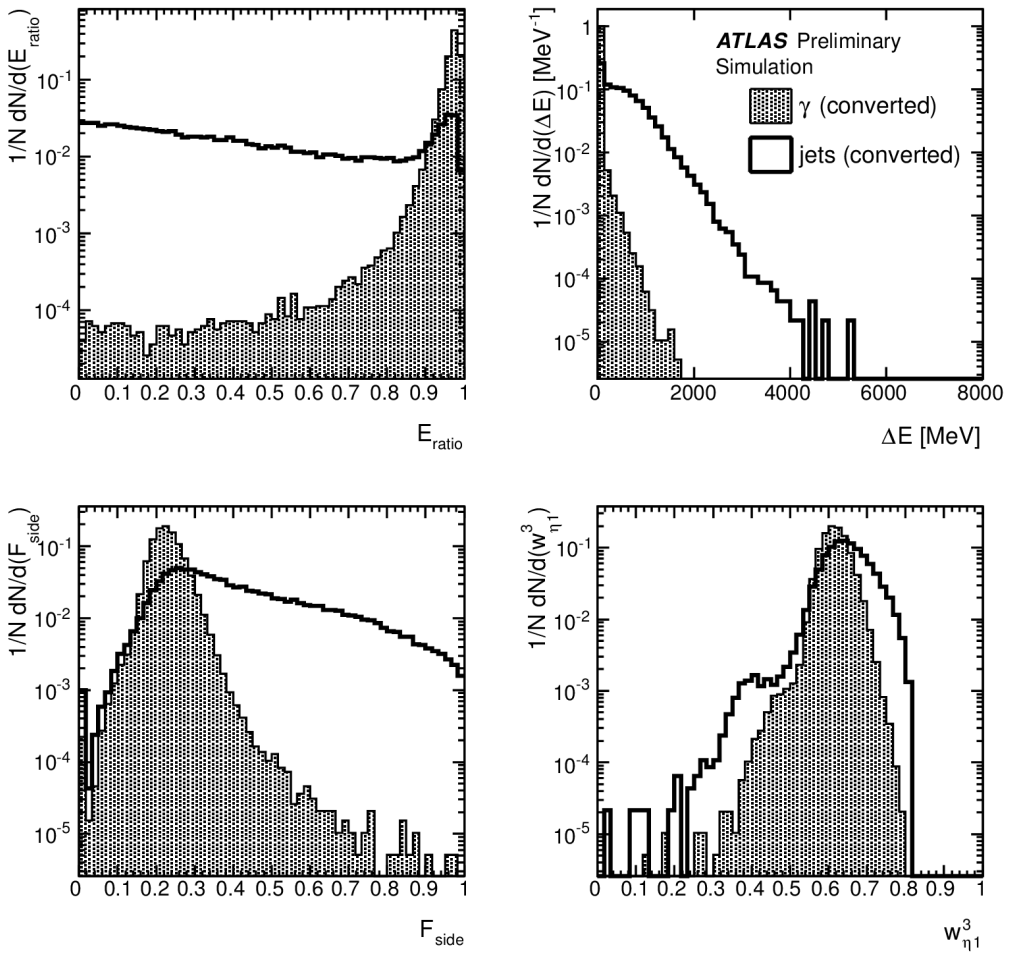

Figure 6.4: Normalised distributions of the strip layer variables used for the non-tight photon identification. The region of $|\eta| < 0.6$ is shown for converted photons by the hatched and jets by the empty histograms for objects with $E_{\mathrm{T}} > 20\,\mathrm{GeV}$ [80].

with the strip layer. These are:

- E_{ratio}, the ratio of the energy difference between the cell with largest and second largest energy deposition and the sum of these two energies.
- ΔE, the difference in energy associated with the second maximum in the strip layer and the minimal energy value found in a strip between the first and the second maximum.
- F_{side}, the fraction of energy deposited within seven strips outside the core of three central strips with the maximal energy deposition.
- $w_{s\,3}$ the shower width for three strips around the cell containing the maximal energy deposition (referred to as $w^3_{\eta\,1}$ in Figures 6.4 and 6.5).

A more technical definition can be found in Section 4.1.1. All other identification criteria have to be passed, as they show a non-negligible correlation with the isolation distribution

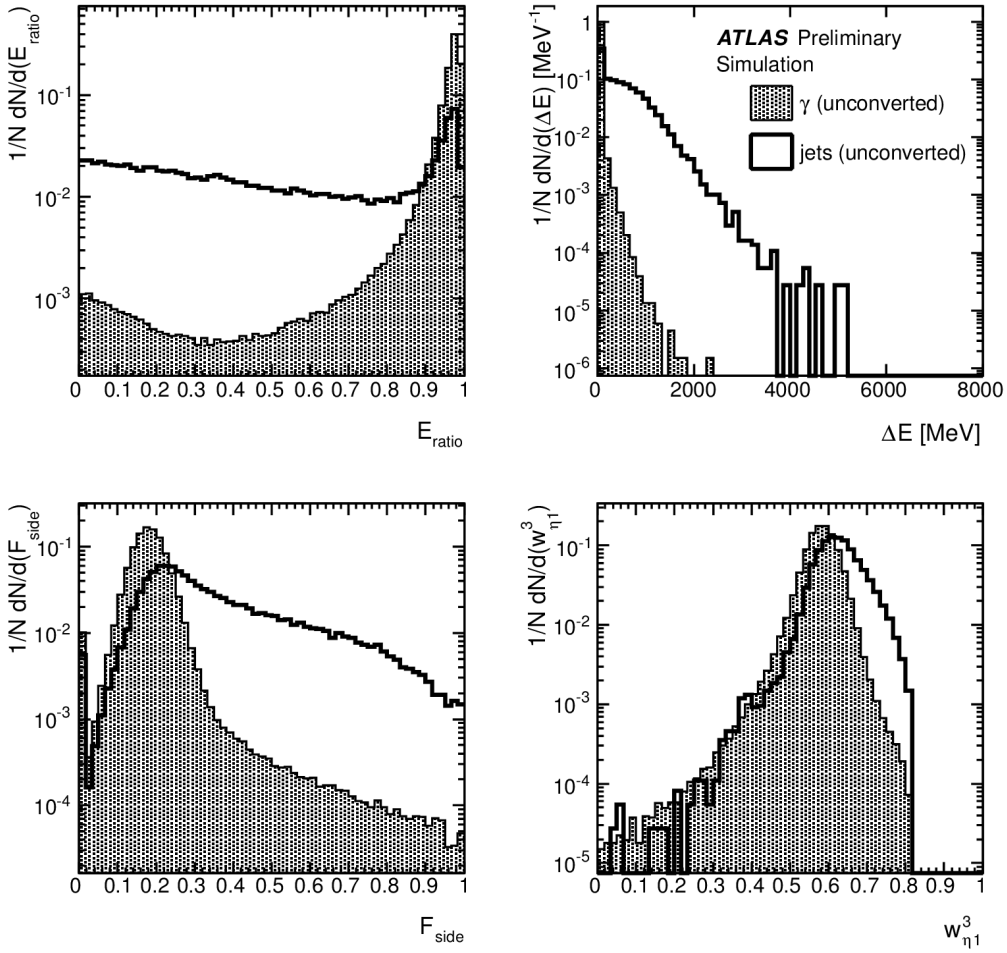

Figure 6.5: Normalised distributions of the strip layer variables used for the non-tight photon identification. The region of $|\eta| < 0.6$ is shown for unconverted photons by the hatched and jets by the empty histograms for objects with $E_{\mathrm{T}} > 20\,\mathrm{GeV}$ [80].

of the photon. The expected distributions of these four variables for photons and jets are shown in Figure 6.4 for converted and in Figure 6.5 for unconverted photon candidates. As the distributions deviate for photons and jets, inverting these criteria selects mainly jets and few genuine photons.

The impact of the non-tight identification on the transverse isolation energy of misidentified jets needs to be checked, as the method relies on the fact that it is robust under the control region definitions. This is done by comparing the $E_{\mathrm{T}}^{\mathrm{iso,\ fake}\,\gamma}$-distribution in regions A and C as well as in regions B and D. Figure 6.6 shows the distributions after the object selection on the left and after the full event selection on the right. In both cases the distributions are in agreement, although the distributions after applying all selection criteria have large statistical uncertainties. The same Monte Carlo simulation as for Figure 6.3 is employed. The influence of the modification of the photon isolation on the signal or on the other backgrounds is of no interest, since these parameters are taken into account in the method using Monte Carlo simulation. All in all, the transverse isolation energy of the photon and the identification

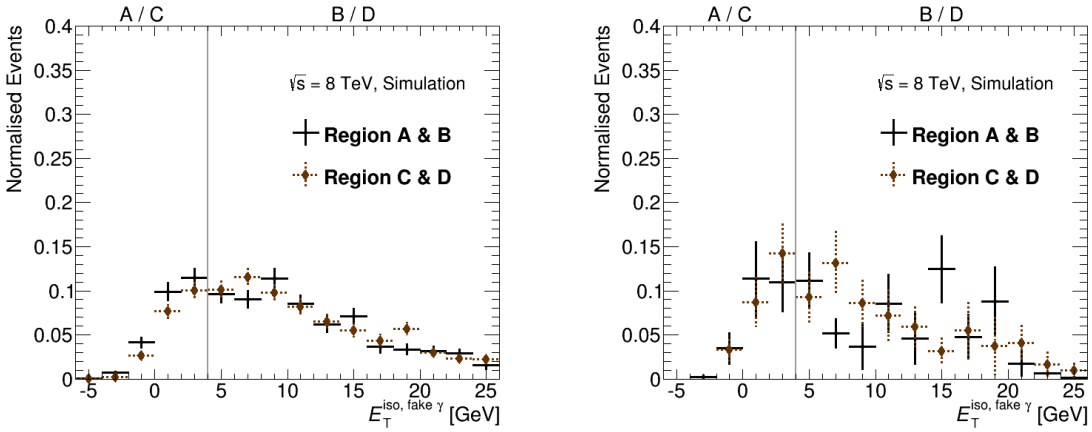

Figure 6.6: Normalised $E_{\mathrm{T}}^{\mathrm{iso,\ fake}\,\gamma}$-distribution for fake photons in the different regions of the ABCD method after the object selection (a) and after the full event selection (b). Photons in regions A and B (black) are selected using the tight identification criteria, while photons in region C and D (brown) are identified with the non-tight selection. The classification of the photon is done using the truth record of the event generation.

criteria are good candidates for the definition of the control regions of the ABCD method.

The trigger `EF_mu18_2g10_medium`, used for the selection of the data sample, does not impose any requirements on the isolation of the photon, but it imposes certain criteria on the shower shapes of the electromagnetic object in order to keep the event rate practicable. Therefore, it cannot be used to select the events containing non-tight photons, as parts of these events are rejected by the trigger. Thus, a trigger is chosen that does not impose any criteria on the photon, but only requires the presence of an energetic electron in the event. The p_{T}-threshold of the electron activating the trigger is 24 GeV and therefore slightly higher than the minimal transverse momentum required by the analysis. However, this influences both control regions C and D in the same way and as only their ratio is exploited by the ABCD method the result is not influenced by this criterion. In order to recover a small loss in efficiency for large transverse electron momenta, events triggered by an item that requires at least one electron with $p_{\mathrm{T}} > 60$ GeV are also considered for analysis. The influence of the trigger on the $E_{\mathrm{T}}^{\mathrm{iso},\gamma}$-distribution of non-tight photons was studied and found to be negligible.

In order to verify that the contribution of the signal in the control regions is small and that the majority of events in these regions comes from misidentified jets, the expected distribution of the transverse photon isolation energy in regions A and B is shown in Figure 6.7a. The same quantity is shown for the events in region C and D in Figure 6.7b. The Monte Carlo expectations are shown as stacked histograms, which means that the single components are added up. The simulation is weighted to correspond to the integrated luminosity of the recorded data set, $\mathrm{L_{int.}} = 20.3\,\mathrm{fb}^{-1}$, and the statistical uncertainty of the Monte Carlo predictions is indicated by the hatched band. All control regions are expected to be dominated by events from misidentified jets shown in light grey. In order to avoid double counting, the photons and electrons of the simulated backgrounds are matched to the truth record of the event generation. For the simulated background containing fake objects, i.e. $W\gamma + jets$, multijet production, WW and $t\bar{t}$, this matching is inverted for the respective object in the event. The component

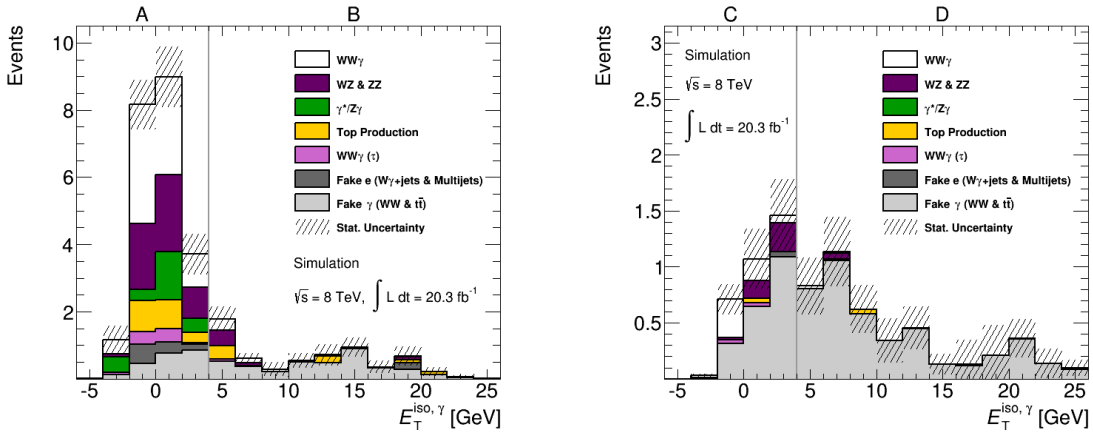

Figure 6.7: Expected distribution of the photon isolation energy for reconstructed photons in the four regions of the ABCD method. Photons identified with the tight criteria corresponding to regions A and B are shown in (a). Figure (b) shows the $E_{\mathrm{T}}^{\mathrm{iso},\,\gamma}$-distribution for photons identified with the non-tight criteria corresponding to regions C and D. The Monte Carlo expectations are scaled to correspond to an integrated luminosity of $20.3\,\mathrm{fb}^{-1}$ and the label top production refers to Wt and $t\bar{t}$ processes. The truth record of the simulation is used to match the final state objects to the reconstructed ones. The statistical uncertainty of the simulation is indicated by the hatched band.

where muons are unmatched in simulation is not shown, as it is negligible. The contribution of fake photons from electrons is included in the simulated components and corrected for as described in Section 6.2. The mechanism of electrons being misidentified as photons only contributes to the simulated WZ and ZZ events.

The Monte Carlo confirms the applicability of the ABCD method to estimate the contribution of fake photons coming from misidentified jets. Instead of reporting the results here, first the validity of the ABCD method for the estimation of fake electrons from misidentified jets is reported. As the fake electrons and fake photons both contribute background events to the signal region, the ABCD methods for the respective event count estimation are united and evaluated simultaneously.

6.3.3 The ABCD Method for Jets Misidentified as Electrons

Prompt electrons also differ from misidentified jets in the distribution of their transverse isolation energy as can be seen in Figure 6.8. On the left hand side the expected transverse isolation energy is shown for the electron with the highest p_{T} in the event after the object selection. The right hand figure shows the same situation after the full event selection is applied and therefore has much larger statistical uncertainties. The classification of the electrons is done by using the truth record of the event generation and the electrons are denoted as fake if they originate from hadrons. A deviation of the $E_{\mathrm{T}}^{\mathrm{iso},\,\mathrm{e}}$-distribution is observable for prompt electrons and electrons coming from misidentified jets. The former exhibits a clear peak around $E_{\mathrm{T}}^{\mathrm{iso},\,\mathrm{e}} = 0\,\mathrm{GeV}$ while the latter manifests a much wider distribution with a tail towards high values of the transverse electron isolation. The Monte Carlo simulation of all irreducible processes listed in Section 5.2 is used along with the contribution of the production of $W\gamma$ events in association with jets which can be misidentified as electrons. The distinction

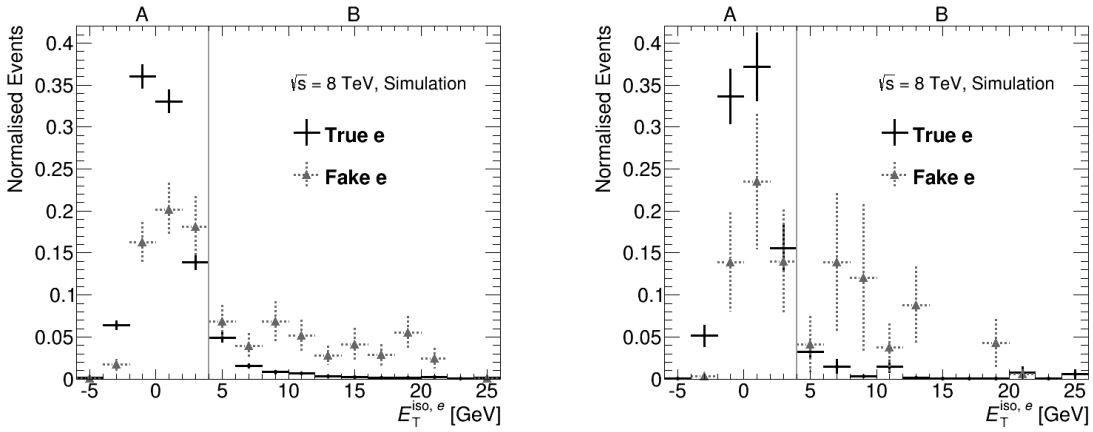

(a) **(b)**

Figure 6.8: Normalised $E_{\mathrm{T}}^{\mathrm{iso,\,e}}$-distribution for prompt and fake electrons after the object selection (a) and after the full event selection (b). The classification of the electrons is done using the truth record of the event generation. The selection with $E_{\mathrm{T}}^{\mathrm{iso,\,e}} < 4\,\mathrm{GeV}$ corresponds to region A of the ABCD method, $E_{\mathrm{T}}^{\mathrm{iso,\,e}} \geq 4\,\mathrm{GeV}$ to region B.

between the regions of the ABCD methods is performed by the transverse isolation threshold of $E_{\mathrm{T}}^{\mathrm{iso,\,e}} = 4\,\mathrm{GeV}$.

The second set of requirements of the ABCD method should define a sample dominated by fake electrons from jets. As the electron identification criteria do not rely as much on the strip layer observables as the photons, an equivalent non-tight identification cannot be formulated for electrons without introducing a bias on $E_{\mathrm{T}}^{\mathrm{iso,\,e}}$. But since the production of jet pairs is abundant at the LHC, a set of criteria can be found to select these dijet events where one of the jets is misidentified as an electron. This is referred to as electron-jet selection and is based on the same object definition as the rest of the analysis. The only difference in this respect is a lower p_{T} requirement imposed on the jets. Jets with a transverse momentum as low as 15 GeV are selected, because dijet events are expected to be balanced in transverse momentum and the p_{T} threshold of the electron it balances against is kept at 20 GeV.

The electron-jet selection requires at least one electron and at least one jet to be reconstructed in the event. As the jets in dijet events tend to be back-to-back, the electron and jet with the largest p_{T} in the event are required to have an azimuthal separation of at least $\Delta\phi = 0.7$. Otherwise, they might stem from a secondary decay of the same source. The sample selected with these criteria still contains many events with prompt leptons from W or Z boson production in association with jets. In order to suppress electrons from W bosons the transverse mass of the event is restricted. It is computed from the selected electron and the missing transverse energy in the event according to:

$$m_{\mathrm{T}} = \sqrt{2E_{\mathrm{T}}^{e}E_{\mathrm{T}}^{\mathrm{miss}}(1 - cos\Delta\phi)}, \tag{6.13}$$

where $\Delta\phi$ refers to the difference in azimuthal angle between the direction of the electron and the missing transverse momentum. Typically, events containing one W boson have values of m_{T} around 75 GeV [100] with a rather wide peak, which is why for the electron-jet selection only events with $m_{\mathrm{T}} \leq 30\,\mathrm{GeV}$ are accepted. Events containing prompt electrons from Z boson decays are rejected by computing the invariant dilepton mass, m_{ll}, in case there is

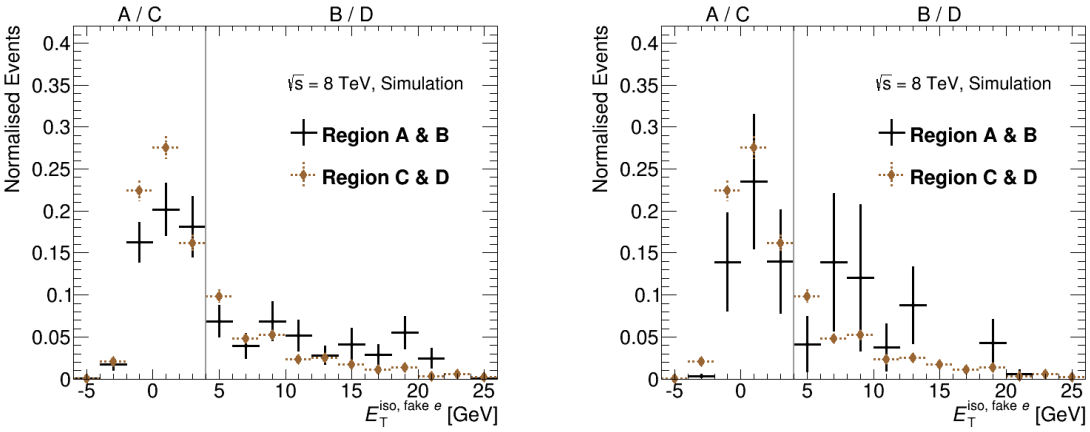

Figure 6.9: Normalised $E_{\mathrm{T}}^{\mathrm{iso,\ fake}\,e}$-distribution for fake electrons in the different regions of the ABCD method. Figure 6.9a shows the distribution in regions A and B (black) after the object selection and Figure 6.9b after the full event selection. The transverse isolation energy shown for regions C an D (brown) corresponds to the electron-jet selection in both figures. The classification of the electron is done using the truth record of the event generation.

more than one reconstructed lepton in the event. These events are rejected, if their invariant dilepton mass is close to the Z boson mass, m_Z, by requiring $|m_{ll} - m_Z| > 7\,\mathrm{GeV}$. The sample defined this way contains mainly events where the electron comes from misidentified jets, as the contribution from genuine electron production mechanism is highly suppressed by the selection criteria and the probability for dijet production is dominating at the LHC.

Since the criteria defining the electron-jet selection differ from the signal region requirements, the trigger item has to be changed as well. Triggering on three objects in the final state when only two are required biases the data set. The electron requirement of the electron-jet selection criteria is exploited for the choice of the trigger. Still, the trigger cannot impose any requirements on the isolation of the electron, as this would introduce a bias on the event count in regions C and D. Only a pre-scaled trigger fulfilling all these requirements is available. It triggers the readout when electrons with a p_{T} larger than 15 GeV are in the event. The pre-scales varied over the data taking and on average, the trigger accepted one event in a thousand that fulfilled its requirements yielding an integrated luminosity of $(20.8 \pm 0.4)\,\mathrm{pb}^{-1}$. Due to the abundance of dijet events, the number of events is still large enough for the ABCD method to work. The efficiency of the trigger to select isolated electrons, i.e. $E_{\mathrm{T}}^{\mathrm{iso,\,e}} < 4\,\mathrm{GeV}$, is a bit higher than its efficiency to trigger events that contain electrons with large values of transverse isolation energy. A trigger efficiency difference of $(6.7 \pm 0.7)\,\%$ is observed when studying simulated multijet events. This small difference biases the ratio of events in region C and D and therefore the event counts are corrected, as it is statistically significant.

The distribution of the transverse isolation energy of fake electrons in the different ABCD regions is shown in Figure 6.9. The left hand figure shows the distribution in regions A and B after the object selection and the figure on the right side after the full event selection is applied. The distribution shown for regions C and D is the same in both figures and corresponds to the electrons selected by the electron-jet selection. It exhibits smaller statistical uncertainties than the distributions in regions A and B. The figure shows the simulation of all irreducible

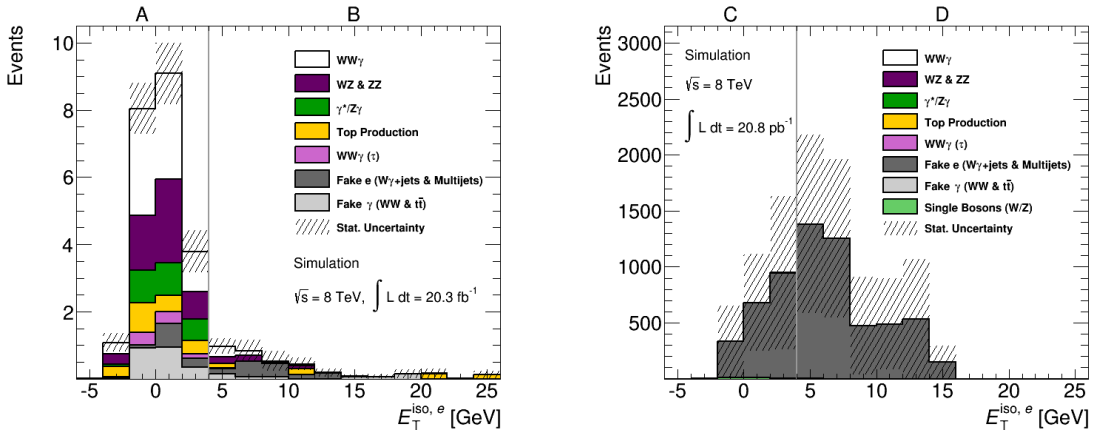

(a) (b)

Figure 6.10: Expected distribution of the electron isolation energy for reconstructed photons in the different regions of the ABCD method. Electrons selected with the default event selection corresponding to regions A and B are shown in Figure 6.10a. Figure 6.10b shows the $E_{\mathrm{T}}^{\mathrm{iso,\,e}}$-distribution for electrons selected using the electron-jet criteria corresponding to regions C and D. The Monte Carlo expectations are scaled to correspond to an the integrated luminosity of the data sample and the label top production refers to Wt and $t\bar{t}$ processes. The truth record of the simulation is used to match the final state objects to the reconstructed ones. Single W or Z boson production only contributes to the electron-jet selection due to the lower multiplicity of final state objects compared to the default event selection. The statistical uncertainty of the simulation is indicated by the hatched band.

backgrounds together with the production of $W\gamma$ events in association with jets. The agreement of the distributions can be verified, which allows the conclusion that the electron-jet selection does not influence the distribution of the transverse isolation energy of fake electrons, which is a necessary condition for the applicability of the ABCD method.

The Monte Carlo expectations for the different regions of the ABCD method to estimate fake electrons from misidentified jets is shown in Figure 6.10. The figure on the left shows the expectations in regions A and B using the default event selection that corresponds to an integrated luminosity of $20.3\,\mathrm{fb}^{-1}$. Few signal events are observable in region B, but there are events containing fake electrons. The right hand figure shows the expected events in regions C and D using the electron-jet selection criteria and the associated trigger. Therefore, the integrated luminosity the expectations are scaled to is much smaller than for the left hand figure and corresponds to $\mathrm{L_{int.}} = 20.8\,\mathrm{pb}^{-1}$. The main contribution comes from events containing fake electrons from the simulation of multijet events. Due to the considerable cross-section of the process, it is computationally not feasible to generate a data set corresponding to a large integrated luminosity. One hundred million events were generated, yielding a data set that is three orders of magnitude smaller than the one recorded with the prescaled trigger. Therefore, this simulation has very large statistical uncertainties that are indicated by the hatched band. Also shown but not visible is the background from single W or Z boson production that does not contribute to the signal region event selection, but to the electron-jet selection due to the smaller final state multiplicity. The contribution from any other source, including the signal, to the electron-jet control regions is negligible and therefore, the necessary conditions of the ABCD method are fulfilled.

6.3.4 Combination of the ABCD Methods for Jets Misidentified as Photons and as Electrons

The estimation of misidentified jet backgrounds relies on the event count in the different regions defined by the ABCD method. As the signal region coincides for the estimation of fake photons and fake electrons, the control region composition defined by the set of equations (6.8) can be extended. Denoting the variables for the estimation of fake photons by the index γ and the ones for the estimation of fake electrons with an index e, the expected number of events in the signal region and the six controls regions - three for each background component - can be written as:

$$\begin{aligned}
N_{\mathrm{A}}^{\mathrm{exp.}} &= N_{\mathrm{A}}^{\mathrm{MC}} + c_{\mathrm{A}} \ * \ N_{\mathrm{A}}^{WW\gamma} + N_{\mathrm{A}}^{\mathrm{fake}\,\gamma} \ + \qquad N_{\mathrm{A}}^{\mathrm{fake}\,e}, \\
N_{\mathrm{B}_\gamma}^{\mathrm{exp.}} &= N_{\mathrm{B}_\gamma}^{\mathrm{MC}} + c_{\mathrm{B}_\gamma} * (N_{\mathrm{A}}^{WW\gamma} + N_{\mathrm{A}}^{\mathrm{fake}\,e}) + \qquad \tau_\gamma * N_{\mathrm{A}}^{\mathrm{fake}\,\gamma}, \\
N_{\mathrm{B}_e}^{\mathrm{exp.}} &= N_{\mathrm{B}_e}^{\mathrm{MC}} + c_{\mathrm{B}_e} * (N_{\mathrm{A}}^{WW\gamma} + N_{\mathrm{A}}^{\mathrm{fake}\,\gamma}) + \qquad \tau_e * N_{\mathrm{A}}^{\mathrm{fake}\,e}, \\
N_{\mathrm{C}_\gamma}^{\mathrm{exp.}} &= N_{\mathrm{C}_\gamma}^{\mathrm{MC}} + c_{\mathrm{C}_\gamma} * (N_{\mathrm{A}}^{WW\gamma} + N_{\mathrm{A}}^{\mathrm{fake}\,e}) + \qquad N_{\mathrm{C}_\gamma}^{\mathrm{fake}\,\gamma}, \\
N_{\mathrm{C}_e}^{\mathrm{exp.}} &= N_{\mathrm{C}_e}^{\mathrm{MC}} + c_{\mathrm{C}_e} * (N_{\mathrm{A}}^{WW\gamma} + N_{\mathrm{A}}^{\mathrm{fake}\,\gamma}) + \qquad N_{\mathrm{C}_e}^{\mathrm{fake}\,e}, \\
N_{\mathrm{D}_\gamma}^{\mathrm{exp.}} &= N_{\mathrm{D}_\gamma}^{\mathrm{MC}} + c_{\mathrm{D}_\gamma} * (N_{\mathrm{A}}^{WW\gamma} + N_{\mathrm{A}}^{\mathrm{fake}\,e}) + \rho_\gamma * \tau_\gamma * N_{\mathrm{C}_\gamma}^{\mathrm{fake}\,\gamma}, \\
N_{\mathrm{D}_e}^{\mathrm{exp.}} &= N_{\mathrm{D}_e}^{\mathrm{MC}} + c_{\mathrm{D}_e} * (N_{\mathrm{A}}^{WW\gamma} + N_{\mathrm{A}}^{\mathrm{fake}\,\gamma}) + \rho_e * \tau_e * N_{\mathrm{C}_e}^{\mathrm{fake}\,e}.
\end{aligned} \tag{6.14}$$

Here, the signal region has contributions from both, jets misidentified as photons and as electrons. The overlap of events containing fake photons and fake electrons is not considered, as it is found to be small. As an upper limit of the overlap, the minimum of the number of expected fake photon or fake electrons events can be used, as it is the maximal number of events that could contain two fake objects. The signal leakage is also used to estimate the contribution of fake photon events in the electron control regions, as the electrons in the events are expected to be genuine under the assumption of no overlap of events containing fake objects. Therefore, their leakage in the other regions should be similar to the one of the signal events. The same is done for the contribution of events containing fake electrons in the control regions defined for the estimation of fake photons. A sketch of the combined method is shown in Figure 6.11. All seven regions with different selection criteria are shown along with the distributions of signal events and of events from misidentified jets. Other backgrounds are omitted for clarity.

The likelihood formulation can again be employed to build a model of the combined ABCD method. To this end, the sets of observables of the two methods are combined, such that $\boldsymbol{\Omega} = \{N_{\mathrm{A}}^{WW\gamma},\ N_{\mathrm{A}}^{\mathrm{fake}\,\gamma},\ N_{\mathrm{A}}^{\mathrm{fake}\,e},\ N_{\mathrm{C}_\gamma}^{\mathrm{fake}\,\gamma},\ N_{\mathrm{C}_e}^{\mathrm{fake}\,e},\ \tau_\gamma,\ \tau_e\}$. Similarly, the set of constrained parameters, $\boldsymbol{\mathcal{C}}$, is defined to include all input parameters obtained from Monte Carlo simulation. This also comprises the efficiency of the trigger in the fake electron control regions C and D, $\epsilon_{\mathrm{C}_e}^{\mathrm{trig.}}$ and $\epsilon_{\mathrm{D}_e}^{\mathrm{trig.}}$. As it slightly varies for isolated and non-isolated electrons in the fake electron control regions C and D, it is considered as an additional source of systematic uncertainty. For the estimation of fake photons, no such effect is observed and therefore it is not considered in the likelihood function. The likelihood function of the combined model reads:

$$\begin{aligned}
\mathcal{L}(N_k|\boldsymbol{\Omega},\boldsymbol{\mathcal{C}}) = Gauss(\rho_\gamma^{\mathrm{obs.}}) \cdot Gauss(\rho_e^{\mathrm{obs.}}) \cdot Gauss(\epsilon_{\mathrm{C}_e}^{\mathrm{trig.,\ obs.}}) \cdot Gauss(\epsilon_{\mathrm{D}_e}^{\mathrm{trig.,\ obs}}) \cdot \\
\prod_{k=1}^{7} Pois(N_k; N_k^{\mathrm{exp.}}) \cdot Gauss(N_k^{\mathrm{MC,\ obs.}}) \cdot Gauss(c_k^{\mathrm{obs.}}),
\end{aligned} \tag{6.15}$$

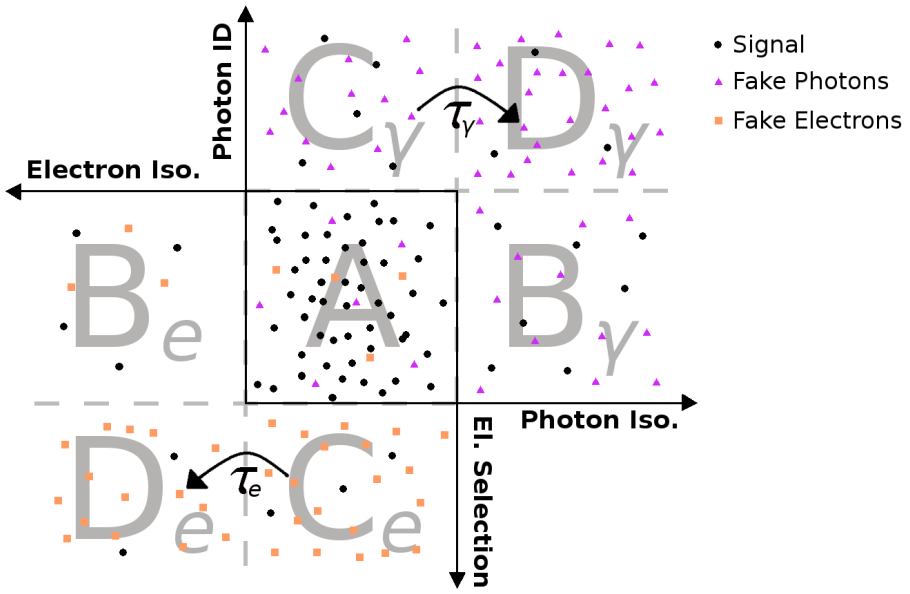

Figure 6.11: Sketch of the combination of the two ABCD methods. Region A coincides for both ABCD methods, such that contributions from jets misidentified as electrons and as photons are expected. For clarity, contributions from other backgrounds that are estimated using Monte Carlo simulation are not shown. The transfer factors τ_γ and τ_e relate the number of events containing fake photons and fake electrons respectively.

where $k \in \{$ A, B_γ, B_e, C_γ, C_e, D_γ, $\mathrm{D}_e\}$ and again $Gauss(c_{\mathrm{A}}^{\mathrm{obs.}}) = 1$.

The likelihood of the signal is determined by numerically maximising Equation (6.15) given the observed number of events in all regions. When doing this, all event counts N entering the likelihood function are restricted to positive values, as negative numbers of events are unphysical. The uncertainties on the observables are estimated using the MINOS algorithm [98], that computes confidence intervals by examining the likelihood in the interval in question. MINOS has the advantage of taking non-linearities and parameter correlations into account and it is included in the ROOT framework.

For the maximisation of the likelihood, usually the natural logarithm of the likelihood function is considered, as this turns the product in e.g. Equation 6.15 into a sum, which is easier to maximise computationally. The parameter values maximising the likelihood are commonly denoted with a hat, such that in the present case, the likelihood of the signal is maximal for the parameters $\hat{\boldsymbol{\Omega}}$ and $\hat{\boldsymbol{\mathcal{C}}}$. The uncertainty σ_μ of a parameter μ is defined as the net change of the value of the best fit parameter, $\hat{\mu}$, when the logarithm of the likelihood function increases by 0.5:

$$\sigma_\mu = |\mu' - \hat{\mu}|, \tag{6.16}$$

where μ' fulfils:

$$0.5 = \ln \mathcal{L}(\hat{\mu}) - \ln \mathcal{L}(\mu'). \tag{6.17}$$

Two possible values for μ' can be found as $\hat{\mu}$ maximises the likelihood, corresponding to the upper and lower uncertainty of $\hat{\mu}$.

The estimation of the uncertainties using the MINOS algorithm extends this concept to cases where the likelihood function depends on several parameters $(\mu, \vec{\nu})$. To this end, the

parameter in question, μ, is varied individually and all other parameters, $\vec{\nu}$, are reoptimised for each assumed value of μ. Again, the condition

$$0.5 = \ln \mathcal{L}(\hat{\mu}, \hat{\vec{\nu}}) - \ln \mathcal{L}(\mu', \hat{\hat{\vec{\nu}}}) \tag{6.18}$$

needs to be met, where the variables denoted with $\hat{\hat{\vec{\nu}}}$ correspond to the reoptimised parameters for $\mu = \mu'$. As before, two values for μ' can be found and the uncertainty intervals do not need to be symmetric, i.e. $|\mu'_{\text{up}} - \hat{\mu}| \neq |\mu'_{\text{down}} - \hat{\mu}|$.

6.3.5 Systematic Uncertainties

Several sources of systematic uncertainties exist for the signal estimation with the ABCD method and have to be taken into account. They are incorporated into the likelihood formulation as nuisance parameters constrained by a Gaussian distribution and their effect on the signal estimation is evaluated the following way: Each parameter is fixed individually to its central value plus one standard deviation. Then the likelihood is remaximised and the deviation from the initial result is computed. The same is done for the value lowered by one standard deviation and the largest of the two deviations is considered as the systematic uncertainty due to the respective source. The systematic uncertainties considered for the ABCD method are:

- Uncertainty of the Monte Carlo prediction: The precision of the Monte Carlo input parameters N_i^{MC} and c_i is limited due to the finite statistics of the simulated events. For the number of background events also the systematic uncertainty is taken into account, as explained in Section 6.1. In the ratios of expected events from Monte Carlo this uncertainty cancels. This is why it is not considered for c_i. The standard deviation of the Gaussian distribution constraining each of these input parameters is set to the uncertainty of the parameter estimation.

- Non-factorisation of the distributions: As described above, the correlation factor ρ is introduced to correct for the possible bias of the events of the estimated background with respect to the observables used for the control region definition. The deviation of the results obtained with $\rho = 1$ from those with the value of ρ set to the number obtained from Monte Carlo simulation is therefore a measure for the influence of the non-factorisation of the distributions on the final result. To this end, the value of ρ is set to unity and the width of the Gaussian distribution constraining it is set to the maximum of the statistical uncertainty on ρ and the deviation of ρ from unity when estimated using Monte Carlo simulation. The correlation factor ρ_γ is estimated using the simulation of W boson pair production and ρ_e is computed using simulated $W\gamma$ processes in association with jets.

- Trigger related uncertainty: For the fake electron estimation, the trigger efficiency, $\epsilon^{\text{trig.}}$, is slightly different in region C and region D as described in 6.3.3. This is corrected for by scaling the number of events in the two regions such that the efficiencies agree. The statistical uncertainty of the efficiency estimation using Monte Carlo simulation is taken as the standard deviation of the Gaussian distribution constraining these parameters.

Observable	Fake Photon Estimation	Fake Electron Estimation
$N_{\mathrm{A}}^{\mathrm{MC}}$	11.0 ± 2.2	
$N_{\mathrm{B}}^{\mathrm{MC}}$	1.76 ± 0.53	1.11 ± 0.40
$N_{\mathrm{C}}^{\mathrm{MC}}$	0.56 ± 0.24	21.27 ± 3.40
$N_{\mathrm{D}}^{\mathrm{MC}}$	0.11 ± 0.07	1.91 ± 0.31
c_{B}	0.108 ± 0.010	0.086 ± 0.009
c_{C}	0.081 ± 0.008	0.002 ± 0.0001
c_{D}	0.011 ± 0.003	0.001 ± 0.0001
ρ	1.00 ± 0.44	1.00 ± 0.69
$\epsilon_{\mathrm{C}}^{\mathrm{trig.}}$	-	0.878 ± 0.005
$\epsilon_{\mathrm{D}}^{\mathrm{trig.}}$	-	0.811 ± 0.005

Table 6.2: Central values of the Monte Carlo input parameters of the ABCD methods for the estimation of jets misidentified as photons and as electrons along with their uncertainty. The uncertainty corresponds to the uncertainty due to the input parameter estimation. For the correlation parameter ρ, the maximum of the statistical uncertainty and the deviation from unity is quoted. The observable $\epsilon^{\mathrm{trig.}}$ corresponds to the efficiency of the trigger to select the events. It is slightly varying for the fake electron control regions C and D, but the effect is negligible for the estimation of fake photons.

6.4 Results of the Background Estimation

The combination of the ABCD methods for fake photons and fake electrons does not only merge the data driven background estimation, but all backgrounds discussed in this chapter. This is because the Monte Carlo inputs of the ABCD methods correspond to the background estimations of the irreducible processes and the fake photons from electrons. Thus, the different background estimation methods are combined in the likelihood function of Equation (6.15).

The Monte Carlo input parameters of the full likelihood function are listed in Table 6.2 along with their uncertainties. The quoted uncertainty corresponds to the uncertainty of the parameter estimation as described in Section 6.3.5. For the correlation parameters, the maximum of the statistical uncertainty and the deviation from $\rho = 1$ is quoted, in order to estimate the effect due to the non-factorisation of the control region distributions. Both values are comparable, such that the Monte Carlo expectations agree with the statement that no bias is introduced by the selection criteria. Still, the limited statistics of the samples give rise to sizeable statistical uncertainties on ρ. The trigger efficiency $\epsilon^{\mathrm{trig.}}$ is only varying for the electron control regions C and D. Therefore, it is not quoted for the estimation of fake photons.

The Monte Carlo input parameters in region B are comparable for the photon and electron estimation. They do differ in regions C and D, as these regions are defined quite differently for the estimation of fake photons and fake electrons.

The event count observed in the seven regions defined by the ABCD method is given in Table 6.3. The quoted uncertainty corresponds to the statistical uncertainty of the measurement, which is the square root of the actual value. Comparing Tables 6.2 and 6.3 it becomes evident that the event count observed in region B_e is below the expectation from $N_{\mathrm{B}}^{\mathrm{MC}}$ only. The likelihood formulation of the ABCD method is capable of accounting for this fluctuation.

With these inputs, the maximisation of the likelihood function given in Equation (6.15)

Observable	Fake Photon Estimation	Fake Electron Estimation
$N_{\mathrm{A}}^{\mathrm{obs.}}$	26 ± 5	
$N_{\mathrm{B}}^{\mathrm{obs.}}$	7 ± 3	1 ± 1
$N_{\mathrm{C}}^{\mathrm{obs.}}$	8 ± 3	95 ± 10
$N_{\mathrm{D}}^{\mathrm{obs.}}$	13 ± 4	122 ± 11

Table 6.3: Observed number of events in the different regions defined by the ABCD method. The uncertainty quoted corresponds to the statistical uncertainty of the measurement.

yields for the observables:

$$\begin{aligned} N_{\mathrm{A}}^{WW\gamma} &= 11.6^{+6.2}_{-6.2}, \\ N_{\mathrm{A}}^{\mathrm{fake}\,\gamma} &= 2.0^{+3.4}_{-1.4}, \\ N_{\mathrm{C}}^{\mathrm{fake}\,\gamma} &= 6.5^{+3.3}_{-2.6}, \\ \tau_{\gamma} &= 2.0^{+2.6}_{-1.0}, \\ N_{\mathrm{A}}^{\mathrm{fake}\,e} &= 0.0^{+0.6}_{-0.0}, \\ N_{\mathrm{C}}^{\mathrm{fake}\,e} &= 62.1^{+9.5}_{-9.0}, \\ \tau_{e} &= 1.8^{+0.0}_{-0.9}. \end{aligned}$$

The best fit values are quoted along with their combined statistical and systematic uncertainties obtained using the MINOS algorithm. The signal can only be extracted with a large statistical significance, but it is different from the null hypothesis within 1.87 standard deviations.

The uncertainty on the extracted number of signal events can be split into a statistical and a systematic component. This yields

$$N_{\mathrm{A}}^{WW\gamma} = 11.6 \pm 5.7(\mathrm{stat.}) \pm 2.4(\mathrm{syst.}),$$

where the largest contribution comes from the limited statistics of the observed events in the different ABCD regions. This component amounts to a relative uncertainty of 49 % and dominates the uncertainties of this analysis. The systematic uncertainty can be split into the different sources explained in Section 6.3.5 and the values are given in Appendix A.4. The largest source of systematic uncertainty is the uncertainty of the Monte Carlo expectation of background events in the signal region, amounting to 21.9 %. The second largest uncertainty arises from the correction factor of the fake photon estimation ρ_{γ}. When this value is changed within its uncertainties, the impact on the extracted number of signal events is 8.4 %. Still, all systematic components are much lower than the statistical one.

The maximal value of the likelihood is obtained, when no fake electron event is present in the signal region due to the downwards fluctuation in region B_e. The value zero is obtained due to the definition of the likelihood function, which imposes a lower boundary of zero on all event counts, as negative event counts are unphysical. This has no influence on any other quantity but on the expected number of fake electrons events. For this observable, the best fit value corresponds to its lower bound. Removing the boundary on $N_{\mathrm{A}}^{\mathrm{fake}\,e}$ yields a best fit value of $N_{\mathrm{A}}^{\mathrm{fake}\,e} = -0.8^{+0.9}_{-1.3}$ which is negative, but still compatible with zero. The other observables vary a bit when removing the boundary on $N_{\mathrm{A}}^{\mathrm{fake}\,e}$, but the change is well within one standard deviation. As the number of events containing jets misidentified as electrons is zero, no overlap

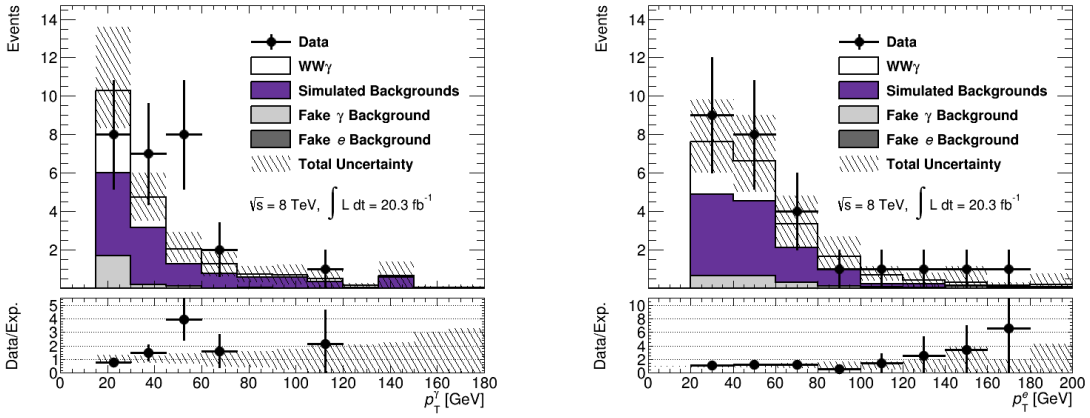

(a) **(b)**

Figure 6.12: Distribution of transverse momentum for photons (a) and electrons (b) passing the event selection requirements. The round markers show the observed number of events in the studied data set. The p_{T}-distributions are taken from simulation for the different background processes and scaled to the best fit values from the likelihood maximisation. The fake electron background is not visible, as its best fit value corresponds to zero. The lower panels show the ratio of the observed event count and the total expectations.

between events containing misidentified jets as photons and as electrons is observed and the assumption that the overlap is small is confirmed.

A table containing the best fit values for all variables in the likelihood function of Equation 6.15 is given in Appendix A.4 along with their initial values. For all constrained parameters, the best fit value basically corresponds to the input value of the variable. More tension is observed for the event counts in the regions defined for the estimation of jets being misidentified as electrons. While the likelihood of the signal is maximal for a higher number of events than observed in region B_e, it prefers lower values of N_{C_e} and N_{D_e} than measured.

The comparison of the background estimation to the distributions measured in data is shown in Figure 6.12. The transverse momentum distribution of the photon is shown on the left and the one for electrons on the right. The measured data is represented by the round markers and the signal and background expectations are shown as stacked histograms. The distributions are taken from Monte Carlo simulation and the signal yield is scaled to match the next-to-leading order computations from the generator VBFNLO. The background components are scaled to the expectations obtained from the combined ABCD method, resulting in a zero fake electron events. The p_{T}-distribution from the background components estimated with Monte Carlo simulation described in Sections 6.1 and 6.2 are added according to their relative contributions. This component also includes the small contribution of the fake muon background, which is taken from simulation. The shape of the p_{T}-distribution of the fake photon background is taken from the simulation of WW processes and top-antitop production. The hatched band represents the combined statistical and systematic uncertainty on the background estimation. The lower panel of each figure shows the ratio of observed event counts divided by the total number of expected events corresponding to the stacked histogram in the upper panel. A good agreement between the expected distributions and the data is observed with a slight underestimation of the observation, but all is well within the quoted uncertainties.

The combined backgrounds estimation yields the most likely value for the number of signal events. This can be used to describe the production of $WW\gamma$ events by computing the production cross-section of the $e\mu\gamma$ final states as discussed in the following chapter.

7 Cross-Section Computation

The study of $e\mu\gamma$ final states can be quantified by computing the production cross-section of the process. It is defined as the ratio of the number of signal events and the integrated luminosity of the data set:

$$\sigma^{e\mu\gamma} = \frac{N^{e\mu\gamma}}{\mathrm{L}_{\mathrm{int.}}}. \tag{7.1}$$

As the detector does not have full geometrical coverage, only a fraction of events is observable and the event selection criteria impose further restrictions on the number of measured events. Therefore, the measured cross-section does not correspond to the total cross-section, but to a fiducial one, which means that it imposes restrictions on the phase space. These are partly corrected for by the correction factor ε, which is discussed in Section 7.1. In the notation of the previous chapter, the number of extracted signal events is denoted $N_{\mathrm{A}}^{WW\gamma}$, and the fiducial cross-section is defined as:

$$\sigma_{\mathrm{fid.}}^{e\mu\gamma} = \frac{N_{\mathrm{A}}^{WW\gamma}}{\varepsilon \cdot \mathrm{L}_{\mathrm{int.}}}. \tag{7.2}$$

The extraction of this quantity is discussed along with the theoretical expectations in this chapter.

7.1 Fiducial Phase Space and its Corrections

The analysis is carried out in the fiducial region, which means that geometrical and kinematic requirements are imposed on the final state objects as described in Chapters 4 and 5. In order to obtain a theoretically well defined quantity, the fiducial phase space is defined based on requirements on the truth record of the event. The so-called particle level is considered here, where the truth record of the event is examined after the showering step of the simulation. The fiducial phase space is defined similar to the event selection criteria and summarised in Table 7.1. The requirements on the transverse momenta and energies of the objects on particle level are the same as imposed in the event selection on the so-called reconstruction level. Only the requirements on the pseudorapitidy are slightly extended, as the reconstruction level selection is motivated by the detector geometry. The restrictions of electromagnetic objects in the region of transition between the barrel and the end caps of the calorimeter is not employed for the definition of the fiducial phase space and the maximal η-value for leptons is slightly extended to 2.5. The isolation criteria of the photons at the particle level is imposed by using the relative isolation fraction ϵ_h^p [101] which is better suited for particle level calculations. It is defined as the sum of energies of the particles in a cone with $R = 0.4$ around the photon divided by the transverse energy of the photon: $\epsilon_h^p = {E_{\mathrm{T}}^{\mathrm{iso},\gamma}}/{E_{\mathrm{T}}^{\gamma}}$. This way, an infrared safe definition of the cross-section is obtained.

The difference of the event selection on reconstruction and on particle level is expressed by the correction factor ε. It is a measure for the inefficiencies associated with the reconstruction algorithms and the slightly changed geometrical acceptance. The correction factor is defined

	$pp \to e\nu\mu\nu\gamma$
W bosons	1 electron and 1 muon with opposite el. charge $p_T^{el,\mu} > 20\,\text{GeV}$ $\lvert\eta^l\rvert < 2.5$ $\Delta R(\text{lepton}, \text{lepton}) > 0.1$
Photon	≥ 1 photon $E_T^\gamma > 15\,\text{GeV}$ iso. fraction $\epsilon_h^p < 0.5$ $\lvert\eta^\gamma\rvert < 2.37$ $\Delta R(\text{lepton}, \gamma) > 0.5$
Jets	$p_T > 25\,\text{GeV}$ $\lvert y\rvert < 4.4$ $\Delta R(\text{jet}, \gamma) > 0.5$ $\Delta R(\text{jet}, \text{lepton}) > 0.3$
Background suppression	$m_{ll} > 50\,\text{GeV}$ $E_{\text{T, rel}}^{\text{miss}} > 15\,\text{GeV}$ no selected jet in the event no additional lepton with $p_\text{T} > 7\,\text{GeV}$ in the event

Table 7.1: Requirements for the fiducial region based objects defined on particle level.

as the number of events selected by the event selection based on the reconstructed objects, N_reco, divided by the event count obtained from the truth record of the event, N_truth:

$$\varepsilon = \frac{N_\text{reco}}{N_\text{truth}}. \tag{7.3}$$

The correction factor ε is computed using the Monte Carlo simulation of the SHERPA generator of the signal and corresponds to:

$$\varepsilon = 0.303 \pm 0.008(\text{stat.}) \pm 0.019(\text{syst.}).$$

This indicates, that about 30 % of all simulated $e\mu\gamma$ events are reconstructed. The main source of inefficiency is due to the electron and photon identification criteria whose efficiency range below 70 % for certain phase space regions (see Figure 4.2). As three objects are required for the selected events, the respective efficiencies multiply. Furthermore, the fiducial phase space definition is slightly larger than the one used for the reconstructed events, which also lowers the correction factor. This effect can be investigated separately by defining a second set of selection criteria based on the truth record of the event. It imposes all requirements listed in Table 7.1, but restricts the η-region of the objects further, such that they correspond to the ones used for the reconstructed objects. Explicitly, this means that particle level electrons and photons are rejected if they are in the region $1.37 < |\eta| < 1.52$. The electrons are only considered if their pseudorapitidy is below 2.47, and particle level muons if $|\eta| < 2.4$. Therefore, this set of requirements is also called restricted fiducial region. Using this phase space, the correction factor can be split into the acceptance A, that is a measure for the inefficiency due to the geometrical restrictions in pseudorapitidy and the reconstruction efficiency C:

$$\varepsilon = A \times C = \frac{N_\text{reco}}{N_\text{res. fid.}} \times \frac{N_\text{res. fid.}}{N_\text{truth}}, \tag{7.4}$$

where $N_{\text{res. fid.}}$ is the number of events selected by the restricted fiducial event selection criteria on particle level. The efficiency associated with the detector acceptance is $(87.0 \pm 0.5(\text{stat.}))\,\%$ and describes to the loss of objects due to the restrictions in pseudorapitidy between the fiducial phase space and the event selection based on reconstructed events. A larger inefficiency arises from the reconstruction of the objects and is expressed by C which amounts to $(0.348 \pm 0.009(\text{stat.}))$. This value is low, as three objects are required in the final state and each object has an associated reconstruction efficiency as described in Chapter 4.

7.1.1 Statistical Uncertainty of the Correction Factor

Special care has to be taken when computing the statistical uncertainty of the correction factor as the events in the numerator and denominator are correlated. The event counts of the signal region and the fiducial region are obtained using the same set of simulated events and therefore, standard error propagation does not apply. Splitting the event counts in correlated and uncorrelated components can account for this effect, but is not applicable in this case, as the Monte Carlo events have different weights attributed to them depending on the selection applied. This is because the reconstructed events have additional corrections that are not needed for the particle level event counts. The bootstrap method [102, 103] can be used to overcome this difficulty. It is a statistical method based on random sampling with replacement and relies on the fact that the resampled data has the same statistical features as the original data set. Thus, the uncertainties of the sample can be estimated by resampling the initial data.

Technically this is realised by evaluating N_{reco} and N_{truth} ten thousand times, based on the same Monte Carlo input sample. Therefore, each time an event passes all criteria of a certain category, ten thousand values are drawn from a Poissoninan distribution with mean one. The numbers are treated as different measurements of the event count and each have the same Monte Carlo weight attributed to them. This way ten thousand measurements of the observables are simulated. The correlation between the different event selections is introduced by using the same sequence of Poissonian event counts for both categories when one event passes the selection criteria of either category. The mean of the Poissonian is chosen to be one, as this is the expected event count for the observation of the event per construction. The correction factor can then be computed for the simulated event counts and the distribution of ε follows a Gaussian curve whose standard deviation corresponds to the uncertainty due to the limited sample statistics. This is shown in Figure 7.1 where a Gaussian curve is fitted to the distribution of the correction factor and the fit parameters are indicated. In practise, the distribution is not fitted, but the root mean square (RMS) deviation from the mean value is used. It is also given in the figure and agrees with the standard deviation from the fit.

7.1.2 Systematic Uncertainty of the Correction Factor

The systematic uncertainty on the correction factor estimation corresponds to the uncertainties attributed to the Monte Carlo simulation. They include uncertainties due to the calibration and resolution of the different subdetectors and the reconstruction efficiencies of the single objects as described in Chapter 4. The different components of systematic uncertainties are assessed by varying the object's attributes individually within their uncertainty for each event as described in Section 6.1.1. The maximum deviation of the correction factor computed from the systematically varied sample from the nominal value is taken as symmetric systematic uncertainty associated with the specific component: $\sigma^{\varepsilon}_{\text{syst.}} = max(\sigma^{\varepsilon}_{\text{up}}, \sigma^{\varepsilon}_{\text{down}})$. All components

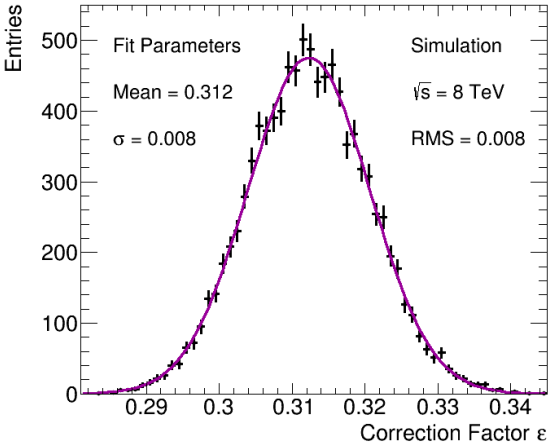

Figure 7.1: Distribution of the correction factor computed ten thousand times using resampled event counts as inputs. The distribution is fitted by a Gaussian curve whose mean corresponds to the central value of the correction factor and the standard value corresponds to the statistical uncertainty of ε. Also given is the root mean square (RMS) of the distribution which coincides with the standard deviation from the fit.

of systematic uncertainties considered for the correction factor of this analysis are summarised in Table 7.2 along with the central value of ε.

The uncertainty that arises due to the choice of the generator is assessed by computing the correction factor from the signal sample where the generator MadGraph is used for the computation of the hard scattering and the program Pythia is used for the showering of the partons. The CTEQ6 parton density function is used in the simulation, such that the two signal samples are not generated on the same footing. Therefore, event weights based on the momentum fraction x of the two incoming partons are computed to mitigate the difference in parton density function. This way, the MadGraph signal simulation is reweighted to the CT10 parton density function, such that the correction factors computed using the two different samples are comparable. The uncertainty due to the choice of the parton density function is attributed to the theory prediction and thus omitted here in order to avoid double counting. The computation of the correction factor using the MadGraph signal simulation yields a slightly smaller correction factor of $\varepsilon_{\mathrm{MG}} = (0.289 \pm 0.006\ (\mathrm{stat.}))$. Its deviation from the nominal value is taken as an additional source of systematic uncertainty. A small difference between the values of the two samples is expected, as both are generated at leading order, but the SHERPA simulation allows up to one additional parton in the final state, which the MadGraph simulation does not.

The single components of the systematic uncertainties are added in quadrature and yield an overall uncertainty of 6.4 %. The largest contributions stem from the difference between the samples generated with the MadGraph and SHERPA generators and the uncertainty associated with the jet energy.

Correction Factor ε	0.303 ± 0.008(stat.)
Systematic Component	Relative systematic uncertainty [%]
Electromagnetic Energy Scale	1.5
Electron Energy Resolution	0.2
Electron Efficiency	1.0
Jet Energy Resolution	1.9
Jet Energy Scale	3.2
Jet Vertex Fraction	0.3
$E_{\mathrm{T}}^{\mathrm{miss}}$ Energy Scale Soft Terms	0.2
$E_{\mathrm{T}}^{\mathrm{miss}}$ Resolution Soft Terms	0.6
Muon Energy Scale	0.0
Muon Efficiency	0.2
Muon Resolution Inner Detector	0.0
Muon Resolution Muon System	0.1
Photon Energy Resolution	0.4
Photon Efficiency	1.3
Pile Up	0.2
Generator Dependence	4.6
Total	6.4

Table 7.2: Correction factor for the simulation of the $WW\gamma$ signal using SHERPA along with the relative systematic uncertainties. The generator dependence indicates the difference between the SHERPA and the MadGraph simulation.

7.2 Cross-Section Extraction

The production cross-section of $e\mu\gamma$ final states can be computed using:

- The expected number of signal events: $N_{\mathrm{A}}^{WW\gamma} = 11.6 \pm 5.7(\mathrm{stat.}) \pm 2.4(\mathrm{syst.})$.
- The correction factor: $\varepsilon = 0.303 \pm 0.008(\mathrm{stat.}) \pm 0.019(\mathrm{syst.})$.
- The integrated luminosity of the data set: $\mathrm{L_{int.}} = (20.3 \pm 0.6)\,\mathrm{fb}^{-1}$.

Putting this in Equation (7.2) results in:

$$\sigma_{\mathrm{fid.}}^{e\mu\gamma} = (1.89 \pm 0.93(\mathrm{stat.}) \pm 0.41(\mathrm{syst.}) \pm 0.05(\mathrm{lumi.}))\,\mathrm{fb},$$

where the largest contribution comes from the low statistics of observed number of events, as this is also the largest source of uncertainty when extracting the number of signal events. The result has little statistical power as is compatible with zero within its two-sigma interval. A larger data set would be necessary in order to improve the significance. Yet, this is the first study of the fully leptonic $WW\gamma$ process at a hadron collider.

7.3 Theoretical Expectations

The theoretical expectation of the production cross-section of $WW\gamma$ processes at the LHC is computed using the Monte Carlo program VBFNLO, as it computes the value at next-to

leading order in the strong coupling constant. The exact input parameters for steering the program are given in Appendix A.5 and mainly correspond to the standard values employed by the generator. The generator does not allow to compute the cross-section of $e\mu\gamma$ final states only, but computes the expectations for the decay into any pair of light leptons. The Standard Model is based on the assumption of lepton universality, which means that the coupling is flavour independent. Therefore, the cross-section of $e\mu\gamma$ final states can be obtained easily by dividing the cross-section for any $WW\gamma$ final state containing light leptons by two. This is because two of the four possible final states containing light leptons contain opposite flavour pairs. The possible final states with light leptons are $ee\gamma$, $e\mu\gamma$, $\mu\mu\gamma$ and $\mu e\gamma$, where the position of the lepton depends on the W boson it is originating from. The expected cross-section amounts to

$$\sigma_{\text{fid.}}^{\text{NLO}} = (1.81 \pm 0.08)\,\text{fb},$$

where three different sources of uncertainty are considered: The uncertainty due to the choice of the parton distribution as well as the choice of the renormalisation and the factorisation scale. The CT10 parton density function is used for the computation of the central value. In order to assess the impact of this choice, the value is recomputed using the MSTW2008 parton distribution function and a deviation of 0.6 % is observed. The renormalisation and the factorisation scales are nominally set to the invariant mass of the triboson final state and varied by a factor of two in order to assess their uncertainties. The variation of the scales changes the nominal cross-section by maximally 2.9 %. This amounts to an overall systematic uncertainty of 3.0 %, dominated by the scale uncertainties.

7.4 Comparison of Measurement and Theory

The measured value of the cross-section and the theoretical expectation obtained in Section 7.3 are not obtained on the same footing. This is because the theory computation is performed at the so-called parton level, where single partons are accounted for and quarks and gluons are considered as jets. This is opposed to the particle level measurement performed in Section 7.2 where the objects are considered after the parton showering. The difference between the parton and particle level expectations is corrected for by the parton to particle level correction factor $C^{parton \to particle}$, which is the ratio of events selected at particle level, N_{truth} and at parton level, N_{parton}:

$$C^{parton \to particle} = \frac{N_{\text{truth}}}{N_{\text{parton}}}.$$

The theory expectation at particle level, and thus comparable to the measurement, can be obtained according to:

$$\sigma_{\text{fid.}}^{\text{theory}} = C^{parton \to particle} \times \sigma_{\text{fid.}}^{\text{NLO}}.$$

The event selection criteria for the particle and the parton level event selection are the same and given in Table 7.1, but they are based on different objects. As the name implies, the parton level event selection is based on the single partons that are produced by the generator, while the particle level definition relies on the object after the parton shower. The largest difference lies in the jet definition where clustered objects are considered at particle level as opposed to single partons. This has an effect on both the direction and transverse momentum of the jet, which is why the number of jets on particle and parton level can differ. But also the relative photon isolation fraction ϵ_h^p is affected, as it is based on the energy of objects close to

the photon. For the definition of leptons on particle level their four momenta are corrected by adding back the photons radiated during the shower in order to obtain comparable quantities at parton and particle level. This effect is found to be small.

The correction factor is computed by using the simulation of the signal obtained from the SHERPA generator. It amounts to:

$$C^{parton \to particle} = 1.10 \pm 0.01(\text{stat.}),$$

thus raising the parton level expectations by ten percent. The difference comes mainly from the different jet definitions at parton and particle level, while only a small dependence on the leptons or the photon isolation is found. The dependence of the parton to particle level correction factor on the shower modelling can be tested by computing it using the signal simulation of MadGraph. The result is $C^{parton \to particle} = 1.10 \pm 0.01(\text{stat.})$, i.e. exactly the same value as for the SHERPA simulation. Therefore, no additional systematic uncertainty is introduced due to the generator dependence.

The theoretical cross-section expectation for the production of $e\mu\gamma$ final states on particle level amounts to:

$$\sigma_{\text{fid.}}^{\text{theory}} = (1.99 \pm 0.09)\,\text{fb}$$

and agrees with the measured cross-section of $\sigma_{\text{fid.}}^{e\mu\gamma} = (1.89 \pm 1.00)\,\text{fb}$. Even though the data set with the largest statistics recorded by the ATLAS detector is employed, the statistical uncertainty of the experimental result is large and prevents the analysis from claiming the observation of the signal. Yet, no deviations from the Standard Model expectations are observed such that this analysis can be used to set limits on the occurrence of physics not described by this model. This is the subject of the following chapter.

8 Constraints on Anomalous Quartic Gauge Couplings

The analysis of $e\mu\gamma$ final states can be used to constrain extensions of the Standard Model of particle physics, as no significant deviation of the measurement from the Standard Model expectations are observed. The limits are derived in the framework of anomalous quartic gauge couplings presented in Section 1.4. Frequentist limits at 95 % confidence level are computed using a profile likelihood method. In this chapter the statistical method with which the limits are derived is presented. This is followed by the description of the optimisation of the phase space to obtain competitive limits and the discussion of the results themselves. In Section 8.3.1 non-unitarised limits are presented and in Section 8.3.2 a dipole form factor is employed to obtained unitarised results.

8.1 Limit Setting Procedure

Constraints on anomalous quartic gauge couplings are derived by computing the maximal number of events that agree with the observation taking the experimental uncertainties into account. Each coupling f_i/Λ^4 (described in Section 1.4) is varied independently and the minimal value at which the increased event count due to this coupling can be excluded with a confidence level of 95 % is quoted as the limit on the respective coupling. The individual variation of single couplings is justified, as new physics processes might only give rise to certain anomalous couplings and not enhance all 14 possible operators detailed in Appendix A.2. Furthermore, it is technically challenging to scan a 14-dimensional parameter space and therefore, the couplings are examined individually.

The cross-section of the $WW\gamma$ process and thus the expected number of events can be expressed as a parabolic function depending on the coupling f_i/Λ^4 as these quantities are proportional to the square of the Lagrangian of the theory. This can be seen by squaring the effective Lagrangian from Equation (1.2) and setting all couplings but one to zero:

$$\sigma_{\text{fid.}}^{\text{aQGC}}(\frac{f_i}{\Lambda^4}) \sim (\mathcal{L}_{eff})^2 = (\mathcal{L}_{SM} + \frac{f_i}{\Lambda^4}\mathcal{O}_i)^2 = (\mathcal{L}_{SM})^2 + (\mathcal{L}_{SM}\frac{f_i}{\Lambda^4}\mathcal{O}_i) + (\frac{f_i}{\Lambda^4}\mathcal{O}_i)^2. \tag{8.1}$$

The above relation allows for efficient modelling of the contributions from anomalous couplings, as the parabola can be obtained by computing the expected cross-section for three values of f_i/Λ^4 and fitting it with the second order polynomial:

$$\sigma_{\text{fid.}}^{\text{aQGC}}(\frac{f_i}{\Lambda^4}) = p_0 + p_1 \cdot (\frac{f_i}{\Lambda^4}) + p_2 \cdot (\frac{f_i}{\Lambda^4})^2. \tag{8.2}$$

This is computationally more effective than recomputing the cross-section for a fine scan of the parameter space of f_i/Λ^4. The Standard Model Lagrangian is obtained in case $f_i/\Lambda^4 = 0$, which implies that p_0 corresponds to the Standard Model cross-section.

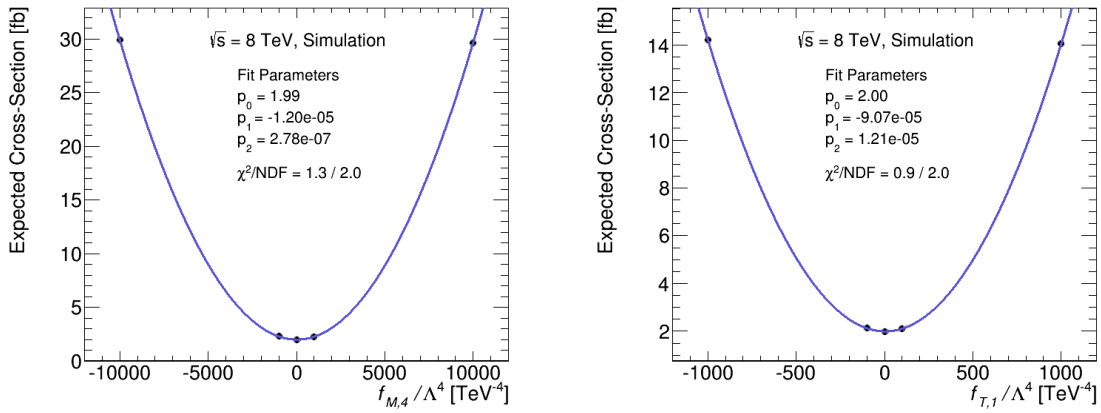

(a) **(b)**

Figure 8.1: Expected cross-section as a function of the couplings $f_{M,4}/\Lambda^4$ (a) and $f_{T,1}/\Lambda^4$ (b). The black markers indicate the cross-section computed with the VBFNLO program for five different values of the coupling and multiplied with the parton to particle level correction factor. The solid line shows the parabolic fit, whose parameters are indicated along with the value of χ^2/NDF.

In this analysis the cross-section of five points in the f_i/Λ^4 parameter space is computed using the VBFNLO program and fitted by a parabolic function for each coupling. This is shown for two examples of couplings in Figure 8.1. A good agreement between the simulated points and the fit can be observed and is indicated by a low value of χ^2/NDF.

The expected event yield due to the anomalous quartic gauge couplings can be computed by combining Equations (7.2) and (8.2) as well as the parton to particle level correction:

$$N^{\text{aQGC}}(\frac{f_i}{\Lambda^4}) = C^{parton \to particle} \cdot \varepsilon \cdot \text{L}_{\text{int.}} \cdot \left(p_0 + p_1 \cdot (\frac{f_i}{\Lambda^4}) + p_2 \cdot (\frac{f_i}{\Lambda^4})^2 \right). \tag{8.3}$$

This is considered as the signal in the following discussion.

The likelihood of observing $N^{\text{obs.}}$ events in data is given by the Poisson distribution of the sum of the expected number of events from the anomalous quartic gauge coupling and the background events:

$$\mathcal{L}(N^{\text{obs.}}) = Pois(N^{\text{obs.}}; N^{\text{aQGC}} + N^{\text{bg.}}) \tag{8.4}$$

and as N^{aQGC} depends on the anomalous coupling f_i/Λ^4, so does the likelihood:

$$\mathcal{L}(N^{\text{obs.}}|\frac{f_i}{\Lambda^4}) = Pois(N^{\text{obs.}}; N^{\text{aQGC}}(\frac{f_i}{\Lambda^4}) + N^{\text{bg.}}). \tag{8.5}$$

The number of signal and background events are not exactly known, but associated with uncertainties as discussed in the previous chapters. These uncertainties are called σ^{aQGC} and $\sigma^{\text{bg.}}$ in this discussion and they are incorporated in the likelihood formalism using nuisance parameters $\boldsymbol{\theta} = \{\theta^{\text{aQGC}}, \theta^{\text{bg.}}\}$; where the first parameter is associated with the signal and the second is associated with the background. The nuisance parameters are nominally zero, but float during the likelihood maximisation within a normal distribution with unit width. In order to express the event yields as a function of their respective total uncertainties, the event counts can be rewritten as:

$$\begin{aligned} N^{\text{aQGC}}(\boldsymbol{\theta}) &= N^{\text{aQGC}}(1 + \sigma^{\text{aQGC}}\theta^{\text{aQGC}}), \\ N^{\text{bg.}}(\boldsymbol{\theta}) &= N^{\text{bg.}}(1 + \sigma^{\text{bg.}}\theta^{\text{bg.}}), \end{aligned} \tag{8.6}$$

Some sources of uncertainty are correlated for the signal and the background events, as is the case for the uncertainty due to the luminosity in this analysis. This is incorporated in the likelihood formulation by introducing the correlation matrix C_{ij}. It is computed from k individual components of systematic uncertainty according to

$$C_{ij} = \sum_k \sigma_{ik}\sigma_{jk}, \tag{8.7}$$

where i and j are $\in \{1, 2\}$, indicating the k-th source of uncertainty on N^{aQGC} and $N^{\text{bg.}}$ respectively. Thus, $\sigma^{\text{aQGC}} = C_{11}$ and $\sigma^{\text{bg.}} = C_{22}$. This way, only two nuisance parameters need to be considered instead of $2k$. Therefore, the likelihood of the observed number of events can be rewritten as:

$$\mathcal{L}(N^{\text{obs.}}|\frac{f_i}{\Lambda^4}, \boldsymbol{\theta}) = Pois(N^{\text{obs.}}; N^{\text{aQGC}}(\frac{f_i}{\Lambda^4}, \boldsymbol{\theta}) + N^{\text{bg.}}(\boldsymbol{\theta})) \times \frac{1}{2\pi} e^{-\frac{1}{2}(\boldsymbol{\theta} C^{-1} \boldsymbol{\theta})}. \tag{8.8}$$

and the second term represents the correlated Gaussian constraint on the nuisance parameters.

The constraints on the anomalous quartic gauge couplings are derived using the so-called p-value, which corresponds to the probability of observing data of equal or greater incompatibility with the predictions of a certain hypothesis [104]. The hypothesis under test is the existence of anomalous quartic gauge couplings with a given strength f_i/Λ^4. A commonly chosen p-value for the exclusion of a signal hypothesis is 0.05 corresponding to a confidence level of 95 % and it is used in the following.

The testing of the compatibility between the hypothesis of a coupling of $f_i^{\text{test}}/\Lambda^4$ and a certain number of observed events is done by using the statistics $\lambda(N^{\text{obs.}}, \frac{f_i^{\text{test}}}{\Lambda^4})$. As λ corresponds to a probability it should fulfil $0 < \lambda(N^{\text{obs.}}, \frac{f_i^{\text{test}}}{\Lambda^4}) \leq 1$. A viable candidate for this statistics is the profile likelihood ratio. It is the ratio of the profile of the likelihood of the observation and the likelihood maximised with respect to all parameters. The profile likelihood $\mathcal{L}_p(N^{\text{obs.}}|\frac{f_i}{\Lambda^4})$ refers to the likelihood of the observation that only depends on the parameter under test. It is obtained from Equation (8.8) by computing the values $\hat{\hat{\boldsymbol{\theta}}}$ that maximise the likelihood for a given value of $\frac{f_i}{\Lambda^4}$. Thus,

$$\mathcal{L}_p(N^{\text{obs.}}|\frac{f_i}{\Lambda^4}) = \mathcal{L}(N^{\text{obs.}}|\frac{f_i}{\Lambda^4}, \hat{\hat{\boldsymbol{\theta}}}) \tag{8.9}$$

and the profile likelihood ratio can be written as:

$$\lambda(N^{\text{obs.}}, \frac{f_i}{\Lambda^4}) = \frac{\mathcal{L}_p(N^{\text{obs.}}|\frac{f_i}{\Lambda^4})}{\mathcal{L}(N^{\text{obs.}}|\frac{\hat{f}_i}{\Lambda^4}, \hat{\boldsymbol{\theta}})}, \tag{8.10}$$

where $\frac{\hat{f}_i}{\Lambda^4}$ and $\hat{\boldsymbol{\theta}}$ denote the maximum likelihood estimators, i.e. the values of $\frac{f_i}{\Lambda^4}$ and $\boldsymbol{\theta}$ that maximise the likelihood for the observation of $N^{\text{obs.}}$ events. Therefore, $\lambda(N^{\text{obs.}}, \frac{f_i}{\Lambda^4})$ is maximal for $\frac{f_i}{\Lambda^4} = \frac{\hat{f}_i}{\Lambda^4}$ by definition.

The profile likelihood ratio effectively removes the nuisance parameters from the actual testing. This is a desired feature, as they represent the uncertainty on the measured value which needs to be taken into account for the testing, but the actual value of $\boldsymbol{\theta}$ is of no interest. The impact of the uncertainty of the measurement on the likelihood ratio can be seen in Figure 8.2. It shows the double of the negative natural logarithm of the likelihood ratio as a function of anomalous quartic gauge couplings. Again, the two couplings $f_{M,4}/\Lambda^4$ and $f_{T,1}/\Lambda^4$ are chosen as

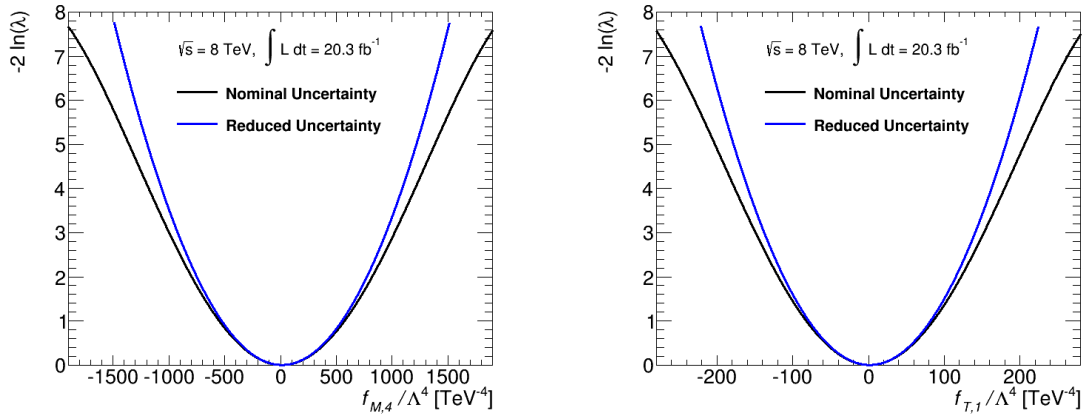

(a) **(b)**

Figure 8.2: Visualisation of the impact of the uncertainty on the measurement on the profile likelihood ratio. The double of the negative logarithm of the likelihood ratio λ is shown as function of the anomalous quartic gauge coupling $f_{M,4}/\Lambda^4$ (a) and $f_{T,1}/\Lambda^4$ (b). The black curve shows the observable when the full uncertainty used for the limit setting in Section 8.3 is employed. The uncertainty corresponds to 32.5 % on the signal and 350 % on the background estimation. The blue curve shows the observable when 1 % uncertainty is assumed on both, the signal and the background. This yields a much narrower distribution which leads to better exclusion limits.

examples. The natural logarithm is considered here, as it is computationally advantageous and commonly twice its negative value is considered. The black curve corresponds to the likelihood ratio employed for the limit setting used in Section 8.3. The uncertainties amount to 32.5 % on the signal and 350 % on the background estimation. The blue curve shows the same profile likelihood ratio, but with smaller uncertainties. They are chosen to be 1 % for both the signal and the background for illustrative purposes. The likelihood ratio with the smaller uncertainties is much narrower and thus leads to better exclusion limits. The profile likelihood ratio shows the same behaviour for both couplings.

The profile likelihood ratio can be used to test the hypothesis. An observation of N^{ps} events under the hypothesis of a certain coupling $\frac{f_i^{\text{test}}}{\Lambda^4}$ is considered less likely than the actual observation of $N^{\text{obs.}}$ events, if

$$\lambda(N^{\text{ps}}, \frac{f_i^{\text{test}}}{\Lambda^4}) < \lambda(N^{\text{obs.}}, \frac{f_i^{\text{test}}}{\Lambda^4}). \tag{8.11}$$

The p-value of a certain coupling $\frac{f_i^{\text{test}}}{\Lambda^4}$ is evaluated using the profile likelihood ratio. In the case of large expected event counts, $N^{\text{obs.}}$, Wilk's theorem [105] can be used which allows to describe the likelihood ratio by the functional form of the χ^2-distribution. In this analysis though, small event counts are expected, which is why the approximations used in the theorem do not hold. Therefore, the p-value is evaluated based on pseudo experiments. These are randomly generated values of $N^{\text{obs.}}$ that follow a Poissonian distribution with the mean $N^{\text{mean}} = N^{\text{aQGC}}(f_i^{\text{test}}/\Lambda^4) + N^{\text{bg.}}$. The values of $N^{\text{aQGC}}(f_i^{\text{test}}/\Lambda^4)$ and $N^{\text{bg.}}$ are allowed to fluctuate within their uncertainties. Technically this is achieved by randomly drawing values from the likelihood function given in Equation (8.8) that takes the nuisance parameters into account. This is done 10000 times per $\frac{f_i^{\text{test}}}{\Lambda^4}$ and the corresponding p-value is computed as the

ratio of pseudo experiments that yield an event count that is less likely than the observed one divided by the total number of pseudo experiments:

$$p\text{-value}(\frac{f_i^{\text{test}}}{\Lambda^4}) = \frac{N^{\text{ps}}(\lambda(N^{\text{ps}}, \frac{f_i^{\text{test}}}{\Lambda^4}) < \lambda(N^{\text{obs.}}, \frac{f_i^{\text{test}}}{\Lambda^4}))}{N^{\text{ps}}}. \tag{8.12}$$

This way, the p-value can be computed for any value of the anomalous coupling given the observed number of events, $N^{\text{obs.}}$. Specific values of a given coupling are excluded, if their p-value is below 5 %. The interval of non-excluded values of the coupling contains the true value with a probability of at least 95 % according to Neyman [106]. The procedure described in this reference does not specify the test that is used to obtain the p-value and the likelihood ratio intervals considered here correspond to the ones described by Feldman and Cousins in Reference [107]. These intervals are constructed in a way that the true value is always covered with the specified probability. As the profile likelihood is used here, some values of the nuisance parameters can violate this, but for practical cases these violations are usually of no interest, see e.g. Reference [108].

The choice of 10000 pseudo experiments yields a statistical uncertainty of the method of 0.02 % on the estimated parameter value. The described procedure is implemented based on the ROOT framework by the ATLAS collaboration and commonly employed for limit setting by several analyses of electroweak final states.

8.2 Phase Space Optimisation

The limits can be derived with the results of the previous chapter, but the sensitivity can be increased as the event selection is optimised for the analysis of the Standard Model $WW\gamma$ signal. Anomalous quartic gauge couplings would lead to an enhanced signal yield in the high energy range, as can be seen in Figure 8.3 for two examples of couplings. The cross-section is shown as a function of the transverse photon momentum and similar features are observed for both couplings. The Standard Model expectation exhibits a steeply falling behaviour, whereas the distributions that include anomalous quartic gauge couplings show an increase of the differential cross-section for large values of p_{T}^{γ}. The distribution computed with the larger coupling values (round markers) show the largest deviation from the Standard Model expectation. The second distribution showing anomalous quartic couplings (square markers) follows the Standard Model expectations for a larger range in transverse photon momentum, but also shows an increased cross-section prediction. The anomalous couplings shown here are for illustrative purposes only, as they are excluded by other analyses [23, 24] by about an order of magnitude, as is further described in Section 8.3.1.

The backgrounds to the search for anomalous quartic gauge couplings are the same as the ones of the analysis of the Standard Model signal, and thus they are steeply falling with increasing photon p_{T} as can be seen in Figure 6.12a. Since the anomalous quartic gauge couplings enhances the signal at high transverse photon momenta, a minimum requirement on this observable can be introduced in order to increase the sensitivity. By introducing a tighter p_{T}^{γ} threshold, most of the backgrounds can be discarded and the purity of the sample is increased. The gain in sensitivity is evaluated in terms of the expected limits. Therefore, the limits are calculated as a function of the transverse photon momentum threshold applied in addition to the standard event selection as described in Chapter 5. For the calculation of the p-value in Equation (8.12) the observed number of events is substituted with the expected number

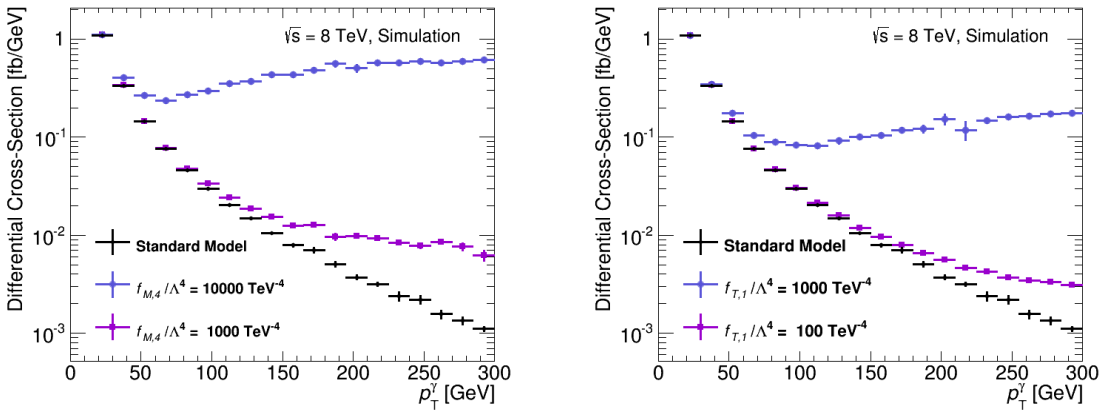

Figure 8.3: Cross-section for $e\mu\gamma$ production as a function of the transverse momentum of the photon. The Standard Model expectations are shown along with two different values of the anomalous quartic gauge couplings $f_{M,4}/\Lambda^4$ (a) and $f_{T,1}/\Lambda^4$ (b). A clear deviation of the distributions is visible for high transverse photon momenta. The values are obtained using the VBFNLO program.

of events when no anomalous gauge couplings are present, i.e. $N^{\text{obs.}} = N^{\text{aQGC}}(0) + N^{\text{bg.}}$. This is done because the optimisation of the phase space should not rely on the observed data as otherwise fluctuation effects could be artificially enhanced. Therefore, the expected limit is computed as the limit observed when only the Standard Model couplings are present.

The parabolic parametrisation of the cross-section has to be recomputed for every tested value of the photon p_{T} threshold and in principle the full background estimation described in Chapter 6 needs to be redone. This is not feasible though, as with increasing requirements on the photon transverse momentum less events are present in the control regions of the ABCD method up to a point where the method no longer works. Therefore, the results obtained in Chapter 6 are employed and extrapolated to the region with the p_{T}^γ threshold under test. To this end, the transverse photon momentum distribution of the cumulative background distribution is fitted with an exponential function, $f(x) = exp(p_0 + p_1 \cdot x)$, as shown in Figure 8.4. The estimated number of background events is shown as a function of transverse photon momentum and corresponds to the coloured stacked histograms in Figure 6.12a. Thus the normalisation of the backgrounds is obtained from the ABCD method described in Section 6.3.3 and the distribution of the photon p_{T} is taken from Monte Carlo simulation as detailed in Section 6.4. The steeply falling distribution is fitted in the range of $15\,\text{GeV} < p_{\text{T}}^\gamma < 150\,\text{GeV}$ and the fit parameters are indicated in the figure. Good agreement is observed and confirmed by a low value of χ^2/NDF.

The expected number of events is obtained by integrating the function from the threshold of transverse photon momentum onwards. The uncertainties shown in the figure correspond to the squared sum of the statistical and the systematic uncertainty obtained from the background estimation. They are propagated to the fit result as uncertainties on the fit parameters. The expected number of events is recomputed for the exponential functions varied within their uncertainties and the maximal deviation from the nominal value is quoted as the propagated uncertainty. The systematic uncertainty of the fitting procedure is evaluated by varying the range of the fit. Both the lower and the upper fit boundary are individually raised and lowered

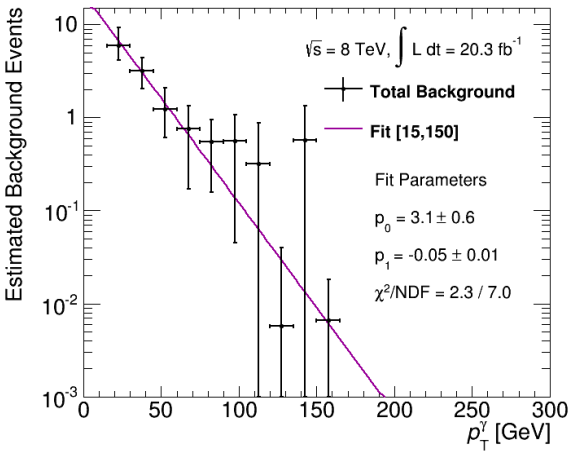

Figure 8.4: Background events to the $e\mu\gamma$ signal as a function of transverse photon momentum. Also shown is the fit of an exponential function to the distribution along with its fit parameters. This function is used in order to extrapolate the expected number of background events to regions with large p_{T}^{γ} thresholds.

by 15 GeV and the distribution is refitted. The expected number of events is reevaluated and the maximal deviation from the nominal value is added quadratically to the uncertainty of the fit to obtain the total uncertainty of the background extrapolation. This way the quantity $N^{\mathrm{bg.}}$ is recomputed for each value of tested p_{T}^{γ} threshold.

The expected cross-section $\sigma_{\mathrm{fid.}}^{\mathrm{aQGC}}(\frac{f_i}{\Lambda^4})$ is computed using the VBFNLO generator and converted to the expected number of signal events using Equation (8.3). For the optimisation, the correction factor ε and parton to particle level corrections are fixed to the values obtained in Chapter 7 for all photon p_{T} requirements. The expected limits as function of the p_{T}^{γ} threshold of the event selection is shown for two examples of anomalous quartic gauge couplings in Figure 8.5. The transverse photon momentum threshold is raised in steps of 15 GeV indicated by the round markers. Coupling values that can be excluded with the given event selection requirements are represented by the shaded region. The expected limits improve with increasing photon p_{T} at first, as more and more background events are discarded. At around p_{T}^{γ} =100 GeV, the contribution from the background events is almost zero and the region of maximal sensitivity is reached. Above this region, the limits slightly worsen, as more signal events are discarded, resulting in a loss of sensitivity. At these photon energies, the expected number of Standard Model events is zero, such that the observed loss of sensitivity can be attributed to the broadening of the cross-section parabola as more and more signal events are discarded. For the same number of expected events, i.e. zero, this leads to worse limits, as the same coupling parameter value leads to a smaller increase in observed events.

Figure 8.5 also indicates the current best limits on the couplings which are obtained by the analysis of the vector boson scattering of two photons to two W bosons [23] for $f_{M,4}/\Lambda^4$ and by the scattering of four W bosons for $f_{T,1}/\Lambda^4$ [24]. The term vector boson scattering denotes the type of collisions where one quark of each of the two incoming protons radiates a vector boson. These bosons collide with each other producing another pair of vector bosons. This way, they are sensitive to anomalous quartic gauge couplings when the final state contains two electroweak bosons. Vector boson scattering events have a very special topology, as the hadronic remnant the bosons are radiated from continue their path in opposite directions

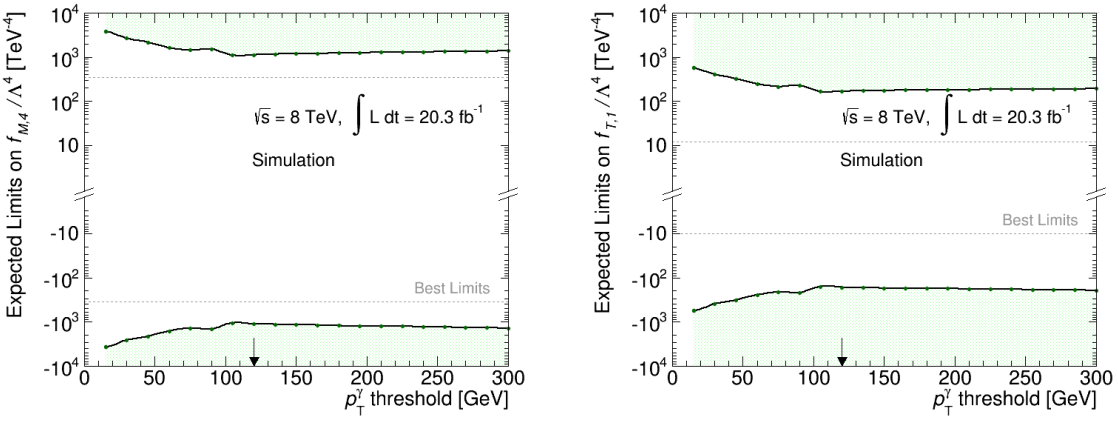

(a) **(b)**

Figure 8.5: Expected limits at 95 % confidence level on $f_{M,4}/\Lambda^4$ (a) and $f_{T,1}/\Lambda^4$ (right) as function of the photon p_T threshold of the event selection. The coloured area corresponds to the excluded values of the corresponding coupling. Also indicated are the current best limits from References [23] (b) and References [24] (right). The optimal p_T^γ threshold, chosen for stability reasons to correspond to 120 GeV, is shown by the arrow.

yielding typically two jets with a large rapidity separation. This rather unique topology can be exploited in the definition of the event selection for an efficient background suppression leading to stringent exclusion limits.

In order to compare the limits quoted in References [23] and [24] with the values obtained here, a conversion of the values has to be performed. This is because the field strength tensors are defined slightly different in the reference and the parametrisation provided by VBFNLO used in this work. The conversion can be found in Reference [109], but is of no relevance for this discussion, as all the quoted values use the same parametrisation. Yet this difference needs to be kept in mind, when comparing limits from different publications.

The optimisation of the expected limits is mainly influenced by the expected number of background events as for all different anomalous quartic gauge couplings the same parabolic model of the cross-section expectation is used. Therefore, only the absolute value of the limits is influenced by the specific parabola, but the general shape of the exclusion limits contour stays the same. This is observable, when comparing Figure 8.5a and Figure 8.5b. Thus, one common p_T^γ threshold is chosen for all tested couplings and it is set to $p_T^\gamma = 120$ GeV. This value is used in order to be within the plateau region of Figure 8.5. The point at 105 GeV promises a slightly better limit, but it is not as stable compared to its neighbouring points. Therefore, the value at $p_T^\gamma = 120$ GeV is taken and indicated in Figure 8.5 by the arrows.

8.3 Limit Determination

The limits on the anomalous quartic gauge couplings are derived using the event selection discussed in Chapter 5, with an increased requirement on the transverse momentum of the photon of 120 GeV in order to improve the sensitivity. This value might change the correction factor ε and the parton to particle level correction factor $C^{parton \to particle}$ due to the slightly changed phase space, such that these values have to recomputed. This is needed, since they

are used to convert the cross-section computed with VBFNLO into the expected number of events, as described by Equation (8.3).

The correction factor ε increases by about 6 % as the photon identification efficiency rises with increasing transverse photon momentum, as can be seen in Figure 4.3. The value obtained with the requirement that the transverse photon momentum exceeds 120 GeV is:

$$\varepsilon = 0.320 \pm 0.045(\text{stat.}) \pm 0.089(\text{syst.}).$$

This value has an increased statistical uncertainty compared to the nominal value, as the same data set is used and the additional requirements on the photon discards a large fraction of events. The systematic uncertainty is again dominated by the generator difference, which increases to 25.5 % in this specific region of phase space.

The correction factor is used for the conversion of the cross-section to an event count for the Standard Model expectation, i.e. $f_i/\Lambda^4 = 0$, but also for all other values computed with different strengths of the anomalous couplings. This can affect the reconstruction efficiency since the number of high energetic events increases with increasing coupling parameter strength, as shown in Figure 8.3. Yet, due to the strong requirement on the transverse photon momentum, only high energetic events are selected, such that the difference in the correction factor is expected to be small between the Standard Model value on the correction factor computed for a certain coupling $f_i/\Lambda^4 \neq 0$. In order to test this hypothesis, Monte Carlo samples of five different anomalous couplings were generated including the full event reconstruction in order to be able to recompute the correction factor. As the topologies for the Standard Model and low values of anomalous coupling parameters are rather similar, large values of the couplings, that are actually already excluded by other analyses, are chosen in order to evaluate the effect in a conservative way. In detail, the chosen couplings are: $f_{M,0}/\Lambda^4 = -1876\,\text{TeV}^{-4}$, $f_{M,1}/\Lambda^4 = -30482\,\text{TeV}^{-4}$, $f_{M,2}/\Lambda^4 = -13099\,\text{TeV}^{-4}$, $f_{M,3}/\Lambda^4 = -21285\,\text{TeV}^{-4}$ and $f_{T,0}/\Lambda^4 = 1374\,\text{TeV}^{-4}$. No significant deviation from the correction factor computed with the Standard Model simulation is observed for any of the samples. Therefore, a constant value of ε is assumed for all values of the anomalous couplings.

The parton to particle level correction factor $C^{parton \to particle}$ is also evaluated for the higher threshold on the transverse photon momentum. As this quantity describes the difference between the objects at parton and particle level, little influence of the additional criterion on the photon is expected. This is also observed when recomputing the value, as the values for the different p_{T}^{γ} thresholds agree within their statistical uncertainty. When the parton to particle level correction factor of the Standard Model simulation is compared to the ones computed when additional couplings are simulated, significant differences are found. This is due to the fact that the anomalous couplings give rise to high energetic events. Therefore, also the jets in the events carry more energy and they mainly affect the parton to particle level correction factor. The difference between the rejection of events containing jets at parton and particle level diminishes as the jet energy is further away from the p_{T} threshold of 25 GeV. Therefore, more events are discarded due to the jet p_{T} requirement, but overall, the difference between the parton and particle level expectation decreases. As the amount of additional high energetic events in comparison to the Standard Model expectations changes with the strength of the coupling f_i/Λ^4 (seen in Figure 8.3), the parton to particle level correction factor is expected to vary slightly as a function of the coupling strength. Evaluating this effect requires quite some computational effort, as a several thousand events need to be simulated for the values of a given coupling f_i/Λ^4. Yet the change of the parton to particle level correction factor is

N^{obs}	0
$N^{\text{bg.}}$	0.06 ± 0.21
ε	0.32 ± 0.10
$C^{parton \to particle}$	1.10 ± 0.08
$\text{L}_{\text{int.}}$	$(20.3 \pm 0.6)\,\text{fb}^{-1}$

Table 8.1: Input values for the computation of exclusion limits on anomalous quartic gauge couplings. The quoted uncertainty corresponds to the total uncertainty on the value.

a subleading effect, as it is much smaller than the systematic uncertainty of the correction factor ε. Therefore, a constant parton to particle correction factor is taken for all values of the anomalous quartic gauge couplings and the largest difference observed in the study of the five samples simulating anomalous couplings is taken as a systematic uncertainty. This is a conservative approach, as the tested couplings are experimentally excluded, such that the real effect on the parton to particle level correction factor is expected to be much smaller. All in all, the $C^{parton \to particle}$ amounts to:

$$C^{parton \to particle} = 1.10 \pm 0.01(\text{stat.}) \pm 0.08(\text{syst.}),$$

and is employed in the computation of the expected number of events for a given coupling.

The extrapolated number of background events in the optimised phase space region obtained using the exponential fit amounts to $N^{\text{bg.}} = 0.06 \pm 0.21$ with a rather large uncertainty due to the extrapolation. No recorded event is selected by the optimised signal selection, such that $N^{\text{obs}} = 0$. All inputs for the determination of the limits on anomalous quartic gauge couplings are summarised in Table 8.1.

8.3.1 Limits without Unitarisation

The limits on anomalous quartic gauge couplings can be derived using the inputs in Table 8.1 and the corresponding parabolic parametrisation $\sigma_{\text{fid.}}^{\text{aQGC}}(f_i/\Lambda^4)$ of the anomalous coupling under test. This is obtained using the Monte Carlo generator VBFNLO and converted into an expected number of events according to Equation (8.3). Exclusion limits are set on all 14 parameters this analysis is sensitive to and the parabolic parametrisation for each coupling is given in Table A.4 in the appendix.

The limits derived with the method described in Section 8.1 are visualized in Figure 8.6 and detailed in Table 8.2. The observed and the expected exclusion limits are indicated for the different anomalous quartic gauge couplings. Also given are the best limits on the respective couplings published to date. They come from several analyses that have in common that they are specialised in the study of vector boson scattering. Therefore, their sensitivity to anomalous quartic gauge couplings comes from two-to-two electroweak boson scattering as indicated in the last column of Table 8.2. In this work a one-to-three process is studied, but the increased sensitivity of the vector boson scattering analysis to anomalous quartic gauge couplings mainly comes from the fact that the special event topology yields better background suppression possibilities.

The expected limits are computed using pseudo experiments for the number of observed events, $N'^{\text{obs.}}$ and the corresponding nuisance parameters $\boldsymbol{\theta}'$. The number of observed events is drawn randomly from a Poisson distribution whose mean corresponds to the expected number

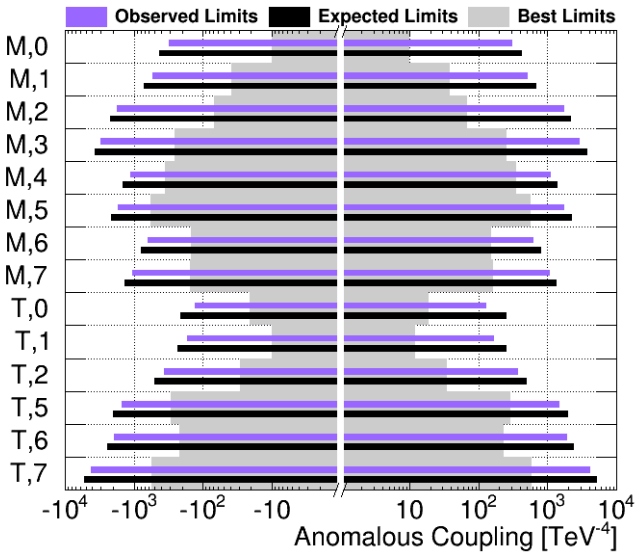

Figure 8.6: Visualisation of the observed and expected limits at 95 % confidence level on the different anomalous quartic gauge couplings. The current best limits are shown in grey and come from different analyses [23, 24, 110, 111] as detailed in Table 8.2. For brevity, only the index i of the coupling f_i/Λ^4 is indicated in the figure.

of events when no anomalous quartic gauge couplings are present, i.e. $N^{\mathrm{aQGC}}(0, \boldsymbol{\theta}) + N^{\mathrm{bg.}}(\boldsymbol{\theta})$. The nuisance parameters $\boldsymbol{\theta}$ for the evaluation of the mean are set to the maximum likelihood estimators of the events observed in data for the hypothesis that no additional couplings are present. The nuisance parameters $\boldsymbol{\theta}'$ are obtained by drawing a random number from a normal distribution. The exclusion limits for these particular inputs of $N'^{\mathrm{obs.}}$ and $\boldsymbol{\theta}'$ are computed and the whole procedure is repeated 5000 times to obtain a distribution of expected limits. The mean value of the distribution of the upper and respectively lower limits from the pseudo experiments is taken as the expected upper and lower exclusion limit on the coupling.

The observed limits are more stringent than the expected ones for all parameters, as no event is observed in the optimised phase space. The fluctuations within the uncertainties that are simulated using the pseudo experiments can therefore only yield a larger number of observed events, as no negative event count is admitted. As more observed events yield worse limits, the expected limits are always smaller than the observed ones for this measurements.

The term $\gamma\gamma \to WW$ in Table 8.2 refers to the analysis of final states containing an electron-muon pair and no associated charged particles from the same vertex [23]. This way the scattering of two photons that are radiated from the incoming quarks and produce a pair of W bosons with opposite charge can be studied. The analysis described in Reference [23] combines the analysis of this final state recorded with the CMS detector at a centre-of-mass energy of 7 and 8 TeV, leading to improved limits with respect to the analysis of the single data sets [112, 113]. With the combined data set, this analysis yields the best limits on the anomalous quartic gauge couplings $f_{M,0}/\Lambda^4$, $f_{M,1}/\Lambda^4$, $f_{M,3}/\Lambda^4$ and $f_{M,4}/\Lambda^4$.

The term $W\gamma \to W\gamma$ denotes the study of electroweak-induced production of $W\gamma$ final states [110]. The full data set with $\sqrt{s} = 8\,\mathrm{TeV}$ recorded by the CMS detector is used and events with a leptonically decaying W boson, an energetic muon and two jets with a large rapidity separation are selected. The quartic vertex arises from the scattering of a W boson and a photon. This way, this analysis is also sensitive to the 14 anomalous quartic gauge

Coupling	Observed Limits [TeV^{-4}]	Expected Limits [TeV^{-4}]	Current Best [TeV^{-4}]	Analysis
$f_{M,0}/\Lambda^4$	[-311, 315]	[-426, 426]	[-10, 10]	$\gamma\gamma \to WW$
$f_{M,1}/\Lambda^4$	[-535, 522]	[-717, 699]	[-38, 38]	$\gamma\gamma \to WW$
$f_{M,2}/\Lambda^4$	[-1760, 1767]	[-2194, 2205]	[-69, 69]	$\gamma\gamma \to WW$
$f_{M,3}/\Lambda^4$	[-3033, 2978]	[-3713, 3757]	[-255, 255]	$\gamma\gamma \to WW$
$f_{M,4}/\Lambda^4$	[-1122, 1139]	[-1464, 1426]	[-351, 351]	$W\gamma \to W\gamma$
$f_{M,5}/\Lambda^4$	[-1722, 1754]	[-2160, 2240]	[-570, 570]	$W\gamma \to W\gamma$
$f_{M,6}/\Lambda^4$	[-622, 629]	[-799, 825]	[-148, 152]	$WW \to WW$
$f_{M,7}/\Lambda^4$	[-1056, 1077]	[-1351, 1375]	[-155, 164]	$WW \to WW$
$f_{T,0}/\Lambda^4$	[-129, 132]	[-214, 255]	[-21, 19]	$WW \to Z\gamma$
$f_{T,1}/\Lambda^4$	[-166, 170]	[-234, 257]	[-10, 12]	$WW \to WW$
$f_{T,2}/\Lambda^4$	[-361, 371]	[-506, 503]	[-29, 35]	$WW \to WW$
$f_{T,5}/\Lambda^4$	[-1501, 1485]	[-1990, 1991]	[-292, 292]	$W\gamma \to W\gamma$
$f_{T,6}/\Lambda^4$	[-1908, 1908]	[-2399, 2446]	[-215, 230]	$W\gamma \to W\gamma$
$f_{T,7}/\Lambda^4$	[-4180, 4169]	[-5202, 5184]	[-561, 591]	$W\gamma \to W\gamma$

Table 8.2: Summary of the observed, expected and current best limits at 95 % confidence level on the different couplings. The parametrisation used by the VBFNLO program is employed, thus the numbers quoted from the publications are converted according to Reference [109]. The current best limits stem from four different analyses whose vector boson scattering process is indicated by the last column [23, 24, 110, 111].

couplings discussed here and it is the only one to quote limits on all these couplings.

The study of events containing two W bosons with the same electrical charge is denoted by $WW \to WW$ [24]. The same data set as for the $W\gamma \to W\gamma$ analysis is studied. The event selection requires two leptons with the same electrical charge and two jets with a large rapidity separation. This enhances the contribution from the scattering of four W bosons where two are radiated from the incoming quarks. Thus, this analysis studies the $WWWW$ vertex and sets stringent limits on $f_{M,6}/\Lambda^4$, $f_{M,7}/\Lambda^4$, $f_{T,1}/\Lambda^4$ and $f_{T,2}/\Lambda^4$.

The analysis denoted $WW \to Z\gamma$ in Table 8.2 studies the electroweak production of $Z\gamma$ events [111]. The strategy is very similar to the analysis of the electroweak produced $W\gamma$ final states and the same data set is analysed. The events are selected by requiring a photon, a pair of light leptons and two jets with a large rapidity separation. The last requirement favours the production of $Z\gamma$ events via vector boson scattering. This analysis holds the best limits on the parameter $f_{T,0}/\Lambda^4$.

The results obtained here confirm the observation of the studies using vector boson scattering events. Yet, the limits are not as stringent as the ones quoted above due to the lower sensitivity of this analysis. This is due to the loss of a considerable fraction of the signal arising from the background rejection criteria. Still the analysis cannot be performed without these requirement, as then the signal purity would be too low. The results obtained here are similar to the ones obtained by the analysis of the triboson final state $W\gamma\gamma$ [5] which uses the same data set. The limit set by the $W\gamma\gamma$ analysis on the transverse coupling $f_{T,0}/\Lambda^4$ is slightly better than the one

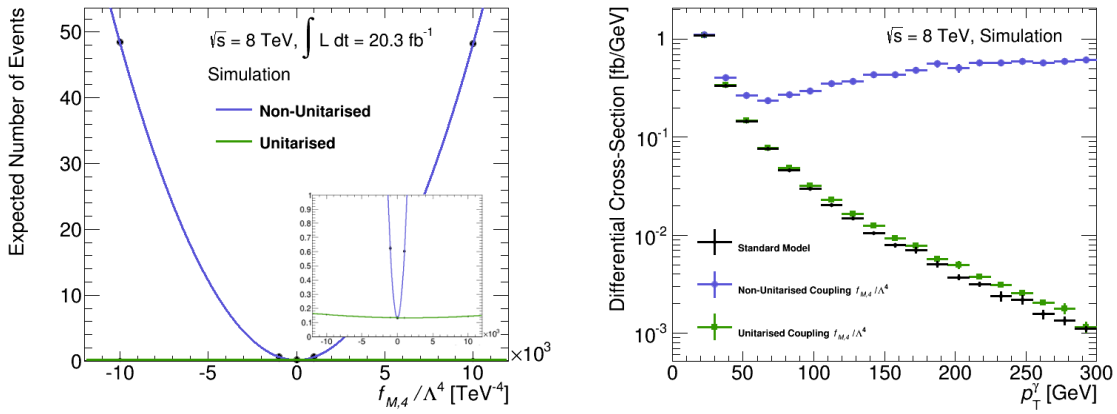

(a) (b)

Figure 8.7: Comparison of unitarised and non-unitarised quartic gauge couplings with $f_{M,4}/\Lambda^4 = 10000\,\text{TeV}^{-4}$. The unitarisation is performed by applying a dipole form factor with $\Lambda_{FF} = 500\,\text{GeV}$. Figure 8.7a shows the parabolic dependence of the expected number of events and the inset shows the same figure with a zoom on the y-axis. The differential cross-section is shown as a function of the photon transverse momentum in Figure 8.7b. The distributions are presented for the Standard Model only hypothesis and for the existence of anomalous quartic gauge couplings with and without unitarisation.

obtained here, but the limits on the mixed couplings $f_{M,2}/\Lambda^4$ and $f_{M,3}/\Lambda^4$ are improved by the current work. This is because of the additional contribution from the $WWZ\gamma$ vertex, which the $W\gamma\gamma$ analysis is not sensitive to.

The limits obtained here are useful to compare the sensitivity of this work with other analyses of quartic gauge boson couplings, but they are unphysical, as the couplings violate unitarity at the tested energy scales. Therefore, the from factor unitarisation explained in Section 1.4.1 is employed and unitarity conserving limits are derived.

8.3.2 Limits with Unitarisation

In order to conserve unitarity, the anomalous gauge couplings f_i/Λ^4 are multiplied with a dipole form factor given by Equation 1.4 when choosing a cut-off power of $p = 2$:

$$F(\hat{s}) = \left(1 + \frac{\hat{s}}{\Lambda_{FF}^2}\right)^{-2}, \tag{8.13}$$

The form factor scale Λ_{FF} needs to be chosen small enough to conserve unitarity at all energy ranges accessible with this analysis, i.e $\sqrt{\hat{s}} \leq 8\,\text{TeV}$. Effectively the choice of Λ_{FF} broadens the parabola of the cross-section expectation in dependence of a given coupling from Equation (8.2), as it dampens the coupling. This is also visible in Figure 8.7a, where the parabolic parametrisation of the unitarised and non-unitarised coupling $f_{M,4}/\Lambda^4 = 10000\,\text{TeV}^{-4}$ are compared. The damping effect of the unitarisation leads to unitarised parabola appearing like a straight line in comparison to the non-unitarised one in the shown range. Therefore, the inset shows the same figure with a smaller y-axis range, to depict the parabolic shape of the unitarised fit as well. Due to the effective cross-section damping of the unitarisation, the exclusion limits depend on the chosen form factor scale and worsen with decreasing Λ_{FF}.

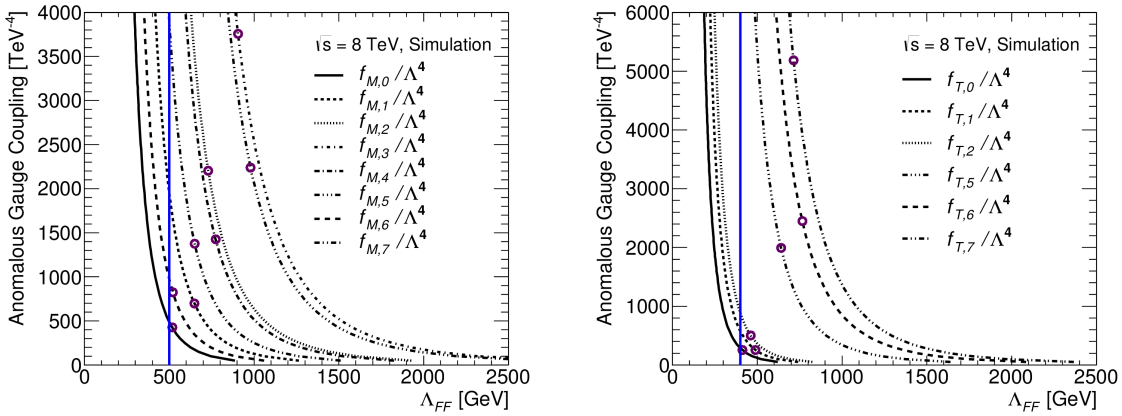

Figure 8.8: Minimal dipole form factor scale Λ_{FF} to conserve unitarity as a function of the strength of the mixed (a) and transverse (b) anomalous quartic gauge couplings. The expected limits obtained by this analysis are circled for each coupling. They have to yield larger form factor scales than the common one chosen to unitarise all mixed or transverse couplings respectively in order to guarantee unitarity for all couplings. The common scales are indicated by the vertical lines in the figures.

The effect of a unitarisation with a dipole form factor and $\Lambda_{FF} = 500\,\text{GeV}$ on the differential cross-section as a function of the transverse photon momentum is shown in Figure 8.7b. While the non-unitarised cross-section increases strongly with p_{T}^{γ}, the unitarised expectation values do not differ much from the Standard Model distribution due to the damping effect of the form factor.

The determination of the maximal value of Λ_{FF} that still conserves unitarity is performed by employing a partial wave decomposition of the scattering matrix of on-shell two-to-two vector boson scattering: $VV \rightarrow VV$, with $V \in \{W, Z, \gamma\}$. The absolute value of the real part of the zeroth partial wave of the amplitude is required to be below 0.5 for the unitarity conservation [114]. The two-to-two scattering of all possible electroweak boson configurations is considered individually for a given value of the anomalous quartic gauge coupling f_i/Λ^4 and the corresponding maximal form factor scale determined. Additionally, the scattering of states with the same electrical charge is evaluated collectively [115]. While the determination of Λ_{FF} is based on two-to-two processes and this works studies a one-to-three boson process, it still yields viable results for the estimation of the unitarity violation. The computation is implemented as part of the VBFNLO program package [116] and employed here.

Figure 8.8 shows the minimal value of the form factor scale Λ_{FF} that is needed to conserve unitarity with a dipole form factor as a function of the anomalous quartic gauge couplings. The expected limits obtained in this analysis from Table 8.2 are circled in the figure for each parameter. This yields one minimal form factor scale per gauge coupling and all values of Λ_{FF} below this scale also conserve unitarity for this parameter. One common form factor scale is chosen for the mixed and the transverse gauge couplings respectively. They are indicated in the figure by the vertical line. For the mixed couplings $\Lambda_{FF} = 500\,\text{GeV}$ is a conservative choice and is driven by the minimal scales obtained for the couplings $f_{M,0}/\Lambda^4$ and $f_{M,6}/\Lambda^4$ which are close to 500 GeV, see Figure 8.8a. In order to guarantee unitarity conservation for all transverse couplings, the value of the form factor scale needs to be lowered to $\Lambda_{FF} = 400\,\text{GeV}$. This value

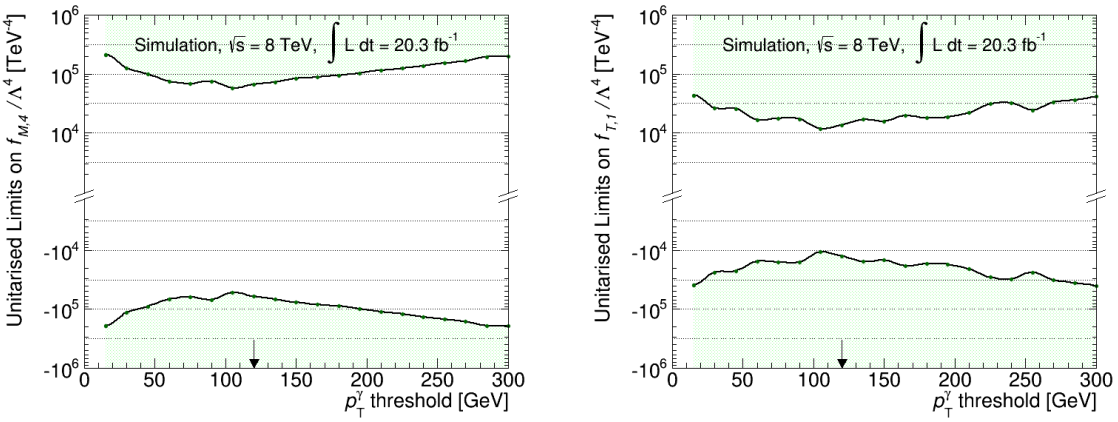

(a) **(b)**

Figure 8.9: Expected limits at 95 % confidence level on the unitarised couplings $f_{M,4}/\Lambda^4$ (a) and $f_{T,1}/\Lambda^4$ (b) as function of the photon p_T threshold of the event selection. The coloured area corresponds to the excluded limits. A dipole form factor is employed for the unitarisation and the form factor scale is set to 500 GeV for $f_{M,4}/\Lambda^4$ and to 400 GeV for $f_{T,1}/\Lambda^4$. The p_T^γ threshold chosen for this analysis corresponds to 120 GeV and is indicated by the arrow.

is driven by the coupling $f_{T,0}/\Lambda^4$, but also the expected limits on $f_{T,2}/\Lambda^4$ and $f_{T,1}/\Lambda^4$ require a small value of Λ_{FF} to conserve unitarity. Only the positive values of the couplings are shown in Figure 8.8, but the conclusions also hold for the negative values of the expected exclusion limits.

For the limit setting, the inputs given in Table 8.1 can be reused, but the parabolic dependence of the expected number of events given in Equation 8.3 has to be reevaluated. To this end, the expected cross-section for the anomalous quartic gauge coupling is computed with the form factor applied. The values computed without unitarisation cannot be reused, as the unitarisation depends on the scale $\hat{s}$ of the specific event, such that a simple reweighting is not applicable.

The expected limits as a function of the minimum requirement on the transverse momentum of the photon are recomputed to test if the photon p_T threshold of 120 GeV is also viable for unitarised couplings. The resulting distribution is shown in Figure 8.9 for the two couplings $f_{M,4}/\Lambda^4$ and $f_{T,1}/\Lambda^4$. The expected limits are much smaller than the non-unitarised ones shown in Figure 8.5, and the sensitivity of the analysis decreases more rapidly at high transverse photon momenta, as there is little signal expected. Yet, the p_T^γ threshold of 120 GeV, indicated by the arrow, lies in the middle of the rather stable region of exclusion limits between $50\,\text{GeV} < p_T^\gamma < 200\,\text{GeV}$. Therefore, it is a good choice and it is kept as requirement also for the limit setting for unitarised couplings.

The shape of the expected unitarised limits in Figure 8.9 is not as smooth as in the non-unitarised case (see Figure 8.5), due to the lower strength of the unitarised couplings. As the parabola is much flatter, computing only five values for fitting the parabola leaves room for fluctuations. Thus, for the computation of the parabola with the optimised p_T^γ threshold, that is employed in the limit setting, seven cross-section values of each anomalous quartic gauge coupling are computed with the form factor applied. This yields a more reliable fit and the parametrisations of the expected number of events as a function of the couplings are given in

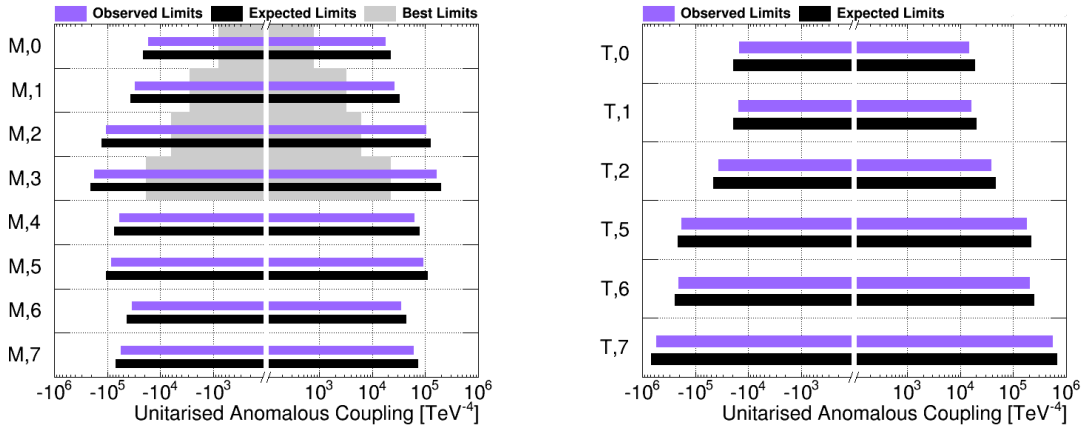

Figure 8.10: Visualisation of the observed and expected limits at 95 % confidence level on the unitarised anomalous quartic gauge couplings. The left figure shows the limits for the mixed gauge couplings unitarised with a dipole form factor and a scale of $\Lambda_{FF} = 500\,\text{GeV}$. For the upper four couplings, published limits exist [23] with the same unitarisation and are shown in grey. The figure on the right shows the exclusion limits for the transverse gauge couplings unitarised with a dipole form factor and a scale of $\Lambda_{FF} = 400\,\text{GeV}$. No limits with the same unitarisation are published to date.

Tables A.5 and A.6 in the appendix. As expected, these parabolas are much flatter than the ones for the non-unitarised values in Table A.4.

The inputs of Tables 8.1 and A.5 are used to set the exclusion limits on the mixed anomalous gauge couplings unitarised with a dipole form factor with a scale of $\Lambda_{FF} = 500\,\text{GeV}$. The observed and expected limits are computed at 95 % confidence level as described in the previous sections. The results are visualised in Figure 8.10a and detailed in Table 8.3. For four of the couplings the analysis of the vector boson scattering of two photons and two W bosons [23] set limits and is using the same unitarisation, such that the results are based on the same footing. Again, the limit set by that analysis are better than the ones of this work, since the same inputs are used as for the non-unitarised limits. For the remaining four couplings, no unitarised limits are published as of yet, hence the limits derived here are the current best limits.

The observed and expected exclusion limits on the transverse anomalous gauge couplings unitarised with a dipole form factor and $\Lambda_{FF} = 400\,\text{GeV}$ are shown in Figure 8.10b and listed in Table 8.4. While the analysis of $W\gamma\gamma$ final states [5] does compute a limit on the coupling $f_{T,0}/\Lambda^4$ unitarised with a dipole form factor, the limit is not comparable to the one obtained here. This is because in that analysis a larger value of $\Lambda_{FF} = 600\,\text{GeV}$ is afforded. Therefore, the expected non-unitarised limit is lower, leading to a larger freedom in the choice of the unitarisation scale. No limits on the other transverse couplings with the same unitarisation applied here are published, such that no comparison to any other measurement can be made here.

All in all, the full sensitivity of this analysis is exploited by setting exclusion limits at 95 % confidence level on all accessible anomalous quartic gauge coupling parameters. This is done for the plain couplings as well as for the couplings unitarised with a dipole form-factor. The computed limits on the non-unitarised couplings are not as stringent as the current best limits,

Coupling	Observed Limits [TeV^{-4}]	Expected Limits [TeV^{-4}]	Current Best [TeV^{-4}]	Analysis
$f_{M,0}/\Lambda^4 \cdot F(\hat{s})$	[-17065, 17831]	[-21402, 22591]	[-798, 798]	$\gamma\gamma \to WW$
$f_{M,1}/\Lambda^4 \cdot F(\hat{s})$	[-29711, 26558]	[-36742, 33594]	[-2814, 3283]	$\gamma\gamma \to WW$
$f_{M,2}/\Lambda^4 \cdot F(\hat{s})$	[-104603, 105943]	[-127340, 129520]	[-6222, 6222]	$\gamma\gamma \to WW$
$f_{M,3}/\Lambda^4 \cdot F(\hat{s})$	[-173684, 165972]	[-208370, 201540]	[-18670, 22270]	$\gamma\gamma \to WW$
$f_{M,4}/\Lambda^4 \cdot F(\hat{s})$	[-59948, 63480]	[-73828, 77580]	-	-
$f_{M,5}/\Lambda^4 \cdot F(\hat{s})$	[-84529, 92556]	[-103740, 112720]	-	-
$f_{M,6}/\Lambda^4 \cdot F(\hat{s})$	[-34117, 35619]	[-43069, 44095]	-	-
$f_{M,7}/\Lambda^4 \cdot F(\hat{s})$	[-55615, 60892]	[-68843, 74390]	-	-

Table 8.3: Summary of the observed, expected and current best limits at 95 % confidence level on unitarised mixed quartic couplings. The parametrisation used by the VBFNLO program is employed, thus the numbers from the quoted publication are converted according to Reference [109]. The current best limits for the first four parameters are set by the analysis of $\gamma\gamma \to WW$ vector boson scattering [23]. Where the values are not quoted, no limits exist with the same unitarisation as is employed here. The unitarisation is performed using a dipole form factor with $\Lambda_{FF} = 500\,\text{GeV}$.

as those are set by analyses of vector boson scattering that can exploit the event topology for a better discrimination of the signal and background processes. Due to the same reason, also the unitarised limits computed here are not as good as the ones that are published, as the same inputs are used for their computation. Yet, this analysis quotes limits on all accessible couplings with unitarisation and for the majority of these, no other public result exists.

Coupling	Observed Limits [TeV^{-4}]	Expected Limits [TeV^{-4}]
$f_{T,0}/\Lambda^4 \cdot F(\hat{s})$	[-14845, 15018]	[-18882, 19098]
$f_{T,1}/\Lambda^4 \cdot F(\hat{s})$	[-15261, 16216]	[-19280, 20561]
$f_{T,2}/\Lambda^4 \cdot F(\hat{s})$	[-36338, 38519]	[-45925, 47452]
$f_{T,5}/\Lambda^4 \cdot F(\hat{s})$	[-180081, 179930]	[-215950, 217310]
$f_{T,6}/\Lambda^4 \cdot F(\hat{s})$	[-203711, 205202]	[-244040, 246750]
$f_{T,7}/\Lambda^4 \cdot F(\hat{s})$	[-547974, 555963]	[-673620, 684980]

Table 8.4: Summary of the observed and expected limits at 95 % confidence level on unitarised transverse gauge boson couplings. The parametrisation used by the VBFNLO program is employed. The unitarisation is performed using a dipole form factor with $\Lambda_{FF} = 400\,\text{GeV}$. No other results with the same unitarisation exist.

Summary

The analysis presented here is the first study of the fully leptonic decay of two W bosons that are produced in association with a photon in hadron collisions. The main challenge of this study is the low production probability of the process. Therefore, the data set with the largest statistics recorded by the ATLAS detector is employed. It has an integrated luminosity of $L_{int.} = 20.3\,fb^{-1}$ and a centre-of-mass energy of $\sqrt{s} = 8\,TeV$. The production cross-section of this process is orders of magnitudes smaller than the cross-section of dijet or diboson production. Thus, efficient background rejection criteria have to be defined to isolate the signal.

The fully leptonic final states are selected by requiring the presence of one electron, one muon and a photon in the event. Background processes mainly arising from $Z\gamma$ and Drell-Yan production are reduced by introducing minimal thresholds on the relative transverse momentum imbalance and the dilepton invariant mass. Events containing energetic jets are excluded from this analysis to suppress background processes containing top quarks. The remaining background also has contributions from misidentified objects and is estimated using a combination of Monte Carlo simulations and two sideband methods. To this end, six additional sets of event selection criteria are defined based on the energy isolation of the objects. The number of signal events is extracted using a likelihood formulation of the expected number of events accepted by the different selections and the fiducial cross-section is computed. It amounts to $\sigma_{\text{fid.}}^{e\mu\gamma} = (1.89 \pm 0.93(\text{stat.}) \pm 0.41(\text{syst.}) \pm 0.05(\text{lumi.}))\,fb$ and agrees with the theoretical expectation at next-to-leading order of $\sigma_{\text{fid.}}^{\text{theory}} = (1.99 \pm 0.09)\,fb$. While the result is in good agreement with the Standard Model expectations, no observation of the signal can be claimed due to the limited statistics of the analysed data. The sensitivity of this analysis can only be increased significantly by the use of a larger data set.

Exclusion limits on the contributions from new physics processes are derived in the framework of anomalous quartic gauge couplings described by an effective field theory. Fourteen coupling parameters are accessible by the study of the $e\mu\gamma$ final state and frequentist limits at 95 % confidence level are derived for each of them. This measurement confirms the limits that are set by other analyses and is complementary to them. However, the limits are not as stringent as the ones obtained by the study of vector boson scattering processes. Since the anomalous quartic gauge couplings can violate unitarity at the tested energy scales, the exclusion limits are also derived for all coupling parameters when they are unitarised with a dipole form factor. This work extends the current set of exclusion limits on unitarised anomalous gauge couplings as, for most parameters, no other unitarised exclusion limits have been published.

All in all, the analysis presented here agrees well with the Standard Model expectations. More sensitivity can be achieved with a data set of larger statistics, foreseen with the higher collision energy of $\sqrt{s} = 13\,TeV$. Once this data set exceeds the statistics of the one employed here, a similar analysis can be performed and the observation of the $WW\gamma$ signal might be feasible.

A Appendix

A.1 Event Display of a Candidate Event

The event display of Figure 1 shows the cross-section of the ATLAS detector in the x-y-plane that is perpendicular to the beam axis. Three additional views of the event are provided in Figure A.1. There, the cross-section of the detector is also shown in the R-z-plane, i.e. along the beam axis and in the ϕ-z- and ϕ-η-plane. Again, the Atlantis event display was employed to produce the visualisations. The inner detector shows tracks recorded with a transverse momentum exceeding 1 GeV. The electron, photon and muon are indicated by the green, the yellow and the red bar respectively. The length of the bar corresponds to the relative transverse

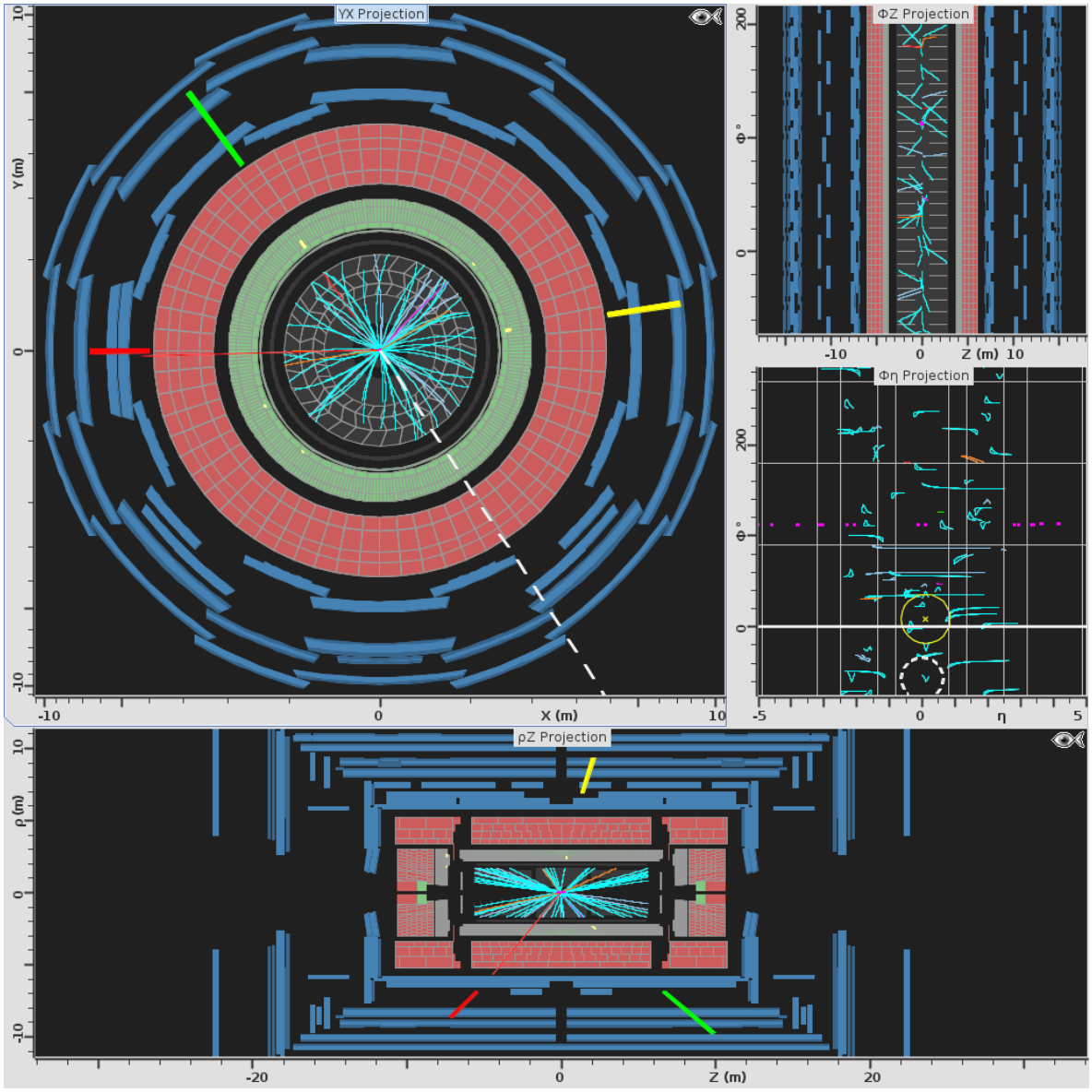

Figure A.1: Visualisation in different cutting planes of the outcome of a particle collision recorded with the ATLAS detector. Distorted proportions are indicated by the fish-eye symbol in each panel when applied. The shown event is candidate signal event of the analysis presented here.

momentum of the respective object. The dotted line indicates the direction of the missing transverse energy in the event.

A.2 Dimension-8 Operators of Anomalous Quartic Gauge Couplings

The dimension-8 operators that contribute to the anomalous quartic gauge coupling vertices $W^+W^-\gamma\gamma$ and $W^+W^-Z\gamma$ can be grouped into two categories:

1. Operators containing derivatives of the Higgs field Φ, called $\mathcal{O}_M$
2. Operators not containing the Higgs field Φ, called $\mathcal{O}_T$

They are detailed in [20] as functions of the Standard Model fields and summarized here.

The covariant derivative is defined as a function of the fields B_μ and W_μ^k, with $k \in \{1, 2, 3\}$, according to:

$$D_\mu \equiv \partial_\mu + i\frac{g'}{2}B_\mu + igW_\mu^k\frac{\tau^k}{2}$$

and τ^k denotes the SU(2) generators that obey $\mathrm{Tr}[\tau^i\tau^j] = 2\delta^{ij}$. g and g' are the electroweak coupling parameters, and are free parameters in the Standard Model.

The gauge fields can be used to build the field strength tensors $B_{\mu\nu}$ and $W_{\mu\nu}$ which are defined as:

$$B_{\mu\nu} = \frac{i}{2}g'(\partial_\mu B_\nu - \partial_\nu B_\mu)$$
$$W_{\mu\nu} = \frac{i}{2}g\tau^k(\partial_\mu W_\nu^k - \partial_\nu W_\mu^k + g\epsilon_{klm}W_\mu^l W_\nu^m),$$

with ϵ_{klm} being the totally antisymmetric Levi-Civita tensor.

In this notation the dimension-8 operators of the first group can be written as:

$$\mathcal{O}_{M,0} = \mathrm{Tr}[W_{\mu\nu}W^{\mu\nu}] \times [(D_\beta\Phi)^\dagger D^\beta\Phi],$$
$$\mathcal{O}_{M,1} = \mathrm{Tr}[W_{\mu\nu}W^{\nu\beta}] \times [(D_\beta\Phi)^\dagger D^\mu\Phi],$$
$$\mathcal{O}_{M,2} = [B_{\mu\nu}B^{\mu\nu}] \times [(D_\beta\Phi)^\dagger D^\beta\Phi],$$
$$\mathcal{O}_{M,3} = [B_{\mu\nu}B^{\nu\beta}] \times [(D_\beta\Phi)^\dagger D^\mu\Phi],$$
$$\mathcal{O}_{M,4} = [(D_\mu\Phi)^\dagger W_{\beta\nu}D^\mu\Phi] \times B^{\beta\nu},$$
$$\mathcal{O}_{M,5} = [(D_\mu\Phi)^\dagger W_{\beta\nu}D^\nu\Phi] \times B^{\beta\mu},$$
$$\mathcal{O}_{M,6} = [(D_\mu\Phi)^\dagger W_{\beta\nu}W^{\beta\nu}D^\mu\Phi],$$
$$\mathcal{O}_{M,7} = [(D_\mu\Phi)^\dagger W_{\beta\nu}W^{\beta\mu}D^\nu\Phi].$$

These operators describe four boson interactions that depend on the boson momenta, since they involve the field strength tensors in their definitions.

The operators of the second group are:

$$\mathcal{O}_{T,0} = \mathrm{Tr}[W_{\mu\nu}W^{\mu\nu}] \times \mathrm{Tr}[W_{\alpha\beta}W^{\alpha\beta}],$$
$$\mathcal{O}_{T,1} = \mathrm{Tr}[W_{\alpha\nu}W^{\mu\beta}] \times \mathrm{Tr}[W_{\mu\beta}W^{\alpha\nu}],$$
$$\mathcal{O}_{T,2} = \mathrm{Tr}[W_{\alpha\mu}W^{\mu\beta}] \times \mathrm{Tr}[W_{\beta\nu}W^{\nu\alpha}],$$
$$\mathcal{O}_{T,5} = \mathrm{Tr}[W_{\mu\nu}W^{\mu\nu}] \times B_{\alpha\beta}B^{\alpha\beta},$$
$$\mathcal{O}_{T,6} = \mathrm{Tr}[W_{\alpha\nu}W^{\mu\beta}] \times B_{\mu\beta}B^{\alpha\nu},$$
$$\mathcal{O}_{T,7} = \mathrm{Tr}[W_{\alpha\mu}W^{\mu\beta}] \times B_{\beta\nu}B^{\nu\alpha}.$$

And the first three operators predict vertices between all electroweak gauge bosons. The index T represents the fact that these operators only have contributions from transverse polarisation modes, while the operators from the first group have mixed contributions from longitudinal and transverse modes.

A.3 Details on the Simulated Processes

Simulated events are used for a number of purposes in this thesis. They are employed to optimise the signal region definition for maximal signal sensitivity. The reconstruction efficiency and the acceptance are computed using the simulation of the signal process and the simulation of anomalous quartic gauge couplings for different coupling parameters. Furthermore, the irreducible backgrounds are estimated using the Monte Carlo predictions. The simulations are listed in Table A.1. Not all samples are used for the signal estimation, but for completeness samples that were used in dedicated studies only are also listed.

Process	Generator	PDF	σ [fb]	N_{events}
$WW\gamma$ (decaying to light leptons)	Sherpa	CT10	12.82	45×10^3
$WW\gamma$ (leptonic decays including τ)	Sherpa	CT10	97.42	250×10^3
$WW\gamma$ (decaying to light leptons)	MadGraph (Pythia)	CTEQ6L1	25.39	115×10^3
$WW\gamma$ (leptonic decays including τ)	MadGraph (Pythia)	CTEQ6L1	31.96	130×10^3
$WW\gamma$ with aQGCs	MadGraph (Pythia)	CTEQ6L1	sample dependant	50×10^3
$qq \to WW \to l\nu l'\nu'$	Powheg (Pythia)	CT10	5580.00	540×10^3
$gg \to WW \to l\nu l'\nu'$	gg2ww (H+J)	CT10	153.00	270×10^3
Wt (decaying leptonically)	Powheg (Pythia)	CT10	2348.83	9.98×10^6
WZ (decaying leptonically)	Sherpa	CT10	9750.80	2.70×10^6
$ZZ \to llll$	Sherpa	CT10	8740.30	3.80×10^6
$ZZ \to ll\nu\nu$	Sherpa	CT10	496.01	900×10^3
Multijet final states	Pythia8	CTEQ6L1	1235×10^9	100×10^6
$t\bar{t}\gamma \to l\nu bl'\nu'b'\gamma$	MadgraphPythia	CTEQ6L1	173.33	45×10^3
$WZ\gamma$ (decaying to light leptons)	Sherpa	CT10	5.35	59×10^3
$W\gamma$	Alpgen (H+J)	CTEQ6L1	368.57	23.88×10^6
W (decaying leptonically)	Alpgen (Pythia)	CT10	36.68×10^6	32.94×10^6
$W\gamma\gamma$ ($W \to e\nu$)	Sherpa	CT10	162.4	350×10^3
$W\gamma\gamma$ ($W \to \mu\nu$)	Sherpa	CT10	161.8	350×10^3
$\gamma^*/Z\gamma$ (decaying leptonically)	Sherpa	CT10	96940	22.03×10^6
Z (decaying leptonically)	Alpgen (Pythia)	CT10	3.45×10^6	73.93×10^6

Table A.1: Monte Carlo simulations used in this thesis. The process is quoted along with the generator used for its simulation. When a general purpose generator is used for the hadronisation of the particles or the underlying event, the name of this generator is quoted in brackets, where H+J stands for HERWIG+JIMMY. The parton density function (PDF) used to generate the events is also stated along with the cross-section σ and the statistics of the samples. The difference in cross-section for the simulation of the leptonic $WW\gamma$ processes between the two generators comes from the fact that a different phase space has been simulated and for the anomalous quartic gauge couplings (aQGCs) the influence of several operators was emulated by dedicated simulations.

A.4 More Results of the Combined ABCD Method

The impact of the different components of systematic uncertainty on the extracted number of signal events, $N_{\mathrm{A}}^{WW\gamma}$, is listed in Table A.2. They are evaluated by fixing the parameter under study to its best fit result plus one standard deviation, and remaximising the likelihood given in Equation (6.15). The procedure is repeated when lowering the parameter value from its best fit number by one standard deviation. The maximal relative difference between the nominal value of $N_{\mathrm{A}}^{WW\gamma}$ and the ones obtained with the shifted parameter is quoted as relative uncertainty.

Source	Rel. Uncertainty [%]
Uncertainty on $N_{\mathrm{A}}^{\mathrm{MC}}$	21.9
Uncertainty on $N_{\mathrm{B}_\gamma}^{\mathrm{MC}}$	2.8
Uncertainty on $N_{\mathrm{C}_\gamma}^{\mathrm{MC}}$	0.7
Uncertainty on $N_{\mathrm{D}_\gamma}^{\mathrm{MC}}$	0.3
Uncertainty on $N_{\mathrm{B}_e}^{\mathrm{MC}}$	1.8
Uncertainty on $N_{\mathrm{C}_e}^{\mathrm{MC}}$	0.01
Uncertainty on $N_{\mathrm{D}_e}^{\mathrm{MC}}$	0.02
Uncertainty on c_{B_γ}	0.5
Uncertainty on c_{C_γ}	0.4
Uncertainty on c_{D_γ}	0.2
Uncertainty on c_{B_e}	1.6
Uncertainty on c_{C_e}	0.3
Uncertainty on c_{D_e}	0.02
Photon control region correlation (ρ_γ)	8.4
Electron control region correlation (ρ_e)	0.1
Uncertainty on $\epsilon_{\mathrm{C}}^{\mathrm{trig.}}$	0.02
Uncertainty on $\epsilon_{\mathrm{D}}^{\mathrm{trig.}}$	0.08

Table A.2: Relative systematic uncertainty on the number of signal events split into the different components discussed in Section 6.3.5.

The variables of the likelihood function of the combined ABCD method, given in Equation (6.15) are listed in Table A.3. Their input values are given along with their best fit value. Overall, a good agreement between the input and the best fit values is observed. The values only change notably for the event counts in the control regions defined for the estimation of jets misidentified as electrons. While the likelihood for the signal is maximal, if more events are observed in region B_e, the fit underestimates the event counts in regions C_e and D_e.

Observable	Input Value	Best Fit Value
N_{A}	26 ± 5	25 ± 5
N_{B_γ}	7 ± 3	7 ± 3
N_{C_γ}	8 ± 3	8 ± 3
N_{D_γ}	13 ± 4	13 ± 4
N_{B_e}	1 ± 1	2 ± 1
N_{C_e}	95 ± 10	83 ± 9
N_{D_e}	122 ± 11	99 ± 9
$N_{\mathrm{A}}^{\mathrm{MC}}$	11.0 ± 2.2	11.2 ± 2.2
$N_{\mathrm{B}_\gamma}^{\mathrm{MC}}$	1.8 ± 0.5	1.8 ± 0.5
$N_{\mathrm{C}_\gamma}^{\mathrm{MC}}$	0.6 ± 0.2	0.5 ± 0.2
$N_{\mathrm{D}_\gamma}^{\mathrm{MC}}$	0.11 ± 0.07	0.09 ± 0.09
c_{B_γ}	0.108 ± 0.010	0.108 ± 0.010
c_{C_γ}	0.081 ± 0.008	0.081 ± 0.008
c_{D_γ}	0.011 ± 0.003	0.011 ± 0.003
ρ_γ	1.0 ± 0.4	1.0 ± 0.5
$N_{\mathrm{B}_e}^{\mathrm{MC}}$	1.1 ± 0.4	1.0 ± 0.4
$N_{\mathrm{C}_e}^{\mathrm{MC}}$	21.3 ± 3.4	21.3 ± 3.4
$N_{\mathrm{D}_e}^{\mathrm{MC}}$	1.9 ± 0.3	1.9 ± 0.3
c_{B_e}	0.086 ± 0.009	0.086 ± 0.009
c_{C_e}	0.002 ± 0.0001	0.002 ± 0.0001
c_{D_e}	0.001 ± 0.0001	0.001 ± 0.0001
ρ_e	1.00 ± 0.69	0.86 ± 0.77
$\epsilon_{\mathrm{C}}^{\mathrm{trig.}}$	0.88 ± 0.01	0.88 ± 0.01
$\epsilon_{\mathrm{D}}^{\mathrm{trig.}}$	0.81 ± 0.01	0.81 ± 0.01

Table A.3: Input values of the variables of the ABCD methods along with their best fit value and uncertainty.

A.5 Input Values for the Cross-Section Expectation Computation

The theoretical expectations of the $WW\gamma$ production cross-section are computed using the VBFNLO program. It is steered by the file `vbfnlo.dat` specifying the process and the input parameters as well as by the file `cuts.dat` that specifies the requirements on the objects defining the fiducial region. For completeness, both files are printed here.

The file `vbfnlo.dat` reads:

```
!   Main input file for vbfnlo

!   General parameters of the calculation
!-----------------------------------------
PROCESS              = 460                 ! Identifier for process
LOPROCESS_PLUS_JET   = false               ! switch: LO process with 1 additional jet
LEPTONS              = 98                  ! final state leptons

! lepton numbering according to MC particle numbering scheme
! particles are given positive numbers, antiparticles negative numbers
! e-   ve   mu-  vm   ta-  vt
! 11   12   13   14   15   16
! 98 : leptons are either generation 1 or generation 2
! 99 : any lepton

LO_ITERATIONS        = 4         ! number of iterations for LO calculation
NLO_ITERATIONS       = 4         ! number of iterations for real-emissions calc.
LO_POINTS            = 20        ! number of points for LO calculation (= 2^..)
NLO_POINTS           = 20        ! number of points for real-emissions calc. (= 2^..)
LO_GRID              = "grid2_1" "grid2_2" "grid2_3" "grid2_4" ! names of LO files
NLO_GRID             = "grid3_1" "grid3_2" "grid3_3" "grid3_4" ! names of real em. files
PHTN_GRID            = "grid4_1" "grid4_2" "grid4_3" "grid4_4" ! names of photon em. files
FLOOP_GRID           = "grid5_1" "grid5_2" "grid5_3" "grid5_4" ! names of fermion loop files
NLO_SWITCH           = true      ! switch: nlo/lo calculation
EWCOR_SWITCH         = false     ! Whether electoweak corrections are included
FERMIONLOOP          = 3         ! Contribution of gluon-induced fermion loops for dibosons
                                 ! 0: none
                                 ! 1: only box diagrams
                                 ! 2: only Higgs resonance
                                 ! 3: both contributions (default)

ECM                  = 8000d0    ! collider center-of-mass energy
BEAM1                = 1         ! type of beam 1 (1=proton, -1 = antiproton)
BEAM2                = 1         ! type of beam 2 (1=proton, -1 = antiproton)

ID_MUF               = 4         ! ID for factorization scale
ID_MUR               = 4         ! ID for renormalization scale
MUF_USER             = 100d0     ! user defined factorization scale, if MUF is set to 0
MUR_USER             = 100d0     ! user defined renormalization scale, if MUR is set to 0
XIF                  = 1d0       ! scale factor xi for mu_F (not mu^2!!)
XIR                  = 1d0       ! scale factor xi for mu_R


!   Physics parameters
!-----------------------
HMASS       = 126.0d0         ! Higgs mass
HTYPE       = 0               ! Type of Higgs produced:
```

```
                                !      0     SM Higgs with mass HMASS
                                !      1     light cp-even type higgs h0
                                !      2     heavy cp-even type higgs HH
                                !      3     lightest cp-odd type higgs A0
                                !   SUSY parameters for 1-3 are set in susy.dat.
                                !   For these options, if input 'MODEL' is set
                                !   to 1 (SM), calculation will run in the SM
                                !   for a Higgs with equivalent mass to that
                                !   chosen in the MSSM.
MODEL       = 1                 ! model: 1 for SM, 2 for MSSM
HWIDTH      = -999d0            ! Higgs width (set to -999d0 for internal calculation)
TOPMASS     = 172.4d0           ! Top mass
BOTTOMMASS  = 4.855d0           ! Bottom Pole mass
CHARMMASS   = 1.65d0            ! Charm Pole mass
TAU_MASS    = 1.77684D0         ! Tau mass
ALFA_S      = 0.1176d0          ! Strong coupling constant
EWSCHEME    = 3                 ! Choose scheme for electroweak parameters (1,2,3,4)
EW_APPROX   = 0                 ! Approximation used when calculating electroweak
FERMI_CONST = 1.16637d-5        ! Fermi Constant
ALFA        = 7.2973525376d-3 ! Fine-structure constant
SIN2W       = 0.23119d0         ! Weak mixing angle
WMASS       = 80.398d0          ! W mass
ZMASS       = 91.1876d0         ! Z mass
ANOM_CPL    = false             ! Anomalous couplings
KK_MOD      = false             ! Warped Higgsless Model
SPIN2       = false             ! Spin-2 model


!   Parameters for the LHA event output
!-----------------------------------------
LHA_SWITCH            = false    ! Les Houches interface only for LO calculation
LHA_FILE              = event.lhe  ! Name of Les Houches output file
HEPMC_SWITCH          = false      ! HepMC interface only for LO calculation
HEPMC_FILE            = event.hepmc ! Name of HepMC output file
UNWEIGHTING_SWITCH    = true     ! unweighted/weighted (T/F) events for LHA
PRENEVUNW             = 1000     ! number of events to calculate pre-maximal weight
TAUMASS               = false    ! Include mass of the tau lepton(s) in the LHA file for VBF


!   PDF set parameters
!------------------------
PDF_SWITCH    = 0       ! which pdfs to use: 1 = lhapdf, 0 = hard-wired cteq (default)
! choose pdfset and pdfmember here. Look at the LHAPDF manual for details.
LO_PDFNAME    = cteq6ll.LHpdf
NLO_PDFNAME   = CT10.LHgrid
LO_PDFMEMBER  = 0
NLO_PDFMEMBER = 0


!   Parameters for histogram creation
!---------------------------------------
XSECFILE        = xsection        ! name of output-file (+ .out)
ROOT     = true           ! create root-file?
TOP      = false           ! create top-drawer file?
GNU      = false           ! create gnu-plot script file?
DATA     = false           ! create data file?
REPLACE  = true            ! replace output files?
```

```
ROOTFILE = histograms      ! name of root-file ( + '.root')
TOPFILE  = histograms      ! name of top-drawer file ( + '.top')
GNUFILE  = histograms      ! name of gnuplot file ( + '.gp')
DATAFILE = histograms      ! name of data directory ( + '.dir')
```

The content of `cuts.dat` is:

```
! input file for the cut parameters

!   Jet cuts
!-------------
RJJ_MIN    = 0.4d0      ! min jet-jet R separation
Y_P_MAX    = 4.4d0      ! max pseudorapidity for partons
PGENKTJET  = -1.0d0      ! exponent of generalised k_T algorithm
PT_JET_MIN = 25.0d0     ! min jet pT
Y_JET_MAX  = 4.4d0      ! max jet rapidity

!   Lepton cuts (only applied to charged leptons)
!-------------------------------------------------
Y_L_MAX    = 2.5d0      ! max lepton rapidity
PT_L_MIN   = 20.0d0     ! min lepton pT
MLL_MIN    = 50.0d0     ! min. m_l+l- for any comb. of opposite charged leptons
!MLL_MAX   = 14000d0    ! max. m_l+l- for any comb. of opposite charged leptons
RLL_MIN    = 0.1d0      ! min lepton-lepton R separation
RLL_MAX    = 50.0d0     ! max lepton-lepton R separation

!   Photon cuts
!----------------
Y_G_MAX    = 2.37d0
PT_G_MIN   = 15d0
RGG_MIN    = 0.0d0      ! min photon-photon R separation
RGG_MAX    = 50.0d0     ! max photon-photon R separation
PHISOLCUT  = 0.5d0      ! photon isolation cut
EFISOLCUT  = 1d0        ! efficiency of photon isolation cut

!   Additional R-separation cuts
!--------------------------------
RJL_MIN    = 0.3d0      ! min jet-lepton R separation
RJG_MIN    = 0.5d0      ! min jet-photon R separation
RLG_MIN    = 0.5d0      ! min lepton-photon R separation
MLG_MIN    = 0.0d0      ! min. m_lg for any comb. of charged leptons and photons
MLG_MAX    = 1.d20      ! max. m_lg for any comb. of charged leptons and photons
PTMISS_MIN = 15d0       ! min. missing transverse momentum


JVETO      = true       ! veto jet cuts
DELY_JVETO = 0.0d0      ! min veto-tag y-dist
YMAX_VETO  = 4.4d0      ! max |y| for veto jet
PTMIN_VETO = 25.0d0     ! min pT for veto jet
```

A.6 Parametrisation of the Expected Number of Events

The parabolic parametrisation of N^{aQGC} as a function of the anomalous quartic gauge couplings is given in Table A.4. The values are obtained by computing the cross-section of five different values for the respective anomalous quartic coupling and fitting them with a parabolic function.

Coupling	n_0	n_1 $[10^{-5}]$	n_2 $[10^{-6}]$
$f_{M,0}/\Lambda^4$	0.479	−15.3	22.5
$f_{M,1}/\Lambda^4$	0.481	10.3	7.81
$f_{M,2}/\Lambda^4$	0.477	−0.78	0.70
$f_{M,3}/\Lambda^4$	0.478	0.78	0.24
$f_{M,4}/\Lambda^4$	0.477	−4.35	1.72
$f_{M,5}/\Lambda^4$	0.477	−3.30	0.73
$f_{M,6}/\Lambda^4$	0.477	−7.00	5.63
$f_{M,7}/\Lambda^4$	0.477	−5.71	1.94
$f_{T,0}/\Lambda^4$	0.479	−11.4	126.
$f_{T,1}/\Lambda^4$	0.481	−25.0	77.4
$f_{T,2}/\Lambda^4$	0.484	−13.9	16.2
$f_{T,5}/\Lambda^4$	0.482	0.41	0.99
$f_{T,6}/\Lambda^4$	0.479	−0.77	0.60
$f_{T,7}/\Lambda^4$	0.480	−0.21	0.13

Table A.4: Parabolic parametrisation of $N^{\mathrm{aQGC}}(\frac{f_i}{\Lambda^4}) = n_0 + n_1 \cdot (\frac{f_i}{\Lambda^4}) + n_2 \cdot (\frac{f_i}{\Lambda^4})^2$ for the different anomalous gauge couplings tested with this analysis. The units of the couplings is TeV^{-4}.

The parabolic dependence of the expected number of events from anomalous quartic gauge couplings unitarised with a dipole form factor is given in Table A.5 for the mixed and in Table A.6 for the transverse couplings. Seven different values of the expected cross-section are computed and fitted due to the lower coupling values compared to the non-unitarised case.

Coupling	n_0	n_1 $[10^{-6}]$	n_2 $[10^{-10}]$
$f_{M,0}/\Lambda^4 \cdot F(\hat{s})$	0.480	−6.38	72.2
$f_{M,1}/\Lambda^4 \cdot F(\hat{s})$	0.480	8.17	27.8
$f_{M,2}/\Lambda^4 \cdot F(\hat{s})$	0.480	−0.41	1.99
$f_{M,3}/\Lambda^4 \cdot F(\hat{s})$	0.480	0.50	0.76
$f_{M,4}/\Lambda^4 \cdot F(\hat{s})$	0.481	−2.28	5.78
$f_{M,5}/\Lambda^4 \cdot F(\hat{s})$	0.481	−2.44	2.81
$f_{M,6}/\Lambda^4 \cdot F(\hat{s})$	0.480	−3.14	18.1
$f_{M,7}/\Lambda^4 \cdot F(\hat{s})$	0.480	−3.71	6.49

Table A.5: Parabolic parametrisation of $N^{\mathrm{aQGC}}(\frac{f_i}{\Lambda^4} \cdot F(\hat{s})) = n_0 + n_1 \cdot (\frac{f_i \cdot F(\hat{s})}{\Lambda^4}) + n_2 \cdot (\frac{f_i \cdot F(\hat{s})}{\Lambda^4})^2$ for the mixed unitarised anomalous gauge couplings tested with this analysis. A dipole form factor is employed for the unitarisation with $\Lambda_{FF} = 500\,\mathrm{GeV}$ and the units of the couplings are TeV^{-4}.

Coupling	n_0	n_1 $[10^{-6}]$	n_2 $[10^{-10}]$
$f_{T,0}/\Lambda^4 \cdot F(\hat{s})$	0.480	−2.70	98.7
$f_{T,1}/\Lambda^4 \cdot F(\hat{s})$	0.480	−9.56	88.9
$f_{T,2}/\Lambda^4 \cdot F(\hat{s})$	0.481	−3.82	15.7
$f_{T,5}/\Lambda^4 \cdot F(\hat{s})$	0.480	0.72	0.68
$f_{T,6}/\Lambda^4 \cdot F(\hat{s})$	0.480	−0.15	0.53
$f_{T,7}/\Lambda^4 \cdot F(\hat{s})$	0.480	−0.84	0.07

Table A.6: Parabolic parametrisation of $N^{\mathrm{aQGC}}(\frac{f_i}{\Lambda^4} \cdot F(\hat{s})) = n_0 + n_1 \cdot (\frac{f_i \cdot F(\hat{s})}{\Lambda^4}) + n_2 \cdot (\frac{f_i \cdot F(\hat{s})}{\Lambda^4})^2$ for the transverse unitarised anomalous gauge couplings tested with this analysis. A dipole form factor is employed for the unitarisation with $\Lambda_{FF} = 400\,\mathrm{GeV}$ and the units of the couplings are TeV^{-4}.

List of Figures

List of Tables

Bibliography

[1] ATLAS Collaboration, *Atlantis - Event display for ATLAS*, URL: http://atlantis.web.cern.ch/atlantis/.

[2] CMS Collaboration, *Search for $WW\gamma$ and $WZ\gamma$ production and constraints on anomalous quartic gauge couplings in pp collisions at $\sqrt{s} = 8$ TeV*, *Phys. Rev.* D90.3 (2014) p. 032008, DOI: 10.1103/PhysRevD.90.032008, ARXIV: 1404.4619 [hep-ex].

[3] The ALEPH, DELPHI, L3 and OPAL Collaborations; the LEP Electroweak Working Group, *Electroweak Measurements in Electron-Positron Collisions at W-Boson-Pair Energies at LEP*, *Phys. Rept.* 532 (2013) p. 119, ARXIV: 1302.3415 [hep-ex].

[4] J. I. Djuvsland et al., *Measurement of $WV\gamma$ final states in proton proton collisions at $\sqrt{s} = 8$ TeV with the ATLAS detector at the LHC*, ATL-COM-PHYS-2015-1328, CERN, Oct. 2015, URL: https://cds.cern.ch/record/2062936.

[5] ATLAS Collaboration, *Evidence of $W\gamma\gamma$ Production in pp Collisions at $\sqrt{s} = 8$ TeV and Limits on Anomalous Quartic Gauge Couplings with the ATLAS Detector*, *Phys. Rev. Lett.* 115.3 (2015) p. 031802, DOI: 10.1103/PhysRevLett.115.031802, ARXIV: 1503.03243 [hep-ex].

[6] J. I. Hofmann, W Kozanecki, and S Webb, *Impact of non-factorisation effects on the absolute luminosity calibration for the March 2011 van der Meer scans*, ATL-COM-LUM-2013-001, CERN, Jan. 2013, URL: https://cds.cern.ch/record/1504314.

[7] M. Thomson, *Modern Particle Physics*, Cambridge University Press, 2013, ISBN: 978-1107034266.

[8] B. Povh et al., *Teilchen und Kerne*, Springer-Verlag Berlin Heidelberg, 2009, ISBN: 9783642378218.

[9] P. J. Mohr, D. B. Newell, and B. N. Taylor, *CODATA Recommended Values of the Fundamental Physical Constants: 2014*, July 2015, ARXIV: 1507.07956 [physics.atom-ph].

[10] Wikipedia, *Standard Model*, 11.01.2016, URL: https://en.wikipedia.org/wiki/Standard_Model#/media/File:Elementary_particle_interactions_in_the_Standard_Model.png.

[11] ATLAS Collaboration, *Observation of a new particle in the search for the Standard Model Higgs boson with the ATLAS detector at the LHC*, *Phys. Lett.* B716 (2012) pp. 1–29, DOI: 10.1016/j.physletb.2012.08.020, ARXIV: 1207.7214 [hep-ex].

[12] CMS Collaboration, *Observation of a new boson at a mass of 125 GeV with the CMS experiment at the LHC*, *Phys. Lett.* B716 (2012) pp. 30–61, DOI: 10.1016/j.physletb.2012.08.021, ARXIV: 1207.7235 [hep-ex].

[13] P. Renton, *Electroweak Interactions - An Introduction to the Physics of Quarks and Leptons*, Cambridge University Press, 1990, chap. 5, ISBN: 9780521366922.

[14] D. Yang et al., *Probing $W^+W^-\gamma$ Production and Anomalous Quartic Gauge Boson Couplings at the CERN LHC*, *JHEP* 04 (2013) p. 108, DOI: 10.1007/JHEP04(2013)108, ARXIV: 1211.1641 [hep-ph].

[15] G. Bozzi et al., *NLO QCD corrections to $W^+W^-\gamma$ and $ZZ\gamma$ production with leptonic decays*, *Phys. Rev.* D81 (2010) p. 094030, DOI: 10.1103/PhysRevD.81.094030, ARXIV: 0911.0438 [hep-ph].

[16] K. Olive and P. D. Group, *Review of Particle Physics*, *Chinese Physics C* 38.9 (2014) p. 090001, URL: http://stacks.iop.org/1674-1137/38/i=9/a=090001.

[17] J. Baglio et al., *Release Note - VBFNLO 2.7.0* (2014), ARXIV: 1404.3940 [hep-ph].

[18] K. Arnold et al., *VBFNLO: A Parton Level Monte Carlo for Processes with Electroweak Bosons – Manual for Version 2.5.0* (2011), ARXIV: 1107.4038 [hep-ph].

[19] K. Arnold et al., *VBFNLO: A Parton level Monte Carlo for processes with electroweak bosons*, *Comput. Phys. Commun.* 180 (2009) pp. 1661–1670, DOI: 10.1016/j.cpc.2009.03.006, ARXIV: 0811.4559 [hep-ph].

[20] C. Degrande et al., *Monte Carlo tools for studies of non-standard electroweak gauge boson interactions in multi-boson processes: A Snowmass White Paper*, *Community Summer Study 2013: Snowmass on the Mississippi (CSS2013) Minneapolis, MN, USA, July 29-August 6, 2013*, 2013, ARXIV: 1309.7890 [hep-ph], URL: http://inspirehep.net/record/1256129/files/arXiv:1309.7890.pdf.

[21] C. Degrande et al., *Effective Field Theory: A Modern Approach to Anomalous Couplings*, *Annals Phys.* 335 (2013) pp. 21–32, DOI: 10.1016/j.aop.2013.04.016, ARXIV: 1205.4231 [hep-ph].

[22] O. J. P. Eboli, M. C. Gonzalez-Garcia, and S. M. Lietti, *Bosonic quartic couplings at CERN LHC*, *Phys. Rev.* D69 (2004) p. 095005, DOI: 10.1103/PhysRevD.69.095005, ARXIV: hep-ph/0310141.

[23] CMS Collaboration, *Evidence for exclusive gamma-gamma to W^+W^- production and constraints on anomalous quartic gauge couplings at $\sqrt{s} = 7$ and 8 TeV* (2016), ARXIV: 1604.04464 [hep-ex].

[24] CMS Collaboration, *Study of vector boson scattering and search for new physics in events with two same-sign leptons and two jets*, *Phys. Rev. Lett.* 114.5 (2015) p. 051801, DOI: 10.1103/PhysRevLett.114.051801, ARXIV: 1410.6315 [hep-ex].

[25] L. Evans and P. Bryant, *LHC Machine*, *JINST* 3 (2008), ed. by L. Evans S08001, DOI: 10.1088/1748-0221/3/08/S08001.

[26] ATLAS Collaboration, *The ATLAS Experiment at the CERN Large Hadron Collider*, *JINST* 3 (2008) S08003, DOI: 10.1088/1748-0221/3/08/S08003.

[27] European Organisation for Nuclear Research, *LEP Design Report: Vol.2. The LEP Main Ring* (1984), URL: https://cds.cern.ch/record/102083.

[28] F. Müller, *Jet production measurements at the ATLAS experiment*, PhD thesis: Heidelberg University, 2013.

[29] ALICE Collaboration, *The ALICE experiment at the CERN LHC*, *Journal of Instrumentation* 3.08 (2008) S08002, URL: http://stacks.iop.org/1748-0221/3/i=08/a=S08002.

[30] CMS Collaboration, *The CMS experiment at the CERN LHC*, *Journal of Instrumentation* 3.08 (2008) S08004, URL: http://stacks.iop.org/1748-0221/3/i=08/a=S08004.

[31] LHCb Collaboration, *The LHCb Detector at the LHC*, *Journal of Instrumentation* 3.08 (2008) S08005, URL: http://stacks.iop.org/1748-0221/3/i=08/a=S08005.

[32] ATLAS Collaboration, Letter of Intent (1992), URL: https://cds.cern.ch/record/291061.

[33] ATLAS Collaboration, *Expected performance of the ATLAS experiment: detector, trigger and physics*, CERN, 2009, URL: https://cds.cern.ch/record/1125884.

[34] ATLAS Collaboration, *Evidence for Electroweak Production of $W^{\pm}W^{\pm}jj$ in pp Collisions at $\sqrt{s} = 8$ TeV with the ATLAS Detector*, *Phys. Rev. Lett.* 113.14 (2014) p. 141803, DOI: 10.1103/PhysRevLett.113.141803, ARXIV: 1405.6241 [hep-ex].

[35] S. P. Martin, *A Supersymmetry primer* (1997), DOI: 10.1142/9789812839657_0001,10.1142/9789814307505_0001, ARXIV: hep-ph/9709356.

[36] L. Randall and R. Sundrum, *Large Mass Hierarchy from a Small Extra Dimension*, *Phys. Rev. Lett.* 83 (17 Oct. 1999) pp. 3370–3373, DOI: 10.1103/PhysRevLett.83.3370, URL: http://link.aps.org/doi/10.1103/PhysRevLett.83.3370.

[37] ATLAS Collaboration, *The ATLAS Inner Detector commissioning and calibration*, *Eur. Phys. J.* C70 (2010) pp. 787–821, DOI: 10.1140/epjc/s10052-010-1366-7, ARXIV: 1004.5293 [physics.ins-det].

[38] M. Aharrouche et al., *Energy Linearity and Resolution of the ATLAS Electromagnetic Barrel Calorimeter in an Electron Test-Beam*, *Nucl. Instrum. Methods Phys. Res., A* 568.physics/0608012 (Aug. 2006) pp. 601–623, URL: http://cds.cern.ch/record/976098.

[39] T. Davidek and the Atlas Tilecal system, *ATLAS Tile Calorimeter performance for single particles in beam tests*, *Journal of Physics: Conference Series* 160.1 (2009) p. 012057, URL: http://stacks.iop.org/1742-6596/160/i=1/a=012057.

[40] B. Dowler et al., *Performance of the ATLAS hadronic end-cap calorimeter in beam tests*, *Nucl. Instrum. Meth.* A482 (2002) pp. 94–124, DOI: 10.1016/S0168-9002(01)01338-9.

[41] J. P. Archambault et al., *Energy calibration of the ATLAS Liquid Argon Forward Calorimeter*, *Journal of Instrumentation* 3.02 (2008) P02002, URL: http://stacks.iop.org/1748-0221/3/i=02/a=P02002.

[42] ATLAS Collaboration, *Measurement of the muon reconstruction performance of the ATLAS detector using 2011 and 2012 LHC proton–proton collision data*, *Eur. Phys. J.* C74.11 (2014) p. 3130, DOI: 10.1140/epjc/s10052-014-3130-x, ARXIV: 1407.3935 [hep-ex].

[43] S. van der Meer, *Calibration of the effective beam height in the ISR*, CERN-ISR-PO-68-31, CERN, 1968, URL: https://cds.cern.ch/record/296752.

[44] ATLAS Collaboration, *Improved luminosity determination in pp collisions at $\sqrt{s} = 7$ TeV using the ATLAS detector at the LHC*, *Eur. Phys. J.* C73.CERN-PH-EP-2013-026 (Feb. 2013) 2518. 40 p, ISSN: 1434-6052, DOI: 10.1140/epjc/s10052-013-2518-3, URL: http://dx.doi.org/10.1140/epjc/s10052-013-2518-3.

[45] ATLAS Collaboration, *Summary of cross section measurements by ATLAS presented as a function of centre-of-mass energy $\sqrt{s}$ from 7 to 13 TeV for a few selected processes*, 26.01.2016, URL: https://atlas.web.cern.ch/Atlas/GROUPS/PHYSICS/CombinedSummaryPlots/SM/index.html#ATLAS_m_SMSummary_SqrtS.

[46] ATLAS Collaboration, *ATLAS detector and physics performance: Technical Design Report, Volume 1*, Technical Design Report ATLAS (1999), URL: https://cds.cern.ch/record/391176.

[47] T. Sjostrand, *Monte Carlo Generators*, *High-energy physics. Proceedings, European School, Aronsborg, Sweden, June 18-July 1, 2006*, 2006 pp. 51–74, ARXIV: hep-ph/0611247, URL: http://weblib.cern.ch/abstract?CERN-LCGAPP-2006-06.

[48] S. Agostinelli et al., *GEANT4: A simulation toolkit*, *Nucl. Instrum. Meth. A* 506 (2003) pp. 250–303, DOI: 10.1016/S0168-9002(03)01368-8.

[49] ATLAS Collaboration, *The ATLAS Simulation Infrastructure*, *Eur. Phys. J.* C70 (2010), DOI: 10.1140/epjc/s10052-010-1429-9, ARXIV: 1005.4568 [physics.ins-det].

[50] J. M. Campbell, J. W. Huston, and W. J. Stirling, *Hard Interactions of Quarks and Gluons: A Primer for LHC Physics*, *Rept. Prog. Phys.* 70 (2007) p. 89, DOI: 10.1088/0034-4885/70/1/R02, ARXIV: hep-ph/0611148.

[51] G. Altarelli and G. Parisi, *Asymptotic Freedom in Parton Language*, *Nucl. Phys.* B126 (1977) p. 298, DOI: 10.1016/0550-3213(77)90384-4.

[52] Y. L. Dokshitzer, *Calculation of the Structure Functions for Deep Inelastic Scattering and e+ e- Annihilation by Perturbation Theory in Quantum Chromodynamics.*, *Sov. Phys. JETP* 46 (1977), [Zh. Eksp. Teor. Fiz.73,1216(1977)] pp. 641–653.

[53] V. N. Gribov and L. N. Lipatov, *Deep inelastic e p scattering in perturbation theory*, *Sov. J. Nucl. Phys.* 15 (1972), [Yad. Fiz.15,781(1972)] pp. 438–450.

[54] H.-L. Lai et al., *New parton distributions for collider physics*, *Phys. Rev. D* 82 (7 Oct. 2010) p. 074024, DOI: 10.1103/PhysRevD.82.074024, URL: http://link.aps.org/doi/10.1103/PhysRevD.82.074024.

[55] J. Pumplin et al., *New generation of parton distributions with uncertainties from global QCD analysis*, *JHEP* 07 (2002) p. 012, ARXIV: hep-ph/0201195.

[56] A. D. Martin et al., *Parton distributions for the LHC*, *Eur. Phys. J.* C63 (2009) pp. 189–285, DOI: 10.1140/epjc/s10052-009-1072-5, ARXIV: 0901.0002 [hep-ph].

[57] S. Catani et al., *QCD matrix elements + parton showers*, *JHEP* 11 (2001) p. 063, DOI: 10.1088/1126-6708/2001/11/063, ARXIV: hep-ph/0109231.

[58] J. Alwall et al., *Comparative study of various algorithms for the merging of parton showers and matrix elements in hadronic collisions*, *Eur. Phys. J.* C53 (2008) pp. 473–500, DOI: 10.1140/epjc/s10052-007-0490-5, ARXIV: 0706.2569 [hep-ph].

[59] S. Frixione, P. Nason, and C. Oleari, *Matching NLO QCD computations with Parton Shower simulations: the POWHEG method*, *JHEP* 11 (2007) p. 070, DOI: 10.1088/1126-6708/2007/11/070, ARXIV: 0709.2092 [hep-ph].

[60] B. Andersson, *The Lund Model*, Part of Cambridge Monographs on Particle Physics, Nuclear Physics and Cosmology, Cambridge University Press, 2005, ISBN: 9780521017343.

[61] T. D. Gottschalk, *A Realistic Model for e+ e- Annihilation Including Parton Bremsstrahlung Effects*, *Nucl. Phys.* B214 (1983) p. 201, DOI: 10.1016/0550-3213(83)90658-2.

[62] T. Gleisberg et al., *Event generation with SHERPA 1.1*, *JHEP* 0902 (2009) p. 007, DOI: 10.1088/1126-6708/2009/02/007, ARXIV: 0811.4622 [hep-ph].

[63] T. Sjostrand, S. Mrenna, and P. Z. Skands, *PYTHIA 6.4 Physics and Manual*, *JHEP* 0605 (2006) p. 026, DOI: 10.1088/1126-6708/2006/05/026, ARXIV: hep-ph/0603175.

[64] T. Gleisberg and S. Hoche, *Comix, a new matrix element generator*, *JHEP* 0812 (2008) p. 039, DOI: 10.1088/1126-6708/2008/12/039, ARXIV: 0808.3674 [hep-ph].

[65] S. Schumann and F. Krauss, *A Parton shower algorithm based on Catani-Seymour dipole factorisation*, *JHEP* 0803 (2008) p. 038, DOI: 10.1088/1126-6708/2008/03/038, ARXIV: 0709.1027 [hep-ph].

[66] S. Hoche et al., *QCD matrix elements and truncated showers*, *JHEP* 0905 (2009) p. 053, DOI: 10.1088/1126-6708/2009/05/053, ARXIV: 0903.1219 [hep-ph].

[67] T. Sjostrand, S. Mrenna, and P. Z. Skands, *A Brief Introduction to PYTHIA 8.1*, *Comput. Phys. Commun.* 178 (2008) p. 852, DOI: 10.1016/j.cpc.2008.01.036, ARXIV: 0710.3820 [hep-ph].

[68] J. Alwall et al., *MadGraph 5 : Going Beyond*, *JHEP* 1106 (2011) p. 128, DOI: 10.1007/JHEP06(2011)128, ARXIV: 1106.0522 [hep-ph].

[69] J. Alwall et al., *The automated computation of tree-level and next-to-leading order differential cross sections, and their matching to parton shower simulations*, *JHEP* 07 (2014) p. 079, DOI: 10.1007/JHEP07(2014)079, ARXIV: 1405.0301 [hep-ph].

[70] P. Nason, *A New method for combining NLO QCD with shower Monte Carlo algorithms*, *JHEP* 0411 (2004) p. 040, DOI: 10.1088/1126-6708/2004/11/040, ARXIV: hep-ph/0409146.

[71] M. L. Mangano et al., *ALPGEN, a generator for hard multiparton processes in hadronic collisions*, *JHEP* 0307 (2003) p. 001, DOI: 10.1088/1126-6708/2003/07/001, ARXIV: hep-ph/0206293.

[72] G. Corcella et al., *HERWIG 6: An Event generator for hadron emission reactions with interfering gluons (including supersymmetric processes)*, *JHEP* 0101 (2001) p. 010, DOI: 10.1088/1126-6708/2001/01/010, ARXIV: hep-ph/0011363.

[73] J. Butterworth, J. R. Forshaw, and M. Seymour, *Multiparton interactions in photoproduction at HERA*, *Z. Phys.* C72 (1996) pp. 637–646, DOI: 10.1007/s002880050286, ARXIV: hep-ph/9601371.

[74] T. Binoth et al., *Gluon-induced W-boson pair production at the LHC*, *JHEP* 12 (2006) p. 046, DOI: 10.1088/1126-6708/2006/12/046, ARXIV: hep-ph/0611170.

[75] *ATLAS Computing: technical design report*, Technical Design Report ATLAS, CERN, 2005, URL: http://cds.cern.ch/record/837738.

[76] C. Eck et al., *LHC computing Grid: Technical Design Report. Version 1.06 (20 Jun 2005)*, Technical Design Report LCG, CERN, 2005, URL: http://cds.cern.ch/record/840543.

[77] ATLAS Collaboration, *Expected performance of the ATLAS experiment: detector, trigger and physics*, CERN, 2009, URL: https://cds.cern.ch/record/1125884.

[78] ATLAS Collaboration, *Measurements of the photon identification efficiency with the ATLAS detector using 4.9 fb^{-1} of pp collision data collected in 2011*, ATLAS-CONF-2012-123, CERN, Aug. 2012, URL: http://cds.cern.ch/record/1473426.

[79] W. Lampl et al., *Calorimeter Clustering Algorithms: Description and Performance*, ATL-LARG-PUB-2008-002, CERN, Apr. 2008, URL: https://cds.cern.ch/record/1099735.

[80] ATLAS Collaboration, *Expected photon performance in the ATLAS experiment*, ATL-PHYS-PUB-2011-007, CERN, Apr. 2011, URL: https://cds.cern.ch/record/1345329.

[81] ATLAS Collaboration, *Electron and photon energy calibration with the ATLAS detector using LHC Run 1 data*, *Eur. Phys. J.* C74.10 (2014) p. 3071, DOI: 10.1140/epjc/s10052-014-3071-4, ARXIV: 1407.5063 [hep-ex].

[82] ATLAS Collaboration, *Electron efficiency measurements with the ATLAS detector using the 2012 LHC proton-proton collision data*, ATLAS-CONF-2014-032, CERN, June 2014, URL: https://cds.cern.ch/record/1706245.

[83] ATLAS Collaboration, *Measurement of the inclusive isolated prompt photon cross section in pp collisions at $\sqrt{s} = 7$ TeV with the ATLAS detector*, *Phys. Rev. D* 83 (5 Mar. 2011) p. 052005, DOI: 10.1103/PhysRevD.83.052005, URL: http://link.aps.org/doi/10.1103/PhysRevD.83.052005.

[84] G. P. Salam, *Towards Jetography*, *Eur. Phys. J.* C67 (2010) pp. 637–686, DOI: 10.1140/epjc/s10052-010-1314-6, ARXIV: 0906.1833 [hep-ph].

[85] M. Cacciari, G. P. Salam, and G. Soyez, *The anti-k_t jet clustering algorithm*, *JHEP* 04 (2008) p. 063, DOI: 10.1088/1126-6708/2008/04/063, ARXIV: 0802.1189 [hep-ph].

[86] ATLAS Collaboration, *Jet energy measurement with the ATLAS detector in proton-proton collisions at $\sqrt{s} = 7$ TeV*, *Eur. Phys. J.* C73.3 (2013) p. 2304, DOI: 10.1140/epjc/s10052-013-2304-2, ARXIV: 1112.6426 [hep-ex].

[87] ATLAS Collaboration, *Jet energy measurement and its systematic uncertainty in proton-proton collisions at $\sqrt{s} = 7$ TeV with the ATLAS detector*, *Eur. Phys. J.* C75 (2015) p. 17, DOI: 10.1140/epjc/s10052-014-3190-y, ARXIV: 1406.0076 [hep-ex].

[88] ATLAS Collaboration, *Jet energy resolution in proton-proton collisions at $\sqrt{s} = 7$ TeV recorded in 2010 with the ATLAS detector*, *Eur. Phys. J.* C73.3 (2013) p. 2306, DOI: 10.1140/epjc/s10052-013-2306-0, ARXIV: 1210.6210 [hep-ex].

[89] ATLAS Collaboration, *Pile-up subtraction and suppression for jets in ATLAS*, ATLAS-CONF-2013-083, CERN, Aug. 2013, URL: https://cds.cern.ch/record/1570994.

[90] ATLAS Collaboration, *Performance of Missing Transverse Momentum Reconstruction in Proton-Proton Collisions at 7 TeV with ATLAS*, *Eur. Phys. J.* C72 (2012) p. 1844, DOI: 10.1140/epjc/s10052-011-1844-6, ARXIV: 1108.5602 [hep-ex].

[91] J. M. Campbell, R. K. Ellis, and C. Williams, *Vector boson pair production at the LHC*, *JHEP* 07 (2011) p. 018, DOI: 10.1007/JHEP07(2011)018, ARXIV: 1105.0020 [hep-ph].

[92] ATLAS Collaboration, *Measurement of the $t\bar{t}$ production cross-section using $e\mu$ events with b -tagged jets in pp collisions at $\sqrt{s} = 7$ and 8 TeV with the ATLAS detector*, *Eur. Phys. J.* C74.10 (2014) p. 3109, DOI: 10.1140/epjc/s10052-014-3109-7, ARXIV: 1406.5375 [hep-ex].

[93] ATLAS Collaboration, *Total Integrated Luminosity and Data Quality in 2012*, 3.03.2016, URL: https://twiki.cern.ch/twiki/bin/view/AtlasPublic/LuminosityPublicResults.

[94] ATLAS Collaboration, *Detailed summary of several Standard Model total and fiducial production cross section measurements*, 15.05.2016, URL: https://atlas.web.cern.ch/Atlas/GROUPS/PHYSICS/CombinedSummaryPlots/SM/ATLAS_d_SMSummary_FiducialXsect_rotated/ATLAS_d_SMSummary_FiducialXsect_rotated.png.

[95] K. Melnikov, M. Schulze, and A. Scharf, *QCD corrections to top quark pair production in association with a photon at hadron colliders*, *Phys. Rev. D* 83 (7 Apr. 2011) p. 074013, DOI: 10.1103/PhysRevD.83.074013, URL: http://link.aps.org/doi/10.1103/PhysRevD.83.074013.

[96] ATLAS Collaboration, *Measurement of the production cross-section of a single top quark in association with a W boson at 8 TeV with the ATLAS experiment*, *JHEP* 01 (2016) p. 064, DOI: 10.1007/JHEP01(2016)064, ARXIV: 1510.03752 [hep-ex].

[97] A. Bocci, L. Shi, and Z. Liang, *Measurements of the $e \to \gamma$ fake rate*, ATL-COM-PHYS-2014-026, CERN, Jan. 2014, URL: https://cds.cern.ch/record/1643300.

[98] F. James and M. Roos, *Minuit: A System for Function Minimization and Analysis of the Parameter Errors and Correlations*, *Comput. Phys. Commun.* 10 (1975) pp. 343–367, DOI: 10.1016/0010-4655(75)90039-9.

[99] R. Brun and F. Rademakers, *{ROOT} — An object oriented data analysis framework*, *Nuclear Instruments and Methods in Physics Research Section A: Accelerators, Spectrometers, Detectors and Associated Equipment* 389.1–2 (1997), New Computing Techniques in Physics Research V pp. 81 –86, ISSN: 0168-9002, DOI: http://dx.doi.org/10.1016/S0168-9002(97)00048-X, URL: http://www.sciencedirect.com/science/article/pii/S016890029700048X.

[100] ATLAS Collaboration, *Measurement of the inclusive $W^{\pm}$ and $Z/\gamma*$ cross sections in the e and μ decay channels in pp collisions at $\sqrt{s} = 7\,\text{TeV}$ with the ATLAS detector*, *Phys. Rev. D* 85 (7 Apr. 2012) p. 072004, DOI: 10.1103/PhysRevD.85.072004, URL: http://link.aps.org/doi/10.1103/PhysRevD.85.072004.

[101] S. Frixione, *Isolated photons in perturbative QCD*, *Phys. Lett.* B429 (1998) pp. 369–374, DOI: 10.1016/S0370-2693(98)00454-7, ARXIV: hep-ph/9801442.

[102] B. Efron, *Bootstrap Methods: Another Look at the Jackknife*, *Ann. Statist.* 7.1 (Jan. 1979) pp. 1–26, DOI: 10.1214/aos/1176344552, URL: http://dx.doi.org/10.1214/aos/1176344552.

[103] B. Efron, *Computers and the Theory of Statistics: Thinking the Unthinkable*, *SIAM Rev.* 21.4 (Dec. 1979) pp. 460–480, DOI: 10.1137/1021092, URL: http://epubs.siam.org/doi/abs/10.1137/1021092.

[104] G. Cowan et al., *Asymptotic formulae for likelihood-based tests of new physics*, *Eur. Phys. J.* C71 (2011), [Erratum: Eur. Phys. J.C73,2501(2013)] p. 1554, DOI: 10.1140/epjc/s10052-011-1554-0,10.1140/epjc/s10052-013-2501-z, ARXIV: 1007.1727 [physics.data-an].

[105] S. S. Wilks, *The Large-Sample Distribution of the Likelihood Ratio for Testing Composite Hypotheses*, *The Annals of Mathematical Statistics* 9.1 (1938) pp. 60–62, ISSN: 00034851, URL: http://www.jstor.org/stable/2957648.

[106] J. Neyman, *Outline of a Theory of Statistical Estimation Based on the Classical Theory of Probability*, *Philosophical Transactions of the Royal Society of London A: Mathematical, Physical and Engineering Sciences* 236.767 (1937) pp. 333–380, ISSN: 0080-4614, DOI: 10.1098/rsta.1937.0005, URL: http://rsta.royalsocietypublishing.org/content/236/767/333.

[107] G. J. Feldman and R. D. Cousins, *A Unified approach to the classical statistical analysis of small signals*, *Phys. Rev.* D57 (1998) pp. 3873–3889, DOI: 10.1103/PhysRevD.57.3873, ARXIV: physics/9711021.

[108] W. A. Rolke, A. M. López, and J. Conrad, *Limits and confidence intervals in the presence of nuisance parameters*, *Nuclear Instruments and Methods in Physics Research Section A: Accelerators, Spectrometers, Detectors and Associated Equipment* 551.2–3 (2005) pp. 493 –503, ISSN: 0168-9002, DOI: http://dx.doi.org/10.1016/j.nima.2005.05.068, URL: http://www.sciencedirect.com/science/article/pii/S016890020501291X.

[109] VBFNLO Collaboration, *Conventions in VBFNLO for Anomalous Quartic Gauge Boson Couplings*, 16.04.2016, URL: https://www.itp.kit.edu/vbfnlo/wiki/doku.php?id=documentation:details:aqgc.

[110] CMS Collaboration, *A search for electroweak-induced production of $W\gamma$ with two jets and constraints on anomalous quartic gauge couplings in pp collisions at $\sqrt{s} = 8$ TeV*, CMS-PAS-SMP-14-011, CERN, 2016, URL: https://cds.cern.ch/record/2124432.

[111] CMS Collaboration, *Evidence for the electroweak $Z\gamma$ production in association with two jets and a search for anomalous quartic gauge couplings in pp collisions at $\sqrt{s} = 8$ TeV*, CMS-PAS-SMP-14-018, CERN, 2015, URL: https://cds.cern.ch/record/2048148.

[112] CMS Collaboration, *Study of exclusive two-photon production of W^+W^- in pp collisions at $\sqrt{s} = 7$ TeV and constraints on anomalous quartic gauge couplings*, *JHEP* 07 (2013) p. 116, DOI: 10.1007/JHEP07(2013)116, ARXIV: 1305.5596 [hep-ex].

[113] CMS Collaboration, *Evidence for exclusive gamma-gamma to W^+W^- production and constraints on Anomalous Quartic Gauge Couplings at $\sqrt{s} = 8$ TeV*, CMS-PAS-FSQ-13-008, CERN, 2015, URL: https://cds.cern.ch/record/2025577.

[114] V. Barger et al., *Strong W^+W^+ scattering signals at pp supercolliders*, *Phys. Rev. D* 42 (9 Nov. 1990) pp. 3052–3077, DOI: 10.1103/PhysRevD.42.3052, URL: http://link.aps.org/doi/10.1103/PhysRevD.42.3052.

[115] G. J. Gounaris, J. Layssac, and F. M. Renard, *Unitarity constraints for transverse gauge bosons at LEP and supercolliders*, *Phys. Lett.* B332 (1994) pp. 146–152, DOI: 10.1016/0370-2693(94)90872-9, ARXIV: hep-ph/9311370.

[116] VBFNLO Collaboration, *VBFNLO utility to calculate form factors, version 1.3.0*, 20.04.2016, URL: https://www.itp.kit.edu/vbfnlo/wiki/doku.php?id=download:formfactor.

Acknowledgements

This project only succeeded, as I could rely on many resourceful people around me. I am very grateful to all the teachers I had in life, for helping me to become who I am today.

Above all, I want to thank my supervisor Prof. Dr. Hans-Christian Schultz-Coulon who provided the setting and financing for this work. I really enjoy working in his group! Thanks for giving me the opportunity to stay at CERN for a year and to join many schools, workshops and conferences. He gave me the freedom to choose my research topic and provided valuable input for the execution of the analysis, especially during the last months.

Secondly, I want to thank Prof. Dr. Stephanie Hansmann-Menzemer for agreeing to co-review this thesis, but also for her engagement in the research training group "Particle Physics Beyond the Standard Model". I profited from nice workshops, inspiring talks and lectures and could even practise my own skills as a lecturer.

Furthermore, I want to thank the international research training group "Development and Application of Intelligent Detectors" and the "International Max Planck Research School - PTFS" for financing me and for interesting seminars and encounters.

I am happy a place like CERN exists. Not only does it provide a platform to do outstanding research, it is also a place to meet very interesting people! I am grateful to the ATLAS collaboration; explicitly, I want to thank the L1Calo group for making my stay at CERN so interesting. But also the Electroweak subgroup for the discussions and the efforts to publish this work in the future.

The supervisor-team in Heidelberg also provided valuable input to this work. Monica, thanks a lot for all the advice - also concerning all the organisational things that come with a project like this. Veit, thanks for introducing me to the topic and for leading the way. I am especially grateful for all the practical guidance I got from you.

This work profited a lot from freely available tools like ROOT,the Linux software, Wikipedia, the google search engine and all those open source trouble shooting forums. Thanks for these efforts, they are highly appreciated.

But of course its the people that shape the environment and make "work" a pleasant place to go to. Thanks to all my colleagues, former and new, for making our group at KIP something special. In particular I want to thank all those who entertained me outside university as well. Felix, I want to thank for so much more than just this LaTeX template! And I also want to thank my office mate and sister analyser Alessandra. You definitely made work more fun and had many good ideas I could profit from. A big thank you goes to my enduring proof-readers Rainer, Alessandra, Oleg, Veit, Felix, Tobi, Steph and Øystein. Your comments improved this document so much!

Last but not least I want to thank those closest to me. Thanks to my friends and family for the support especially during the more stressful period. Thanks to my parents for the endless encouragement and support to follow my own way. I am deeply grateful to my husband Øystein who is my biggest supporter not only when it comes to IT questions. I am so happy physics brought us together!

Sage nie, das kann ich nicht,
vieles kannst du, will's die Pflicht.
Alles kannst du, will's die Liebe.
Darum dich im Schwersten übe,
Schweres fordert Lieb und Pflicht.
Sage nie, das kann ich nicht.

Autor Unbekannt